



**UNIVERSITY OF QUEBEC – “Institut National de la
Recherche Scientifique, Centre Energie, Matériaux et
Télécommunications”**

**UNIVERSITY OF CALABRIA – Ph.D. School “Science and
Engineering of Environment, Construction and Energy”**

Dual degree joint Philosophiae Doctor (Ph.D.) program

*Nano Materials and Innovative Laser-Based Accelerators for
Cultural Heritage*

Supervisor:

Patrizio Antici

Ph. D. student

Simona Veltri

Co-supervisor:

Marianna Barberio

Academic year 2016/2017

Contents

Preface	1
Chapter 1 - Introduction	5
1.1 Context and Main Scientific Objectives	5
1.2 Relevance of the Research Activity for European Union and Canada	9
1.3 Thesis Plan and main Results	11
Chapter 2 - State of the Art	19
2.1 Diagnostic methods: state of the art and experimental setups	20
2.2 Conservation Methods	43
Chapter 3 - Growth and Characterization of Nanomaterials and Nanostructured Materials for Conservation of Cultural Heritage	71
3.1 Synthesis and Characterization of thin-transparent nanostructured films for surface protection	71
3.2 TiO ₂ and SiO ₂ nanoparticles film for cultural heritage: conservation and consolidation of ceramic artifacts	84
3.3 AFM and Pulsed Laser Ablation Methods for Cultural Heritage: Application to Archeometric Analysis of Stone Artifacts	93
Chapter 4 - Innovative Laser-Plasma Diagnostics for Cultural Heritage	105
4.1 <i>One-shot PIXE</i> diagnostic	105
4.2 Design of nanostructured targets: enhanced proton beams for <i>one-shot PIXE</i>	121
4.3 Plasma Induced Luminescence in air: a new diagnostic method based on laser-plasma interaction	133
Chapter 5 - General Conclusions and Future Perspectives	141
Appendix I: Publication List	147
Attendance at International Conference	148

Preface

Cultural Heritage, defined by the UNESCO as *“the legacy of physical artefacts and intangible attributes of a group or society that are inherited from past generations, maintained in the present and bestowed for the benefit of future generations”* enriches our everyday lives in countless ways: Cultural Heritage ranges from cherished historic monuments and museums to traditional practices and contemporary art forms, includes new scientific discoveries and constitutes a source of identity and cohesion for communities disrupted by bewildering change and economic instability. This basic principle is again confirmed by the UNESCO when it says *“Heritage constitutes a source of identity and cohesion for communities disrupted by bewildering change and economic instability. Creativity contributes to building open, inclusive and pluralistic societies. Both heritage and creativity lay the foundations for vibrant, innovative and prosperous knowledge societies.[...] No development can be sustainable without a strong culture component [...] International treaties endeavor to protect and safeguard the world’s cultural and natural heritage including ancient archaeological sites, intangible and underwater heritage, museum collections, oral traditions and other forms of heritage, and to support creativity, innovation and the emergence of dynamic cultural sectors.”*

Following these principles for the sustainable development, in the last years the scientific communities put strong effort into research of innovative techniques in the field of Engineering, Physics, and Chemistry applied to Cultural Heritage (CH) for both, diagnostic and conservations, based on the applications of new materials and investigation methods.

The main challenge within this field is to obtain the greatest number of information without provoking damage to the artifacts, i.e. having an efficient method for diagnostics. Another challenge is the conservation of artifacts without modifying its aesthetical appearance. Chemical and morphological information on artworks are mainly obtained using surface spectroscopies or other methods based on particle accelerators and are most effective and sensible in laboratory. On the other hand, conservation and restoration of artifacts without changes in aesthetical aspect or chemical composition are currently obtained mostly using nanoscience and nanomaterials. The enhancement in the nanoscience and in the growth of nanomaterials allows the production of materials with new mechanical and optical properties and opens up new possibilities for the consolidation and restoration.

The ambitious aim of this Ph. D. thesis is to improve both fields of Diagnostic and Conservation in the Cultural Heritage. The main objectives of this work are 1) the development of much more sensitive and performing diagnostics and how this innovative diagnostics react on materials, 2) the improvement of new nanomaterials for the consolidation and conservation of artifacts.

As methodology, for the first topic I use laser-driven particle sources (in application for Cultural Heritage) and for the second topic the realization of thin nanostructured films and laser-generated nanoparticles working as protective materials for artifact surfaces. My thesis opens the field of new laser-driven particle accelerators for research in the field of Cultural Heritage. Moreover, the study of new nanostructured materials for consolidation and conservation allows pursuing new routes to sustainable and easily reversible restoration, without damages or irreversible changes in artwork aesthetical.



Figure 1 - Main Facilities Involved in the Ph. D project

The Ph. D thesis has been performed in the framework of a Dual Ph.D. in collaboration between *University of Calabria* (UNICAL – Italy // **GAP Research Group**) and the *Institute National de la Recherche Scientifique – Centre Energie Materiaux and Communication* (INRS-

EMT- Canada // *iPatLab Research Group*). Moreover, all the research activities were performed in strict collaboration between a network of National and International Collaboration: two partners of the “*Istituto Nazionale di Fisica Nucleare*” (INFN-Italy, INFN-CS and INFN-RM1), the “*Lawrence Livermore National Laboratories*” (LLNL - USA), the Laser Lab “*LULF*” (France), the “*Sovrintendenza ai Beni Culturali Regione Calabria*” (Italy), the *ELI-ALPS* research center (Hungary), and the *ArcheoLab* (Italy). Finally, the research activity related to this thesis was performed in different periods spent at UNICAL (18 months total), INRS-EMT (16 months total), and LLNL (2 months total) with the collaboration of researchers of all the involved institutions.

All the results obtained in this Ph. D work were published or accepted for publication in prestigious international Peer-Review Journals (i.e. Scientific Reports, Applied Surface Science, Applied Physics Letters, Applied Physics A, Surface and Coatings, Archeological Discovery), and presented in many prestigious international Conferences of Laser-Plasma, Nanoscience, and Cultural Heritage (see Appendix I for the detail of Publication).

All the project objectives were fully achieved including the challenging determination to open the first research line on Physics Applied to Cultural Heritage at the INRS-EMT, with the intention to setup dedicated experiment on CH investigation at the ALLS facility (the line is currently in preparation and the first experiment is scheduled in the second half of 2017).

The thesis is presented in 5 Chapters which include the Scientific Context, the State of the Art, the Objectives, the Results, the Conclusions of the Scientific Activities and the Future Perspectives. In detail, the Chapter 1 introduces the context of the Physics Applied to the Cultural Heritage, the Scientific Objectives with their relevance for the scientific communities (Canadian and European) and summarizes the thesis project plan and the main results. The Chapter 2 describes The State of the Art while Chapters 3 and 4 illustrate and discuss all the scientific results. The thesis closes with the General Conclusions and the Future Perspectives and, finally, the Appendix shows the Scientific Publications and the participation to the International Conferences.



Figure 2 - iPatLab Research Group during an experiment at LLNL

Chapter 1

1. Context and Main Scientific Objectives

The world of *Cultural Heritage*, in particular the field of preservation and restoration of Culture, is hindered by the lack of techniques and diagnostics suitable for the conservation and the preservation of artworks or monuments. There is therefore a strong and urgent need for the discovery and development of new techniques and methodologies for the conservation and restoration^{1,2}.

One of the main challenges in the conservation of artifacts is that they can be damaged by a corrosive patina, which can change their aesthetical aspect. The patina can strongly modify the chemical composition, provoking in the worst case the complete destruction of artwork as in the case of biological films (biofilms) on ceramic and stones exposed to biological agents. Biofilm are mostly generated in humid atmospheric conditions or underwater archeological sites. Similar to the patina, this biofilm can deteriorate the artwork's surface, causing in many cases the complete destruction of decorations, colorations, and pigments^{3,4}. Several studies have demonstrated that the role of biological agents is one of the main causes of the deterioration of stones^{5,6}.

Microorganism activity has a strong negative impact on the preservation on Cultural Heritage, because they attack the material producing nitric and sulfuric acid⁷ and as a consequence destroying the surface or generating green patina that covers completely the surface⁸. Moreover, in previous works^{9,10} it was found that the polymeric films, realized as protective film, do alter the artwork's aesthetics, changing brightness and coloration. In addition, their effects on biological agents had not been tested. Great effort has been devoted to the employment of nanomaterials (nanofiber, nanoparticles, and quantum dots) embedded in thin transparent films: Silicon dioxide nanoparticles can be used for the consolidation of porous ceramics and stones while thin films of titanium dioxide (pure or doped) can be used to realize protective and transparent films to be placed on artworks. The research in these fields is in progress and several groups have proposed the growth of new materials and their applications for different artwork substrates^{11,12} (see Figure 1 as example of nanomaterial applications)

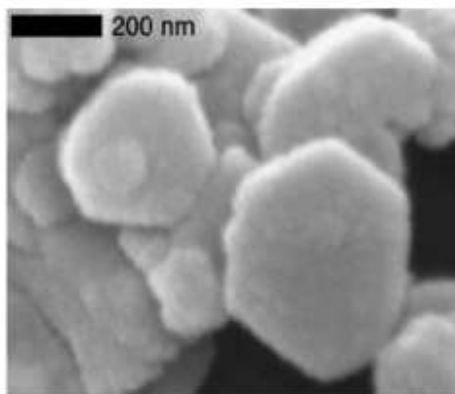


Figure 1 - SEM image of $\text{Ca}(\text{OH})_2$ nanoparticles

However, in the world of cultural Heritage, there is not only the need of preservation of the artworks, but also of diagnostic the status of an artwork. In fact, in the last years, strong exertion has been put into the research of innovative techniques in the field of Physics and Chemistry applied to Cultural Heritage for conservation and diagnostic too. Actually several groups explore the possibility to realize equipment to be used directly on site in the archeological sites or in museum. In fact, this need is due to that currently the best performing classical techniques of diagnostics and conservation (restoration and consolidation) require, generally, to move the artworks from museum, or archeological site, into a laboratory, or to make micro sampling of the artifacts (i.e. extract a small part of the artifact to be analyzed).

Chemical information on artworks (ceramic, bronzes, metals, pigments) is mainly obtained using surface spectroscopies (such as Photoluminescence, Raman, X-ray photoelectron spectroscopy (XPS), X-Ray-Fluorescence (XRF), Energy Dispersive X-ray spectroscopy (EDX) in SEM), while morphological information can be obtained with SEM. Complete chemistry of material bulks is known using sophisticated techniques of nuclear physics such as Proton Induced X-ray and Gamma Emission (PIXE and PIGE - see an example of PIXE analysis in Figure 2). All these methods are based on particle accelerators such as, e.g. the Accélérateur Grand Louvre d'Analyse Élémentaire -AGLAE in Paris and the Laboratory of Nuclear Techniques for Environment and Cultural Heritage-LABEC in Florence. Raman and Photoluminescence spectroscopy techniques, on the other side, require sophisticated spectrometers and lasers. SEM and XPS must be taken under vacuum conditions and PIXE and PIGE require the employment of large particle accelerators. Moreover, all these methods allow realizing only local analysis on artworks (beam

spot sizes are generally in the order of mm²). Several portable instrumentations, such as XRF and Raman, have been realized to make diagnostics directly in situ. However, all this portable equipment has efficiencies lower than when used in laboratory conditions. Moreover, they present the limiting factor of not being very tunable and adaptable, making their use limited only to a certain field of energy range and with that, to a certain field of interest.

The advent of lasers, which can produce compact bunches of coherent photons, has opened up possibilities of laser-based particle acceleration, as foreseen in reference¹³. The acceleration of electrons has been studied since the 70'-80' through wake fields and has recently made a breakthrough by reaching the GeV limit¹⁴ in mono-energetic bunches¹⁵. First evidence of proton production by laser-target interaction was observed in experiments between 1978-1982, yielding very low maximum proton energies of ~0.56 MeV. In 2000, evidence of laser-accelerated proton beams with significantly improved beam characteristics was obtained, yielding maximum proton energies of ~58 MeV¹⁶. Collimated high-current multi-MeV beams of protons generated by ultra-intense (>10¹⁸ W/cm²) short laser pulse (30 fs–10 ps) were discovered also by other research groups¹⁷. The investigation of laser-driven proton acceleration and its use is currently challenging many research laboratories worldwide, with some significant results, in particular for the improved characteristics of laser-based particle sources such as compactness, its efficiency, its versatility and its tunability.

A Laser-based particle beam, moreover, presents the advantage of having a high current, strong laminarity at the source, short duration, and small source size. Focusing on laser-driven proton acceleration, today, existing multi-hundred-TW table-top laser systems generating on-target intensities of ~ 10¹⁹-10²⁰ W/cm² can routinely reach proton energies of ~15-20 MeV with a typical laser-to-proton energy conversion efficiency of 1-6 %^{18,19,20} a current in the kA regime and a laminarity at the source 100 times better than conventional accelerators. These parameters make them a desired candidate for innovative applications requiring one or more of the above-mentioned properties, e.g. in the medical field²¹, for inertial confinement fusion²², warm dense matter studies²³ or hybrid accelerators²⁴. While there has been already many attempts to use and compare these laser based protons to conventional accelerated particle in some applications (medical field, etc), no effort has currently been put to test the efficiency and usage of laser-driven proton acceleration for purposes of Cultural Heritage. This opens up new opportunities to apply the field

of laser-driven particle accelerators on this research domain and to test and develop innovative and improved methods of diagnostics with new particle sources.



Figure 2 - Classical PIXE applied to the diagnostic of artworks of The Uffizi Museum of Florence

In my thesis I want to overcome some of the above mentioned existing bottlenecks proposing to improve new nanomaterials for the consolidation and conservation of the artifact and trying to develop new diagnostics methods based on Laser-Plasma Acceleration which are more sensitive and better performing.

In this scenario, there is the need to put emphasis in the research related to the following Activities that are the main scientific mission of the current Ph. D Thesis (See Figure 3 below):

- 01 Study and realization of Nanostructured Thin Films and Nanomaterials for consolidation and conservation of artworks
- 02 Study the use of Laser-Driven Particle sources for Cultural Heritage applications and compare them to conventional accelerators
 - a. Study the influence of particle (protons) irradiation on the stability of the artwork surface
 - b. Study of the effect of accumulated radiative dose during particle irradiation on artifacts materials

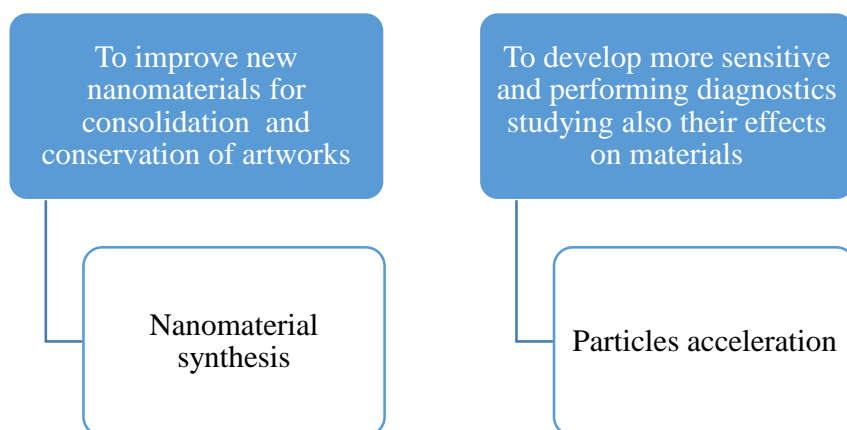


Figure 3 - Schematic representation of Thesis Main Objectives

1.2 Relevance of the Research Activity for the European Union and for Canada

In the context of the Protection of Cultural Heritage, the European Commission and its member states (including Italy) are undertaking a variety of actions with the aim of promoting and stimulating the optimal use and the resources in science and technology. Not surprisingly, HORIZON2020 is premised on the fundamental idea that setting up synergies between different communities and research domains is a key element for guiding the development of science and technology worldwide and enhancing its efficiency. In order to reinforce their statement, the European Commission plans to name 2018 the “Year of the Cultural Heritage” (see Figure 4). In the upcoming HORIZON2020 Program, the European Parliament has recently included “Cultural Heritage” as a priority in the proposed funding program of €80 bn from 2013-2020. The inclusion of Cultural Heritage in HORIZON2020 takes the form of a series of amendments focusing on the contribution of culture to research excellence, social cohesion and growth. A key section reads:

“Accessibility and preservation of Cultural Heritage [...] is needed for the vitality of engagement within and across European cultures by also considering the importance of Cultural Heritage as strong economic driver in a post-industrial economy and its contribution to sustainable economic growth.”

The sections of European interest in Cultural Heritage are specified in the “Carvalho Report Specific Program”. In particular, it can be read in the CA 18 (Industrial Leadership) the objective:

“Applying design and the development of converging technologies to, create new business opportunities, including the preservation of Europe’s heritage and materials with historical or cultural value. Protecting the Cultural Heritage: assessment, monitoring and choice of conservation materials and techniques, with reference to the environment and energy management, use and maintenance, and integration into contemporary and historical urban surroundings and archaeological and cultural contexts”.

The following project endorses fully these objectives of the European Commission. The collaboration of Universities, Research Institutes, Regional and National Agencies and, indirectly, Industry, ensures the correct use of European resources in science and technology. The research in new Materials and Methods for Cultural Heritage will contribute to protect and preserve our common historical and archaeological patrimony. Moreover, the optimization of diagnostic and conservation technique can reduce the costs of restoration and conservation, favoring their usage also for small museums and small archeological sites and ensuring the accessibility and the preservation of Cultural Heritage for all European citizens.

Moreover, the project links different communities, such as the conventional accelerator community, the nanomaterials community and the laser community, which allows for cross-linked activities on different facilities and different fields of applications that build a unique compound, currently not existing elsewhere.

The research Field of Science Applied to the Cultural Heritage is relatively new for Canada and for the Quebec. New laws on the preservation of Cultural Heritage were introduced in 2012 and the Canadian scientific community is starting to work in this new research field and new funding programs have been opened in the last three years (e.g. Coopération Québec-Italie 2014-2017 and 2017-2019 Appel à projets en art et culture dans le cadre de la Sous-commission mixte).

This Ph.D. project is the first thesis in the field of the Physics Applied to the Cultural Heritage at the INRS-EMT center and should allow for new experiments devoted to the field on the proton beam line currently under setup, with the aim of producing a “laser-driven, *few-shot PIXE*” diagnostic (first experiments were planned for second half of 2017).



Figure 4 – EU Commission proposes to designate 2018 as the European Year of Cultural Heritage

1.3 Thesis Plan and main Results

The entire research activity was organized in two main Activities, which are subdivided in different subtask. Each task corresponds to a well-defined research activity to realize the objectives mentioned before, and is structured as indicated below.

1.3.1 Activity I – Growth and Characterization of Nanostructured Thin Films and Nanoparticles for Conservation of Cultural Heritage

The duplex goal of these scientific research was: (i) the study and the synthesis of nanostructured protective films and nanoparticles for surface protection and the test of their morphological and biological properties against the more common bacteria. (ii) the use of equipment and methods that are proper of the domain of nanoscience and nanotechnology for the diagnostic and the removal of the surface corrosive patina.

The Activity I will be discussed in the Chapter 3 and the research activity performed within this topic can be summarized as followed:

01. Consolidation of ceramic artifacts using a colloidal solution of TiO_2 and SiO_2 NPs;
02. Selection of nanomaterials and hydrophobic agents for protective film realization;

03. Realization of protective film and deposition on different surfaces of interest for Cultural Heritage;
04. Testing of several deposition methods;
05. Testing of bactericidal and hydrophobic properties of protective films;
06. Studying the use of a Atomic Force Microscope as diagnostic for corrosive patina at nanometric scale;
07. Studying the use of Pulsed Laser Ablation as cleaning process on artworks and artifacts at both, nanometric and micrometric scale.

The results of Activity I produced 4 papers published in International Peer-Reviewed Journal and several participations in International Conferences (see Appendix I). The methodologies and the results, discuss in detail in Chapter 3 can be summarized as follows:

- TiO₂ and SiO₂ nanoparticle films for Cultural Heritage: conservation and consolidation of ceramic and stone artifacts (*Surface & Coatings Technology*, 271 (2015) 174–180)

The work focuses on consolidating ceramic and stone artifacts with SiO₂ and TiO₂ nanoparticles. The nanoparticles were grown by laser ablation of a solution and their shape and dimensions were monitored by optical absorption and AFM morphology studies. The colloidal solutions are mainly made out of spherical nanoparticles with diameter of about 10 nm following a LogNorm distribution with a standard deviation of about 5 nm.

The colloidal solution was then deposited on pottery and stone surfaces to obtain a transparent film with thickness of about 100 nm. The work studies the influence of the nanoparticle deposition on artifacts evaluating 1) the penetration depth of particles into porous materials with XRF and PIXE spectroscopy, 2) the hydrophobicity of deposited film with contact angle measurements, and 3) the influence of the deposition for thermoluminescence dating processes. The results show the reversibility of the thin film deposition process with laser ablation in order to ensure that there are no damages to the artifacts.

- Synthesis and characterization of thin-transparent nanostructured films for surface protection (*Superlattices and Microstructures*, 101 (2017) 209-218 ; DOI: 10.1016/j.spmi.2016.11.023; ICACC'15 Conference 2015 "39th International Conference and Expo on Advanced Ceramics and Composites)

This work demonstrates that very thin and optically transparent nanocomposite films can be conveniently applied on the surface of materials relevant for Cultural Heritage, including bronze, granite, marble, and glass, and display potent antibacterial properties without affecting the aesthetics of the underlying material. The films contain very small loadings of TiO₂, graphene, or fullerene, and can easily be applied on large surfaces using conventional brushes or air-brushes. The antibacterial properties of the films are unaffected by two accelerated aging tests, suggesting their longevity in a real world setting. These nanocomposite films are very promising candidates for the preservation of statues, mosaics, floors, buildings, and other objects that are exposed to challenging environmental conditions.

- Implementation of methods used in nanoscience as diagnostics in the field of Cultural Heritage (*AFM and Pulsed Laser Ablation Methods for Cultural Heritage: Application to Archeometric Analysis of Stone Artifacts*. *Applied Physics A* 120 (2015) 909-916; DOI 10.1007/s00339-015-9225-x)

This work introduces, for the first time, the use of the atomic force microscope (AFM) and of the pulsed laser ablation (PLA) as methods for morphological diagnostic with nanoscale precision of archeological artifacts and corrosive patina removal from stone artifacts extracted from the Church of Sotterra (located in Calabria, South Italy). The AFM microscopy was compared with different petrographic, chemical, optical and morphological analysis methods for identifying the textural characteristics, evaluating the state of preservation and formulating some hypotheses about the provenance and composition of the impurity patina located on the artifact surfaces. The results demonstrate that with the nanometric precision obtained with AFM microscopy, it is possible to distinguish the different states of preservation, much better than using conventional petrographic methods. The surface's roughness is evaluated from very small artifact's fragments, reducing the coring at micrometric scale with a minimal damage to the artworks. After the

diagnosis, we performed restoration tests using the PLA method and compared it with the more common micro-sandblasting under dry conditions. The work demonstrates that the PLA is highly effective for the removal of the superficial patina, with a control of a few hundreds of nanometers in the cleaning of surface, without introducing chemical or morphological damages to the artifacts. Moreover, PLA can be easily implemented in underwater conditions; this has the great advantage that stone and pottery artifacts for marine archeological sites do not need to be removed from the site.

- Laser Ablation Cleaning Effects on Thermoluminescence Dating Technique
(Archaeological Discovery, 2 (2014) 58-64)

Here we present the study of laser ablation (LA) restoration techniques and of thermoluminescence dating process (TL). The main aim of the work is to demonstrate that LA doesn't affect the possibility to date ceramic artifacts after restoration. We ablate Neolithic ceramics in air with a first harmonic of laser YAG (1064 nm) and dating the artifacts before and after the cleanness process. The obtained discrepancy before and after cleanness respectively is of about 200 years (3300 B.C. and 3100 B.C.), value that is below the limits of the experimental error. Moreover, the temperature of the artifacts during the LA was monitored in order to check that the temperature stayed below a certain threshold value. The results indicated that the maximum temperature reached was about 100°C, not enough to empty the metastable traps that cause the luminescence signal. Therefore the artifact can still be used for dating techniques.

1.3.2 Activity II – Laser-driven proton sources for improved and innovative Applications in Cultural Heritage

The aim of this activity is to improve the field of Diagnostic in Cultural Heritage using Laser-accelerated beams and plasma. The work focuses in particular in the design and realization of experiments on laser-driven few-shots PIXE and Cathodo-Luminescence. The experiments were performed in the laser facilities of LLNL (one shot-PIXE) and ALLS (plasma induced

luminescence). The experiments design and realization are discussed in detail in the Chapter 4, where the main research activity can be summarized as follows:

01. Study the use of laser-driven particle sources for Cultural Heritage applications and compare them to conventional accelerators;
02. Perform numerical simulations for investigating the phenomena occurring during irradiation, using Monte Carlo codes;
03. Measure the improvement and the tunability/versatility of laser-driven sources (e.g. regarding penetration depth); Design the experimental setup, realizing preliminary tests on commercial materials of interest for Cultural Heritage (i.e. bronzes, marbles, glass, etc.);
04. Perform experiments on original artworks and artifacts, demonstrating the effectiveness of new methodologies on some particular case studies; Realize monochromatic proton beams designing and realizing dedicated nanostructured target suitable for improving laser-driven proton acceleration experiments, in particular with regard to the Target-Normal-Sheath Acceleration (TNSA) acceleration mechanism, and the use of an energy selector;
05. Study a new method for performing analysis of the chemical composition and optical properties of materials using plasma induced luminescence in air.

The results of Activity II produced 3 papers published in International Peer-Reviewed Journals and several participations in International Conferences (see Appendix I with Publications and Conferences). The methodologies and the results, discuss in detail in Chapter 4 can be summarized as follows:

- Laser-Accelerated Proton Beams as Diagnostics for Cultural Heritage: One-Shot PIXE (Scientific Report, 7 40415 (2017); DOI: 10.1038/srep40415)

The aim of this study is to improve the field of Diagnostic in Cultural Heritage using Laser-accelerated beams developing of much sensitive and performing equipment for diagnostics on the different materials of interest for Cultural Heritage (i.e., stones, bronzes, marbles, pottery, etc...). This work introduces the first use of laser-generated proton beams as diagnostic for materials of interest in the domain of Cultural Heritage. Using laser-acceleration protons, as generated by interaction of a high-power short-pulse laser with a solid target, we are able to produce proton-

induced X-ray and Gamma-ray emission spectroscopies (PIXE/PIGE). Correctly tuning the proton flux on the sample, we are able to perform the PIXE in a single shot without provoking more damage to the sample than conventional methodologies. Modelling the interactions of high-fluxes (10^{13} particles shot) of ultra-short (ps-scale) tunable (keV - 60 MeV) laser-generated proton beams with the most common Cultural Heritage materials, the results show that is possible to analyze artifacts up to a depth of a few hundreds of microns with a very high precision and a beam current at least three orders of magnitude higher than conventional accelerators. The results of this work demonstrate that laser-accelerated protons can be successfully used in *one-shot* proton induced X-ray spectroscopy thus strongly enhancing the diagnostic of many materials.

- Fabrication of nanostructured targets for improved laser-driven proton acceleration
(*Superlattices and Microstructures*, 95 (2016) 159–163)

Here we present a novel realization of nanostructured targets suitable for improving laser-driven proton acceleration experiments, in particular with regard to the Target-Normal-Sheath Acceleration (TNSA) acceleration mechanism. The nanostructured targets, produced as films, are realized by a simpler and cheaper method which includes two step approach for the production of the gold nanoparticle layers: 1) Laser Ablation in Solution and 2) Spray dry technique using a colloidal solution on target surfaces of Aluminum and Mylar thin films and Carbon Nanotube buckypaper. The obtained nanostructured films appear, at morphological and chemical analysis, uniformly nanostructured without presence of oxides or external contaminants. The nanostructured layer were grown on these three materials because the wetting properties between them and the gold nanoparticles can ensure the realization of a uniform nanostructured film on the surface without local aggregation of the NPs²⁵. Moreover, these are some of the most used target materials in laser-driven proton acceleration. The obtained targets show a broad optical absorption in the entire visible region and a surface roughness that is two times greater than non-nanostructured targets, enabling a greater laser energy absorption during the laser-matter interaction experiments producing the laser-driven proton acceleration.

- Laser Stimulated Plasma-Induced Luminescence: a new method for on-air material analysis (*Applied Physics Letters*, 110 021114 (2017); DOI: 10.1063/1.49734670)

In this research activity we develop a new method for performing analysis of the chemical composition and optical properties of materials using *In-Air Plasma-Induced Luminescence*. This is achieved by interaction of a focused high-energy laser with air, interaction that produces a sub-millimetric plasma. The energetic electrons generated and accelerated in the plasma at energies higher than 5 keV reach the target surface of the sample to be analyzed, causing luminescence emission and plasmonic resonance. Each material is characterized by different chemical and optical properties that can be determined with the above-described technique. As such, our method allows obtaining an exact analysis of the sample, covering surfaces in the range of tens of mm², in only a few minutes. The results show that the acquired information is identical to what obtained with more sophisticated methods, such as SEM-Cathodoluminescence and Photoluminescence.

Chapter 2

2. State of the Art

Cultural Heritage takes up a very important worldwide role because it represents the memory, the history and the basis for the sustainable development of the human society. The world is rich and abundant in various cultural heritage buildings, monuments and objects of different sizes; each of these artworks is the fingerprint of a local culture. Our Heritage constitutes the root of present and future cultures, and it can and has to be protected and transferred to the future generations through the scientific skills.

Physical methods applied to the Cultural Heritage became, in this general view, increasingly important and more frequent. Today, it is necessary to perform any restoration process using scientific criteria. In order to do so, there is the crucial need of having as much information as possible about the artwork to get knowledge about the past and current state. Therefore, these methods allow answering questions about the state of deterioration of the work of any previous restorations, and the authenticity of the artifact etc. In recent times, the scientific applications in archaeology are heavily increasing and their particular role in connection with Cultural Heritage is also called *Archaeometry*. Literally, *Archaeometry* means *measurement on ancient objects* and Physics and Chemistry give a fundamental contribution to solving problems associated with the conservation and restoration. *Archaeometry also includes* the scientific study of an artifact based on the radiation-matter interaction and allowing getting any kind of information about the chemical compositions, the physical properties and the dating of the artifact. The modern approach of studying Cultural Heritage is highly interdisciplinary and in the last decades strong effort has been put into this research area.

Many groups currently explore the possibility to realize equipment for diagnostic and conservation that can be used directly in situ (i.e. in the archeological sites or in museums). As mentioned in the previous chapter, chemical information on artworks (ceramic, bronzes, metals, pigments) is, mainly, obtained using surface spectroscopies (such as Photoluminescence, Raman, X-ray photoelectron spectroscopy (XPS), X-Ray-Fluorescence (XRF), Energy Dispersive X-ray Fluorescence (EDX)) in SEM), while morphological information can be obtained with SEM.

Complete chemistry of material bulks is acquired using sophisticated techniques of nuclear physics such as Proton Induced X-ray and Gamma Emission (PIXE and PIGE). However, all these methods present the limiting factor of not being very tunable and adaptable (as already specified

in Chapter 1), making their use limited only to certain energy ranges and with that, to certain areas/fields of interest.

Regarding the conservation field, in the last years many research groups have studied the methods to improve materials for the consolidation and conservation of the artifacts. The current research is based on the fabrication of different protective layers. Some of the layer developments warrant the protection of the surface against condensed water¹, or against organic contaminants and environmental toxins², others employ the well-known photo catalysts activity of some nanomaterials to realize an hydrophobic and biocidal coating³. Other layer developments include Si-based resins⁴ to realize a protective coating for atmospheric pollutants, Oil-in-water (o/w) micro emulsions or micellar solutions⁵ for the solubilization of acrylic and vinyl polymers and the development of new protective films with very low environmental impact, New cellulosic titanium dioxide nanocomposite⁶ is employed for the protection of paper based materials against the damaging effect of ultraviolet radiation, pollutant gasses, mold and bacteria. All these methods allow to preserve the surfaces; some, specifically, are dedicated to the hydrophobicity while others to the bactericidal activity or to the polluted atmospheric environment.

This Chapter gives an overview of the main existing scientific methods applied to the diagnostic, the restoration, and the protection of Cultural Heritage.

2.1 Diagnostic methods: state of the art and experimental setups

This first paragraph describes all the diagnostic techniques. The techniques will be described from a theoretical point of view, besides the description of the experimental setups finishing with the explanation of the PIXE and Photoluminescence spectroscopies, which are the two methods we have proposed to improve in the present study. The paragraph closes with a briefly summary shown in a table 1 of all the mentioned diagnostic techniques.

2.1.1 Scanning Electron Microscope (SEM) coupled with Energy Dispersive X-Ray (EDX) spectrometry

The scanning electron microscopy (SEM) is not only used to define the chemical composition of the material but also the surface morphology. This technique allows to acquire information about the topography of the sample underlining the texture (up to a few nm) and morphology: shape,

size and arrangement of the particles that make up the material. The ability of this instrument to provide very realistic images of the test sample with a high definition is due to employment of electronic waves instead of light waves (see Figure 1 below).

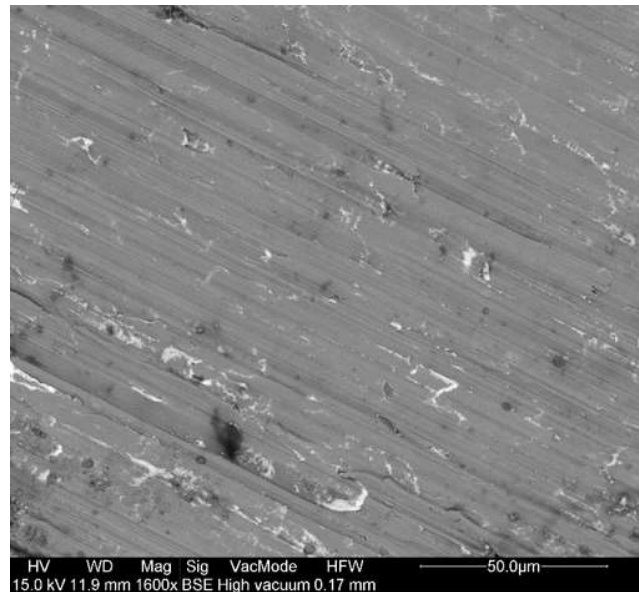


Figure 1 - SEM image

An electron gun (see Figure 2) contains a tungsten filament (cathode), which is displaced in the vacuum. When traversed by a current, this filament becomes incandescent and starts emitting electrons, which are accelerated and focused into a thin beam by means of electromagnetic lenses. Moreover, the beam's impact position on the sample surface, and then the scanning of the area, are controlled by electronically driven deflection coils. The image is acquired by secondary electrons emitted point by point from the sample surface hit by the primary electron beam^{7,8}. Finally, the achieved image is a morphological image, constituted by secondary electrons emitted from the surface, point by point.

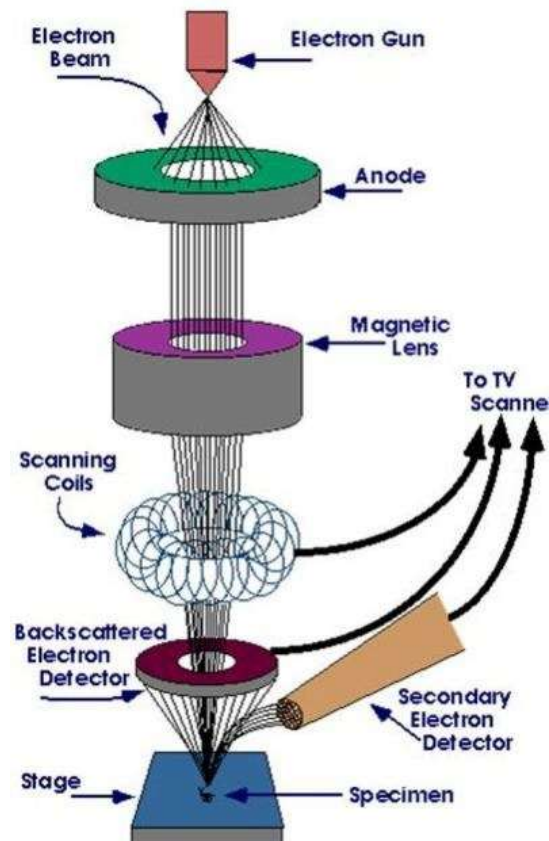


Figure 2 - Electron gun

The high-energy electron beam (20 eV) interacting with the sample surface generates a series of signals:

- *Secondary electrons (SE)*: originate from a depth of a few nm, have low energy and are mainly issued by the Auger effect⁹. The collision of primary electron creates an electronic vacuum in a solid inner band. This band can be filled by decay of an electron from a higher band, with energy transfer liberated to an electron so that it can be expelled from the solid. The secondary electrons provide information on the surface topography and the electric or magnetic fields distribution.
- *Electron back-diffused (BSE)*: derived from elastic interactions of the primary beam with the nuclei of the atoms in the sample. . These electrons allow obtaining information about the average atomic number, the crystalline structure and topography of the scanned area of the sample.

- *X-rays*: produced by fluorescence. They are characteristic of the elements making up the sample. The intensity of these radiation characteristics is proportional to the element concentration in the sample¹⁰.

Microanalysis X-ray (Energy Dispersive X-ray- EDX) gives specific information on the chemical composition of the elements in the sample, in terms of quantity and distribution, by measuring the X-rays emission following the bombardment with a high-energy electron beam. The microanalysis is realized by means of a microprobe applied to the scanning microscope, comprising a window permeable to X-rays¹¹. All elements having atomic numbers from 4 (Be) to 92 (U) can be detected, though not all instruments are equipped for 'light' elements ($Z < 10$). Qualitative analysis involves the identification of the lines in the spectrum, which can be quite easily performed due to the uniqueness of the X-ray spectra for each element. Quantitative analysis (determination of the concentrations of the elements present in the sample) entails measuring the line intensities (height of the line) for each element in the sample. Additional calibration allows measuring the percentage contribution of each element.

The EDX spectrum (shown in 2D images or 'maps', see Figure 3) can be obtained by scanning a single point or the whole area investigated by the microprobe and displaying the intensity of a selected X-ray line.

Three devices essentially constitute the experimental setup for EDX:

- *Electron microprobe*: it is a system for the beam formation. It generates electron beams characterized by high density, current stability and small diameters that may vary depending on the experimental setup used and that are adapted to obtain the highest possible resolution.
- *X-ray detection systems*: the detector is made of a single crystal of Si doped with Li. The detector allows the realization of a graph, where each peak corresponds to a specific chemical element.
- *Analysis of the detected X-rays*: the amplified signal from the detector is conveyed into a device called multichannel analyzer (MCA), which acts as an analog-digital converter and sends the signal coming from the amplifier in discrete energy channels, whose amplitude is usually of 10 or 20 eV. The signals of the X-rays are then distributed according to their energy, thus obtaining the X-rays spectrum. The MCA is integrated in a computerized system that allows to display the obtained spectrum on a monitor and a post-processing of the data.

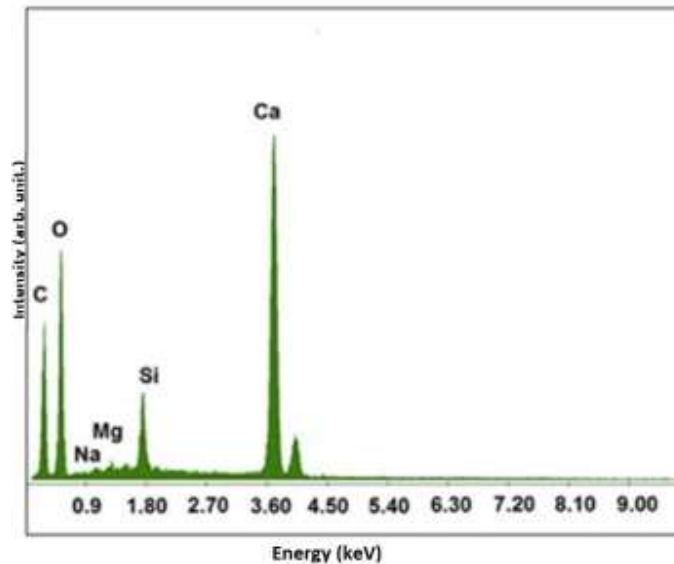


Figure 3 - EDX spectrum

2.1.1.1 The SEM and EDX experimental setup used in this work

The equipment used for most of the analysis in this thesis is a FEI Quanta 200 SEM with a variable-pressure scanning electron microscope (ESEM™). The SEM images are taken under a STEREOSCAN SEM microscope working with an electron energy of 20 keV.

The Quanta SEM systems can be equipped with analytical systems, such as energy dispersive spectrometer, wavelength dispersive x-ray spectroscopy and electron backscatter diffraction.

The microprobe equipped to perform EDX analysis works with a brightness of 100 A/cm² sr, an energy spread of 2.5 -3 eV and a source size of 50 nm.

2.1.2 Raman

Raman microscopy is a spectroscopic technique used to observe vibrational, rotational, and other low-frequency modes in a system¹². It provides information on the atom vibrations in a crystal lattice by studying the inelastic and Raman scattering of a monochromatic light (usually a laser in the visible range). The laser light interacts with molecular vibrations, phonons, or other excitations in the system, and the produced shift in energy gives information about the vibrational modes in the system¹³.

In this present thesis, we have not used this technique.

2.1.3 X-ray Photoelectron-XPS

The X-ray photoemission spectroscopy (XPS) allows the determination not only of the chemical species present, but also the nature of the bonds in which they are involved, through the position analysis (chemical shift) of photoelectric peaks compared with tabulated values referring to the pure atomic species^{14,15}.

The XPS measures the kinetic energy and the number of electrons that are emitted from the surface of a sample after the irradiation with a beam of X-rays¹⁷ (Figure 4).

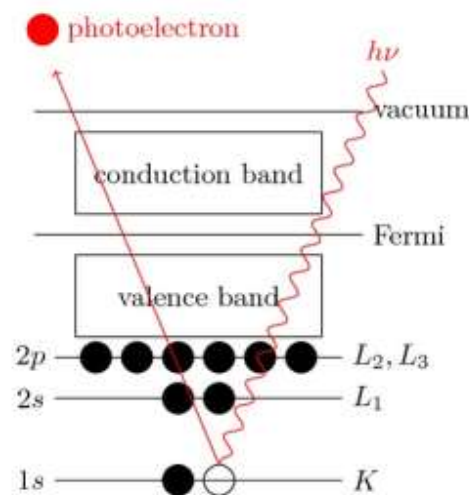


Figure 4 - Sketch of electron photoemission

The XPS is based on the *photoelectric effect*: a photon, of well-defined energy $h\nu$ and hitting a solid material, penetrates into the surface and is then absorbed by an electron. If the photon has a sufficiently high energy then the excited electron will emerge from the surface with a kinetic energy approximately equal to:

$$E_K = h\nu - E_B - \phi_S \quad (1)$$

where ϕ represents the work function of the solid, E_B the energy of the electron bond in the solid, and $h\nu$ the energy of the X-ray source.

From the above equation it is possible to conclude that, by measuring the kinetic energy (E_K) of the emitted electrons, one can retrieve the initial state energy (previous excitation), provided that the electron reaches the analyzer. This, since the electron will endure a variation of energy equal to

$$E_K = h\nu - E_B - \phi_a \quad (2)$$

due to the difference between the sample and the analyzer work functions.

From the description of the *photoelectric effect*, the distribution of electron energy photo-emitted directly represents the distribution of the electronic states of the surface of the solid (less than an amount equal to $h\nu$)¹⁶. The photoelectron spectrum can then be interpreted as a reflection of the orbital diagram: each band of the photoelectron spectrum corresponds to the ionization of a single orbital and each orbital occupied with binding energy less than $h\nu$ gives rise to a band in the spectrum.

The photoemission model described by equation (1) is known as an approximation to an electron. The spectrum (typical of the metals of the second column) is usually dominated by a few very narrow and intense peaks, which originate from the electrons emission from the *core* levels of the surface atoms, by the emission of electrons from the valence band, by some secondary structures that are attributable to the plasmons, to Auger electrons¹⁷ generated from vacation left after the emission of an electron from a *core* layer and at secondary electrons derived from inelastic processes.

The basic components of the XPS are:

- *Vacuum system*: this system involves the use of three pumps, which work according to three different principles (a mechanical rotary pump, a turbo molecular pump and a ionic pump)
- *Excitation source*: as X-ray source, in the XPS instruments are used the emission lines of a metal target called anode, which are subjected to bombardment with electrons having energies of the order of tens of keV. The energy of these lines, resulting from electronic transitions, depends only on the energy level of the anode component atoms. The bombarded anode causes the emission of characteristic radiation of the bombarded

element. This characteristic radiation is superimposed on a continuous spectrum called *Bremsstrahlung*, which depends on the energy of the incident electrons. Anodes available on the instrument at our disposal are aluminum ($K\alpha = 1486.6 \text{ eV}$)¹⁸ and magnesium ($K\alpha = 1253.64 \text{ eV}$)¹⁸ since these two materials guarantee characteristic peaks with an energy that allows to excite the deepest core level of all elements of the periodic table.

- *Electron energy analyzer*: the hemispherical electron analyzer (EA) is a tool that allows measuring the energy of a charged particle. The EA consists of two metal hemispheres on which a potential difference is applied so that only the charges with a determined energy (E) are able to have a curvature that allow them to reach the other terminal of the analyzer. The condition is:

$$\Delta V = V \left(\frac{R_1}{R_2} - \frac{R_2}{R_1} \right) \quad (3)$$

Where $E = qV$

This passing energy is called *Energy pass*. Over the output terminal of the charges, there is a channeltron that consists of a glass tube, whose walls are coated with a highly resistive materials. In this way, whenever the wall is hit by an electron, this will provoke an avalanche breakdown mechanism and for each electron entering in the channeltron, the number of generated electrons is about 10^4 . The resulting current is then transformed into a series of pulses whose frequency is proportional to the intensity of the initial current.

- *Acquisition system detection signal*: the data acquisition is performed by employing a computer with Keithley interface. Through the interface, one can send the voltage to the analyzer lenses to fix the analytical power and receive its signals. Final data are the average of several acquisitions in order to reduce the effects of noise.

2.1.3.1 The experimental setup used in this work

XPS experiments are conducted in a UHV chamber equipped for standard surface analysis with a pressure in the range of 10^{-9} Torr by a non-monochromatic Mg-K α X-ray ($h\nu = 1253.64$ eV). The energies of XPS spectra are calibrated with the C 1s peak of a pure carbon sample (binding energy of 284.6 eV).

2.1.4 X-Ray Fluorescence (XRF)

The X-ray fluorescence (XRF) allows to attain the elemental (qualitative and quantitative) composition of a material. Since this method is fast and non-destructive to the sample, it is commonly used for applications in the field of Cultural Heritage.

The XRF technique is based on the “*photoelectric effect*”: when a primary X-ray excitation source from an x-ray tube or a radioactive source strikes a sample, if the primary x-ray has sufficient energy, it is absorbed by the atom by transferring all of its energy to an innermost electron. During this process, electrons are ejected from the inner shells, creating vacancies that are an unstable condition for the atom.

When the atom returns to its stable condition, electrons from the outer shells are transferred to the inner shells and in the process, giving off a characteristic x-ray whose energy is the difference between the two binding energies of the corresponding shells. The emitted x-rays produced from this process are called “*X-ray Fluorescence*,” or *XRF*. The process of detecting and analyzing the emitted x-rays is called “X-ray Fluorescence Analysis.” In most cases, the innermost K and L shells are involved in the XRF detection (see Figure 5). A typical x-ray spectrum from an irradiated sample will display multiple peaks of different intensities (see Figure 6).

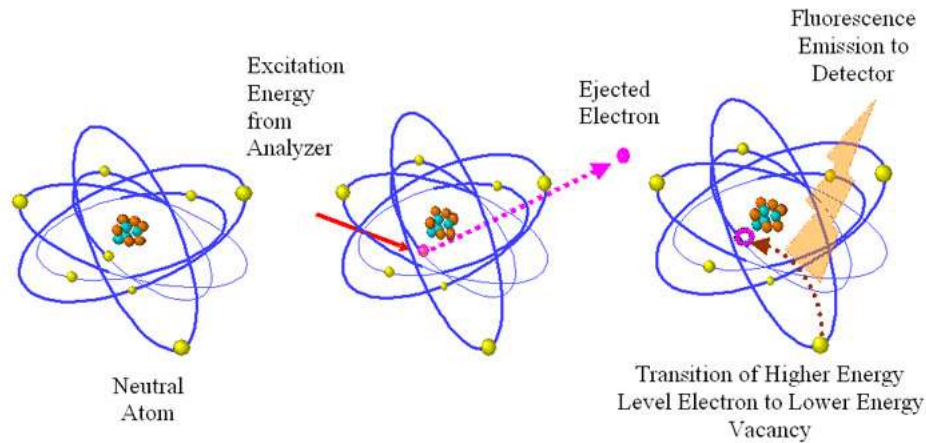


Figure 5 - Sketch of X-ray Fluorescence spectroscopy

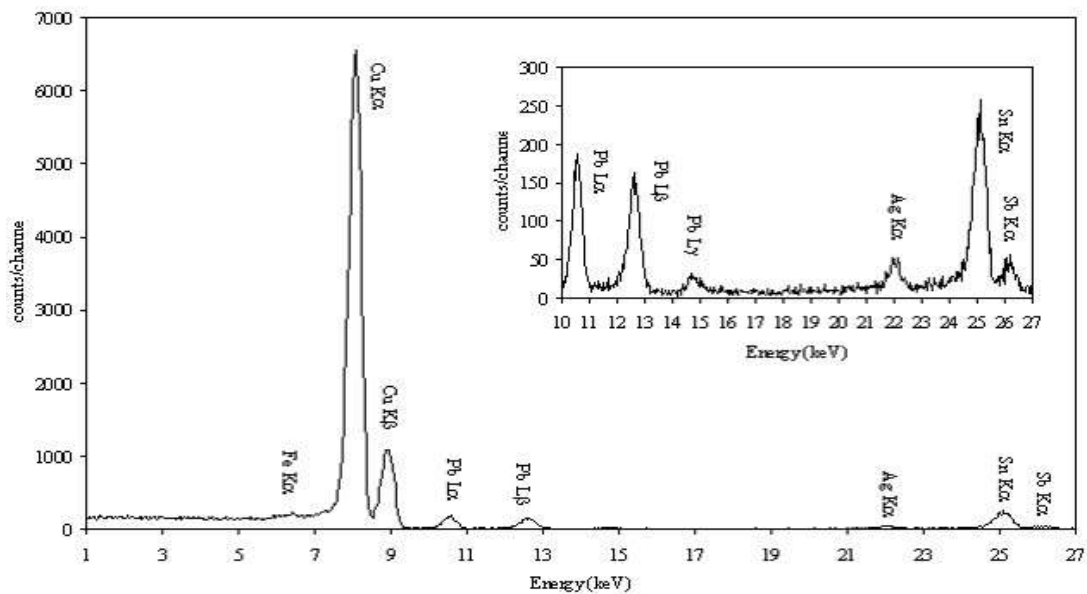


Figure 6 - XRF spectrum of a bronze statue

The characteristic x-rays are labeled as K, L, M or N to denote the shells they originated from. Another designation alpha (α), beta (β) or gamma (γ) is made to mark the x-rays that originated from the transitions of electrons from higher shells. Hence, a $K\alpha$ x-ray is produced from a transition of an electron from the L to the K shell, and a $K\beta$ x-ray is produced from a transition of an electron from the M to a K shell, etc. Since within the shells there are multiple orbits of

higher and lower binding energy electrons, a further designation is made as α_1 , α_2 or β_1 , β_2 , etc. to denote transitions of electrons from these orbits into the same lower shell.

The components of a XRF spectrometer are:

- *Primary X-rays source*: is composed of a cathodic tube able to operate at high values of potential difference and of an anticathod made of Au.
- *Sample holder chamber*
- *Collimator system*: they are usually constituted of several parallel foils that are used to make parallel the obtained X-rays
- *Analyzer crystal*: it allows the identification of the elements by diffracting the secondary X-ray radiation coming from the sample
- *Detector*: it is composed by a counter able to distinguish the different wavelengths and intensities of the collected X-ray radiations, showing them as peaks¹⁹.

2.1.4.1 Experimental setup used in this work

XRF measurements were conducted by the X-123 SDD apparatus by Amptek (USA), equipped by a gold cathode and a beryllium revelator, operating at fixed angle.



Figure 7 - XRF portable setup

The device used for the XRF measurements is shown in Figure 7, and is composed by a “Mini-X” X-ray generator mounted on a MP1 tube equipped with X-123SDD detector. Mini-X is a self-contained, miniature X-ray tube system, which includes the X-ray tube, high voltage power supply

and USB controller.. It features a 50 kV/80 μ A power supply, a gold (Au) or silver (Ag) transmission target, and a beryllium end window. The Mini-X is designed to generate voltages up to 50 kV. Beryllium window is on the front of the unit. The Mini-X is provided with two collimators.

The X-123SDD combines in single package Amptek's high performance X-ray spectroscopy components: (1) the XR-100SDD silicon drift X-ray detector and preamplifier, (2) the DP5 digital pulse processor and MCA, and (3) the PC5 power supply. The X-123SDD uses a silicon drift detector (SDD) to improve the energy resolution and increase the count rates. The pulse processor is the DP5. The DP5 digitizes the preamplifier output, applies real-time digital processing to the signal, detects the peak amplitude, and bins this in its histogram memory. The spectrum is then transmitted to the user's computer.

2.1.5 Photoluminescence

The Photoluminescence technique, widely used in the field of Cultural Heritage, is employed to identify mineralogical phases present on the surface of the materials, the presence of any coatings, "alteration patinas" or extrinsic too.

The *luminescence* is a phenomenon by which the radiative charge transitions happen with emission of electromagnetic radiation in the visible region and close to it (infrared and ultraviolet) as a result of the passage of radiative charged from the excited states to those with a lower energy.

If the emission process stops with the cause exciter, i.e. between the absorption and re-emission there is only the time interval necessary for the atomic transition ($\tau_c < 10^{-8}$ s), then a *fluorescence* process occurs. If the state of excitation is metastable and reissue is delayed ($\tau_c \geq 10^{-8}$ s) and the emergence issue continues even after the removal of the cause exciter, then a *phosphorescence* process occurs.

In relation to the phosphorescence the energy levels diagram phenomenon present a metastable *m* level in the band gap between *e* and *g* (see Figure 8). An electron excited to *g* can be trapped in *m* where it can remain until it receives an energy *E* sufficient to get it back in *e*; from here there can be a transition to *g* with emission of light.

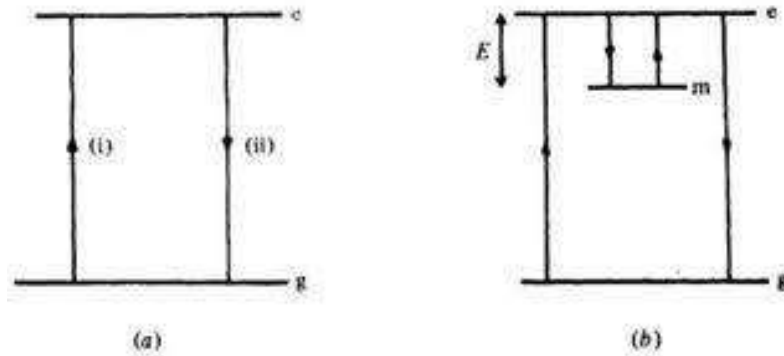


Figure 8 - Energetic transition involved in the production of fluorescence (a) and phosphorescence (b)

The delay that is observed in the phosphorescence phenomenon corresponds to the time that the electron spends in the trap for electrons m . The average life spent in the trap at the temperature T is given by:

$$\tau = S^{-1} \cdot e^{\frac{E}{kT}} \quad (4)$$

32

Where s is a constant called *frequency factor*, expressed in s^{-1} ; E is called the *trap depth* (energy difference between m and e); k is the Boltzmann constant.

The phosphorescence process has an exponential temperature dependence. The complete model, based on the theory of energy bands is the result of the study by Randall and Wilkins²⁰.

Randall and Wilkins assume that, when the electron is freed from the trap ($m \rightarrow e$, Figure 8b), the probability that it returns to the ground state ($e \rightarrow g$) is much higher than the probability that it is trapped. The intensity of phosphorescence is proportional to the rate of recombination ($e \rightarrow g$). In this case the transitions involved are $m \rightarrow e$, for which $I(t)$ is proportional to the escape velocity of electrons from the trap:

$$I(t) = -C \frac{dn}{dt} = C \frac{n}{\tau} \quad (5)$$

Where C is a constant of proportionality and n is the number of electrons trapped in m . Integrating, we obtain:

$$I(t) = I_0 \cdot e^{-\left(\frac{t}{\tau}\right)} \quad (6)$$

Where τ is the average life time, t is the time and I_0 is the intensity at $t = 0$

The equation represents the decay of phosphorescence after the end of irradiation, at a constant temperature (Figure 8). The trend at constant temperature will be a simple exponential or a decay of the first order.

The implemented setup for the photoluminescence consist of:

- *Horiba Jobyn Yvon Olympus microscope*: it mounting objectives 10x, 50x, 100x. The microscope is equipped by a laser source by a Triax 320 (Horiba-Jobyn-Yvon) for the processing of the optical signal.
- *Optical detenction system*: it is composed of a monochromator in series to a CCD. The monochromator (is composed by some toroid mirrors that focused the input signal on a turret with three different diffraction gratings decomposing the signal into its components in various wavelengths) that focus the input signal, transfer it to the CCD (which is a Si wafer detector with a resolution of 1024 x 128 pixels that has the task of transforming the incoming optical signal into an electrical signal by photoelectric effect, so that it is interpretable by the appropriate software). The sample positioned in the housing of the microscope is focused via remote with the 100x objective through a camera connected to a computer. After focusing the sample, due to the optics of the microscope, is sent on a UV laser beam (incidence angle zero), with respect to the normal of the sample. The photoluminescence signal is then collected and sent through an optical system (including a notch filter that excludes the output laser frequencies, to avoid overlap between the input signal and signal output) to an optical fiber that is connected to the entrance slit of the spectrometer.

2.1.5.1 Experimental setup used in this work

Photoluminescence (PL) measurements were taken by an Olympus microscope (Horiba-Jobyn Yvon) mounting objectives of 10×, 50× and 100× magnifications. The microscope is equipped by a 375 nm-laser source with a power of 15 mW for the generation of photo-luminescence, and a Triax 320 that works in the 200 - 1500 nm range.



Figure 9 - Photoluminescence setup for our experiments

2.1.6 Proton Induced X-ray Emission- PIXE

Particle-induced X-ray emission called PIXE is a technique that allows to investigate the elemental (qualitative and quantitative) composition of trace elements (ppm) of a wide range of material and then very important in the Cultural Heritage field. The advantages of this method are many, as high sensitivity (offers better peak to noise ratios and consequently much higher trace element sensitivities), multi-element analysis and measurements at atmospheric pressure.

PIXE is an elemental analysis technique which employs a charged particle beam from an accelerator to excite characteristic emission from the constituents of a material. When a material is exposed to an ion beam, atomic interactions occur, emitting x-rays that are specific to an element. In details, when the ion beam interact with a material, it creates electron “vacancies” in the inner atomic energy levels (the so called K, L and M shells) by ejecting one or more of its most tightly bound electrons out of the atom²¹ (Figure 10).

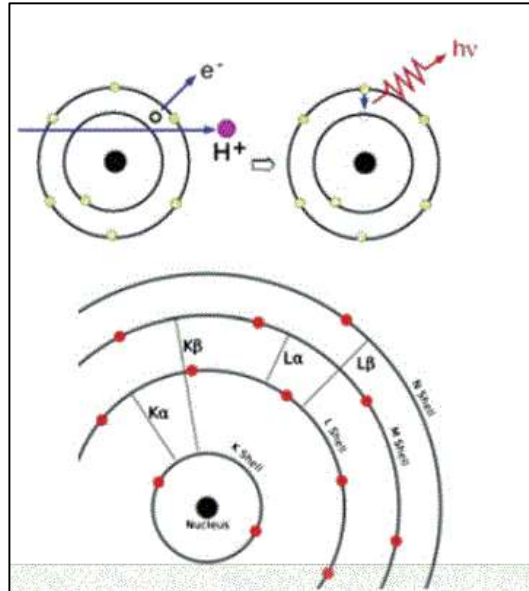


Figure 10 - Sketch of atomic proton interactions and electronic transitions between K, L and M atomic shells

When a beam of heavy charged particles of a few MeV per atomic mass unit penetrates into matter (considered as a compound), it gradually loses its energy with depth, until it is finally stopped. The energy loss occurs mainly through inelastic Coulombic encounters with bound electrons, and in contrast to the case of electron beams, the direction of travel of an ion beam is scarcely altered during the slowing-down process. The stopping power $S(E)$ of an ion with energy E is defined as the energy loss per unit mass thickness traversed:

35

$$S(E) = -\frac{1}{\rho} \frac{dE}{dx} \quad (7)$$

where ρ is the density of the stopping material and x is the distance. As defined here, $S(E)$ is expressed in units of kiloelectron volt per gram per square centimeter. For the energy range of 1-4 MeV, which is the most important in PIXE, the uncertainty of the values calculated with the semiempirical equation is estimated to be less than 3%.

The stopping power for compounds or more complex matrices is obtained from those of the constituent elements through the Bragg-Kleeman additivity rule:

$$S_{matr}(E) = \sum_{i=1}^n w_i S_i(E) \quad (8)$$

where w_i and $S_i(E)$ are the mass fraction and stopping power of constituent element i , respectively.

The total path length R of an ion may easily be obtained by integration of the stopping powers:

$$R = \int_{E_0}^0 ab - \frac{dE}{S(E)} \quad (9)$$

where E_0 is the incident ion energy. Although the total path length is larger than the projected range, the difference between the two is smaller than 1% for the incident protons of a few megaelectron volts (MeV).

Many of the Coulombic interactions between protons or heavier ions and matter results in the ejection of inner-shell electrons. Those interactions and their cross sections are important in PIXE. Calculation of the x-ray production cross section from the ionization cross sections involves different atomic parameters; that is, fluorescence yields and fractional radiative widths in the case of the K shell, and fluorescence yield, Coster-Kronig yields, and fractional radiative widths for the L shell. As to the K fractional radiative widths, either the experimental data of Salem et al²² or the theoretical values of Scofield²³ that are derived from Dirac-Hartree-Fock (DHF) calculations are considered accurate within 1%.

There is, however, a small failure of the theory in the atomic number region $22 < Z < 30$, where experimenters²⁴ agree on a deviation of a few percent. The K fluorescence yields are usually taken from Krause²⁵. These data are quite accurate for atomic numbers above $Z=20$, but the situation for the lighter elements is less clear²⁶. For these lighter elements, one currently prefers the data from Hubbell²⁷. From the case of the L x-rays, Cohen and Clyton²⁸ and Cohen²⁹ suggest employing the fractional radiative widths of Salem et al¹², and the Krause¹⁵ fluorescence and Coster-Kronig yields, and Cohen and Harrigan³⁰ used this approach to convert their table of ECPSSR L ionization cross section³¹ into a very useful table of production cross sections for up to 16 individual L x-ray lines.

A very practical alternative to tabulated theoretical ionization and x-ray production cross sections, particularly with computer calculations in mind, are parameterized or analytical formulas which are obtained by fitting polynomial expressions to theoretical or empirical cross-sectional data. The equations derived by Johansson and Johansson³² have been widely used for the PIXE analysis in the past, but it is now known that they progressively underpredict cross sections with increasing Z of the target element.

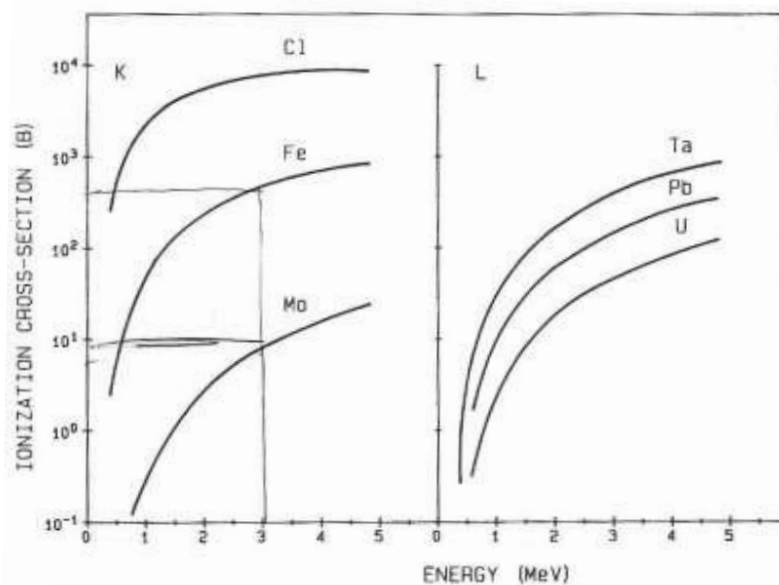


Figure 11 - K and L shell ionization cross sections in barns (1 barn= 10^{-24} cm²) as a function of proton energy and target atom. The values are theoretical ECPSR predictions (Cohen and Harring, 1985)

For the proton energy range of 1-4 MeV typically used in PIXE, the ionization (and x-ray production) cross sections increase with increasing proton energy and decrease with increasing atomic number of the target atom. This is illustrated in Figure 11, which displays theoretical K and L shell ionization cross sections²¹ for the selected target elements.

The very steep fall in the K ionization cross section with Z is particularly notable. Protons or other heavy charged particles that pass near atomic nuclei can be scattered elastically (i.e., without causing nuclear or atomic excitation). The cross section for the elastic scattering is strongly dependent on the scattering angle and on the atomic number (Z) of the scattering nuclide; it decreases with increasing angle and increases with increasing Z . The energy of the scattered particles also increases with Z . By measuring the elastically scattered particles, information can be

obtained on the elemental composition of the sample and on the distribution of the elements within a certain depth.

In addition to elastic encounters between incident particles and target nuclei, various inelastic interactions or nuclear reactions are possible. These both include (p, γ) , $(p, p'\gamma)$ and $(p, \alpha\gamma)$ nuclear reactions when protons are used as incident particles. The cross sections for those reactions do not vary in a regular way with target nuclide and with incident particle energy. The cross sections generally increase with increasing incident particle energy but may exhibit intense resonance peaks at particular energies. In addition, because of the Coulomb barrier, the cross sections are smaller for the heavier target elements than for lighter ones.

By detecting the promptly emitted γ -rays or charged particles for the above-mentioned nuclear reactions, an elemental analysis and the depth profiling of certain elements is possible. The analytical technique that employs these possibilities is referred to as nuclear reaction analysis.

2.1.6.1 Classical instrumentation

The ion beam used for the PIXE analysis is produced by a conventional accelerator. The energy range required, 1-4 MeV/u, means that relatively small (i.e. Accélérateur Grand Louvre d'Analyse Élémentaire called AGLAE - C2RMF in France allows to obtain several beam spot diameters from 20 μm to 500 μm , current intensities from 2 to 10 nA, with dimension of about 40 meters) accelerators are sufficient. Electrostatic accelerators are suitable sources³³ and electrostatic accelerators are most commonly used for this purpose. They may be of a regular or modified Van de Graaff type, in which a high-voltage terminal is charged by a belt or a metallic chain. A second type of electrostatic accelerators uses a high-frequency voltage multiplication stage to charge a cavity, with the ions being accelerated in the electrostatic field created by the cavity.

Usually, in order to perform PIXE, a single-ended or tandem electrostatic machine of 2-3 MeV is chosen. Certain types of analysis, such as analyses by micro beam techniques, impose special requirements on ion source brightness, energy stability, beam emittance, and minimum scattering of the ion beam. Such requirements may play an important role in selecting an accelerator.

Commercially available vacuum chambers used as scattering chambers in nuclear physics experiments are generally not well suited for PIXE. Their shapes and dimensions hamper obtaining large solid angles for detection and introducing multi specimen holders and sample charges.

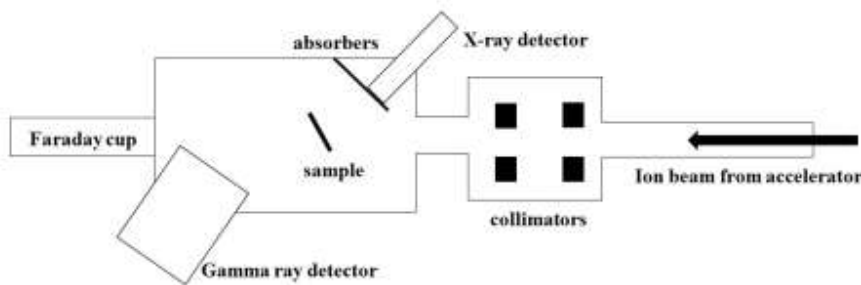


Figure 12 - Typical experiment arrangement for routine PIXE, with detectors for x-rays and γ -rays

As a consequence, few existing PIXE chambers are of commercial origin. Figure 12 shows the design and principal components of a “typical” setup for PIXE analysis. The ion beam emerging from the accelerator first passes through an analyzing magnet, which sorts out the ions with the desired mass and velocity, and then is focused by electrostatic or magnetic quadrupole lenses onto the specimen.

After exiting the gun, the round ion beam is confined by a pair of quadrupoles (collimators), which are placed approximately 100-200 mm apart, just before the entrance to the irradiation chamber. A target holder defines the proper position of the sample during the analysis. The samples are irradiated to a variable angle (to detect the x-rays)

PIXE spectra have most of their x-ray intensity in the low-energy region, so that the spectral shape can advantageously be modulated by placing an x-ray absorber between the sample and the detector. The aim of absorbers is to reduce or eliminate unwanted continuum background and /or intense x-ray peaks and their associated pileup peaks. At the same time, the absorbers allow for ion bombardments at higher beam intensities, so that the elements of interest can be measured in shorter bombardment times and with fewer spectral interferences.

The absorbers are usually made from organic material (e.g., Mylar) or from light-element metal foils (Be and Al). Plain absorbers are employed if a complete elimination of the low-energy part of the spectrum is desired. In PIXE of thin specimens, the ions pass through and are dumped in a Faraday cup for charge integration. The charge integration itself is accomplished by connecting the Faraday cup to a sensitive current integration/digitizer.

2.1.7 Overview of the different diagnostic techniques used in the Cultural Heritage field

Table 1: brief description of the diagnostic techniques used in the Cultural Heritage field

<i>Techniques</i>	<i>Purpose</i>	<i>Operating Principles</i>	<i>Used Equipment and Parameters</i>	<i>Limits</i>
<i>Scanning Electron Microscope (SEM)</i>	Investigation of surface morphology, shape, size and features of the materials	The emitted electrons (from an incandescent filament) impact on the sample surface. The image (containing the morphological information) is reconstructed by secondary electrons emitted from the surface (point by point)	FEI Quanta 200 SEM with a variable pressure scanning and an electron energy of 20 keV	- The scanning depth is only about a few nm with an average resolution of 2,5 nanometers and a maximum scanning area of about 150×150 micrometers - To perform the SEM imaging, it is necessary to take micro sampling
<i>Atomic Force Microscope (AFM)</i>	Investigation of surface morphology (including three dimensional), shape, size and features of the material imaged with nanoscale precision	It operates by measuring the force between a probe (called tip) and the surface material. The morphological image is obtained by measuring the vertical and lateral deflections of the tip by using the optical tool.	ICON Bruker AFM microscope with a resolution of 512 x 512 pixels and a frequency of about 1 Hz	- Can produce images with resolution on the order of fractions of a nanometer on an area of a few microns, with a penetration depth of about 15-20 μm - To perform the AFM imaging it is necessary to take micro sampling
<i>Energy Dispersive X-ray spectroscopy (EDX)</i>	Investigation of the chemical composition of the elements within a material in terms of: quantity and distribution	It measures the x-rays emitted from the surface after bombardment with a high energy electron beam	FEI Quanta 200 SEM with a variable pressure scanning with an electron energy of 20 keV	- Can detect elements having atomic numbers from Beryllium (4) to Uranium (92), with a penetration depth up to μm - To perform the EDX analysis it is necessary to take micro sampling
	Investigation of the chemical species present on	It measures the kinetic energy of the electrons	UHV chamber with a pressure in the range of 10E-9	- The scanning depth is about 9 nm

<p><i>X-ray Photoelectron spectroscopy (XPS)</i></p>	<p>the sample surface, and nature of their bonds (performed by chemical shift)</p>	<p>emitted from the sample surface, after the irradiation of the sample using X-rays</p>	<p>torr; production of X-rays by a non-monochromatic Mg-Kα X-rays ($h\nu= 1253.64$ eV)</p>	<ul style="list-style-type: none"> - Can detect chemical species present and nature of the bonds, giving information on the chemical oxidation states of the various elements - To perform the XPS analysis it is necessary to take micro sampling
<p><i>X-ray Fluorescence spectroscopy (XRF)</i></p>	<p>Investigation of the elemental (qualitative and quantitative) composition of the materials by measuring the fluorescent (or secondary) X-ray emitted from a sample (solid, liquid or powder) when it is excited by a primary X-ray source</p>	<p>It is based on the emission of characteristic secondary (or fluorescent) X-rays from a material that has been excited by bombarding with high-energy X-rays or gamma rays.</p>	<p>X-ray generator (voltages up to 50 kV) mounted on X-123 SDD detector by Amptek (USA), equipped with a gold cathode and a beryllium revelator, operating at fixed angle</p>	<ul style="list-style-type: none"> - Can detect elements having atomic numbers from Sodium (11) to Uranium (92) -Cannot detect the aggregation state of the different elements
<p><i>X – ray Diffraction</i></p>	<p>Identification and distinction between amorphous and crystalline material, quantification of the percent of crystallinity of a material</p>	<p>It is based on the constructive interference (and diffracted X-rays) of monochromatic X-rays and a crystalline material, when Bragg’s Law is satisfied.</p>	<ul style="list-style-type: none"> - Copper is the most common target material used for single-crystal diffraction, with Cu Kα radiation = 1.5418Å - For typical powder patterns, data is collected at 2θ from ~5° to 70° 	<ul style="list-style-type: none"> -The technique is limited by the fact that to identify the crystalline structure of the material, the material must be homogeneous with only one crystal lattice structure. - In order to obtain information on a crystal lattice of a material is essential to have access to a standard reference file of inorganic compounds (d-spacing, hkl) - Requires tenths of a gram of material which must be reduced into a powder - For materials with mixed lattice

				structures, the techniques detects only the lattice materials with a concentration > 2% of sample
Photoluminescence (PL)	Identification of mineralogical phases present on the material surface, identification of defects in the crystal, doping concentration, charge carrier lifetime, and concentration of specific impurities	The radiative charge transitions occurs with emission of electromagnetic radiation in the visible region and close to it (infrared and ultraviolet) as a result of the decay of radiative electrons from the excited states to those with a lower energy	Horiba Jobyn Yvon Olympus microscope equipped with a laser source of 378 nm, power of 12mW and a spectrometer Triax 320 (Horiba Jobyn Yvon) working in the range of 200-1500 nm for the processing of the optical signal.	- Cannot detect the aggregation state of the elements - It is only a qualitative analysis - Disappearance of the luminescence signal when the excitatory source stops (fluorescence exists when the process stops when the excitation source stops. The characteristic time when the emission occurs is for the fluorescence $\tau < 10^{-8}$ seconds for the phosphorescence that occurs also after the source stops: $\tau c \geq 10^{-8}$ seconds
Particle Induced X-ray Emission (PIXE)	Investigation of elemental (qualitative and quantitative) composition of trace elements (ppm) of a wide range of materials	When a material is exposed to a particle (in our case ion beam), the interaction between the beam and the sample results in the emission of X-ray radiation from the sample; the energy of the emitted X-ray is specific for each element	-Mean energy of the proton beam is ~ 2.5 MeV - Beam current is in the 10-150 nA range -Spectrum generated with an X-ray count rate in the order of 800-2000 counts/second	- Particle Energy ranging between 1-5 MeV -Beam current from tens of pA to nA -Long analysis time (each point 100-9000 s measuring time) -The sample adsorbs a high radiation dose -Penetration depth 20 μ m below the surface (depending on the impinging energy) -Is applicable only for local analysis (beam sizes are generally in the order of mm ²)

- Accelerator facility used for the PIXE is complex and requires a larger laboratory. To perform PIXE analysis it is necessary to move the artworks to the laboratory

2.2 Conservation Methods

Artifacts are often exposed to humidity and to harsh environmental conditions (chemical and biological). This results in the formation of a corrosive patina on the surface, which irretrievably damages the artifacts (as in the case of the bronze where the formation of a bronze disease can damage the artifacts until its complete destruction). Usually the restoration and conservation process consists in the removal of the corrosive patina, the consolidation with mortar (for stone and ceramic) and in the coating of a hydrophobic and bactericidal film. Therefore, the materials used for this purpose strongly modify the artifacts surfaces, covering decoration and pigments. Furthermore, the process is often irreversible.

Recently, nanomaterials have been proposed as substitute to resins and mortar in a reversible restoration process³⁴. In particular NPs are promising because they have dimensions between a few nm to tens of microns, so that it is possible to choose the adequate size to allow the NPs to penetrate into the porous surface to consolidate the medium.

In the following, we present an overview of Nanoscience-based Conservation methods followed by a collection of main existing results on the development of bactericidal materials.

2.2.1 Conservation techniques for Cultural Heritage and Nanoscience: an overview

Stone, ceramic and bronze monuments exposed outdoors are susceptible to several decay phenomena, including microorganisms colonization and its consequent surface transformation (color degradation, corrosive patina formation, etc.)^{35,36,37}. A common restoration intervention includes the following phases:

- a) Removal of pre-existing alterations (deposits, crusts, biological patinas);
- b) Consolidation through application of suitable inorganic and organic products;
- c) Filling cracks and fissures with compatible products that do not alter the stability and the general vision of the monuments itself;
- d) Application of biocide products alone, or in combination with protective or consolidants to prevent further colonization^{38,39,40}.

This latter aspect, which aims to prevent the re-colonization of restored surfaces, is very important and has gained more attention due to the fact that the products used for the conservative purpose may serve themselves as nutrient and thus support the re-colonization of the newly restored surface. Several studies evaluate the bio deterioration resistance of already available products used in the different phases of the conservative process^{41,42}.

Moreover, photo-inactivation properties of titanium oxide (TiO₂) have been extensively evaluated in the last 25 years in attempt to develop new alternative safety and environmental friendliness approaches for disinfection^{43,44}. In this context, TiO₂ is one of the most fascinating materials characterized by chemical stability, non-toxicity, high photo-reactivity, broad-spectrum antibiosis and cheapness, and it has been used extensively as biocide against various microorganisms: bacteria, fungi and viruses^{45,46}.

When TiO₂ is exposed to ultraviolet (UV) light ($\lambda < 400$ nm), holes (h⁺) and excited electrons (e⁻) are generated. The holes are capable of oxidizing water or hydroxide anions into hydroxyl radicals (-OH). The produced free radicals can decompose a wide range of organic compounds. The antibacterial efficiency is determined by the competition between the recombination (occurring in nanoseconds scale) of the photo-excited charge carriers, electrons and holes, and the transfer of those to the bacteria. Photodecomposition is not the only photochemical effect due to fact that TiO₂ is activated also by solar UV light. Under ultraviolet irradiation, titanium dioxide develops super-hydrophilic features.

This feature allows to increase the contact angle and to form a uniform protective water film on the surfaces treated with TiO₂²⁵. While under visible irradiation, TiO₂ becomes hydrophobic with a contact angle of about 60-70 degree. Recently new classes of biocides based on doped titanium oxide nanoparticles were proposed in the field of Cultural Heritage²⁷.

Ag and Fe ions are reported to be used as electron acceptor to decrease the e⁻– h⁺ recombination⁴⁷. The modification of TiO₂ using metal ions to improve the electron mobility of

TiO₂ that exhibits high reactivity under visible light ($\lambda > 400$ nm) allowing to use a larger range of the solar spectrum, even under poor UV lighting. Fe³⁺ is defined⁴⁷ to be the best anti-bacteriological candidate due to its band-gap (~2.6 eV) and similar size to that of Ti⁴⁺ and Fe³⁺-doped nanostructured TiO₂ has showed an antibacterial behavior. Fe³⁺ cations may insert into the TiO₂ structure and locate at interstices or occupy lattice positions.

Moreover, there are several applications of Ag-TiO₂ for photo catalyst, antibacterial and optical surface treatments⁴⁸. Silver can: 1) trap the excited electrons from titanium dioxide and vacate the holes for the degradation reaction of organic species; 2) extend TiO₂ wavelength response towards the visible region⁴⁹. In addition, silver ions are known to cause denaturation of proteins present in bacterial cell walls and slow down the bacterial growth⁵⁰.

Recently, alkaline-earth metal ions have been considered a promising, efficient and economic approach for doping the TiO₂⁵¹. There are many reports on transition metal, rare earth and noble metal ion doping of TiO₂, but studies on alkaline-earth metal ion doping of TiO₂ and their photocatalytic properties have seldom been reported. Some authors report good results obtained by using strontium ions to switch the absorption of TiO₂ to a longer wavelength^{52,53}. Indeed, doping TiO₂ with Sr results in lower Photoluminescence intensity in the range 325-575 nm which, in turn, leads to an higher separation efficiency. As a consequence, Sr-doped TiO₂ shows an enhanced photocatalytic activity. Based on these considerations, doped TiO₂ can be more effective in the protection and maintenance of stone surfaces with respect to pure TiO₂, reducing thus the bio deterioration processes.

However, as stressed by Nugari and Salvadori⁵⁴ before any application on monument surfaces, the products must be tested not only for their biocide efficacy but also for being harmless to cultural heritage material. The protective layer of an artifact must be at the same time biocide, hydrophobic, transparent, easily removable and constituted by materials, which do not damage the artifacts.

2.2.2 Antibacterial materials and nanoscience

Attack and growth of microorganism on the surfaces can cause its degradation. The most used antimicrobial agents are chemical reagents or exposure to UV radiation. However, the effect

of chemicals reagent is not lasting long, while the UV radiation is cured while irradiating. Therefore, photo catalysis is an alternative antimicrobial efficacy as illustrated in Ref.⁵⁵.

In general, the inorganic antibacterial materials consist of two categories: those, such as silver, that make contact with bacteria to inhibit their proliferation, and those, as hydroxyl free radical or active oxygen, that produce secondary bactericidal agents⁵⁶, under visible light, in order to kill the bacteria instead of making contact with them. The bactericidal potencies depend on the cellular structure of the tested bacteria and on the semi conductive nature of the nanomaterials⁴⁸.

In details, the studied semiconductors are:

- Titanium dioxide
- Zinc oxide
- Tin oxide
- Graphene - based materials

Concerning the first semiconductor, as the titanium dioxide is exposed to UV light irradiation, holes (h^+) and excited electron (e^-) are generated. The antibacterial properties of TiO_2 are conferred to the redox reaction of the surface species, offering oxidation of bacteria (the holes are trapped by water or hydroxyl groups adsorbed on the surface to generate hydroxyl radicals, which are powerful and oxidizing agents for degrading a wide range of materials⁵⁷). The antibacterial efficiency is determined by the recombination of the charge carriers and the transfer of those carriers to the bacteria⁴⁷.

Concerning the other nanomaterials cited above, even though the antibacterial mechanism is not fully known yet, the possibilities of a cells membrane disruption caused by direct interaction between nanomaterial and bacteria have been reported in literature^{58,59}.

The choice to employ nanomaterials as antibacterial agents through the growth of the films is due to the several advantages that this combination displays. The combined use of nanomaterials with protective layer (usually realized with silicon, sol gel or resins) allows not only to have a good application of the nanomaterial on the surface to be protected against bacteria but also to safeguard the same surface from other attacks due to the environmental conditions. In fact, the protective film plays an important role on the conservation, in aspects ranging from mechanical damage, physical, chemical and microbiological activities.

Antibacterial activity of Fe³⁺ doped TiO₂ thin film against Escherichia Coli

Fe³⁺ ions favor the film's photocatalytic reaction through the formation of hydroxyl free radicals. In fact Fe³⁺ combined with TiO₂ exhibits excellent antibacterial effect.

Characterization of the thin film

The Fe³⁺ doped TiO₂ film is porous because of the expelling of organic compounds. The porous structure (Figure 13) increases the surface area of the catalyst, thus enhancing the antibacterial efficiency⁴⁷. Absorption spectra (Figure 14) show that the primary luminous energy, which causes the transition of electron during the photocatalytic process, is very high in the UV region⁴⁷.

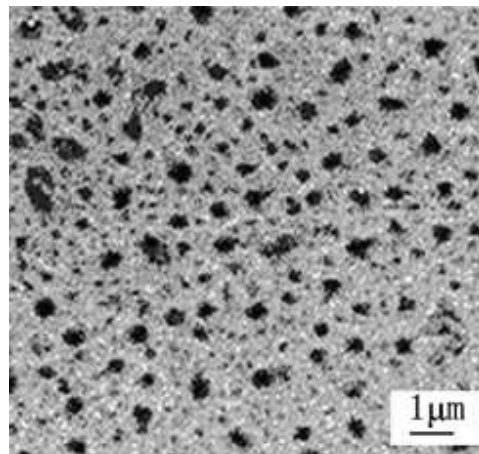


Figure 13 - SEM image of Fe³⁺ doped TiO₂ film

The absorption of the Fe³⁺ doped TiO₂ film has a red shift with respect to that of the pure TiO₂ film (Figure 14) caused by the fact that the iron ion replaces the Ti⁴⁺ in the TiO₂ crystal lattice. The replacement of Ti⁴⁺ with Fe³⁺ is simplified by the fact that both ions species have similar radius⁷. The antibacterial activity is enhanced in presence of both TiO₂ and fluorescent light (Figure 15)⁴⁷.

As can be seen of the Figure 16, the antibacterial efficiency of a Fe³⁺ doped film, after a first phase of improvement with increasing iron ion content, decreases for a higher ion concentration. The

optimum concentration is 0.5 % (mol) with an efficiency of 95% reached after 120 minutes of irradiation. The SEM images of E. Coli show that after 120 minutes the number of germs is much less than the one before irradiation (Figure 17b). After 240 minutes of irradiation there are no bacteria on the substrate (Figure 17c)⁴⁷.

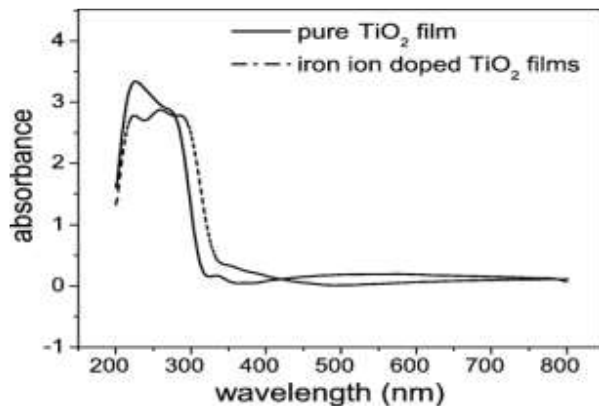


Figure 14 - UV-Vis absorption spectrum

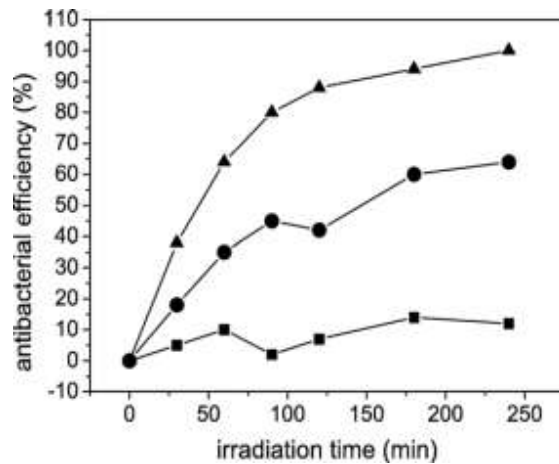


Figure 15 - Antibacterial efficiency as a function of time for (▲) TiO₂ film irradiated with fluorescent light and control experiments: (◻)TiO₂ thin film only; (●) fluorescent light irradiation only

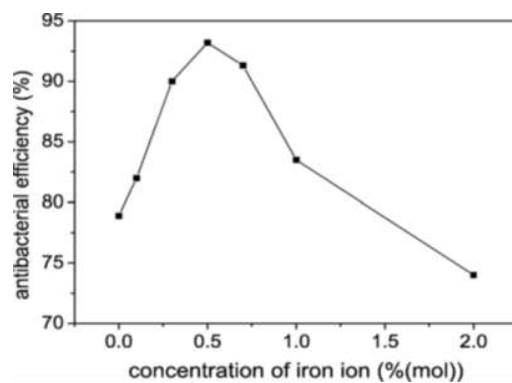


Figure 16 - Antibacterial efficiency as a function of the concentration of Fe³⁺ dopant (mol) after 120 min irradiation

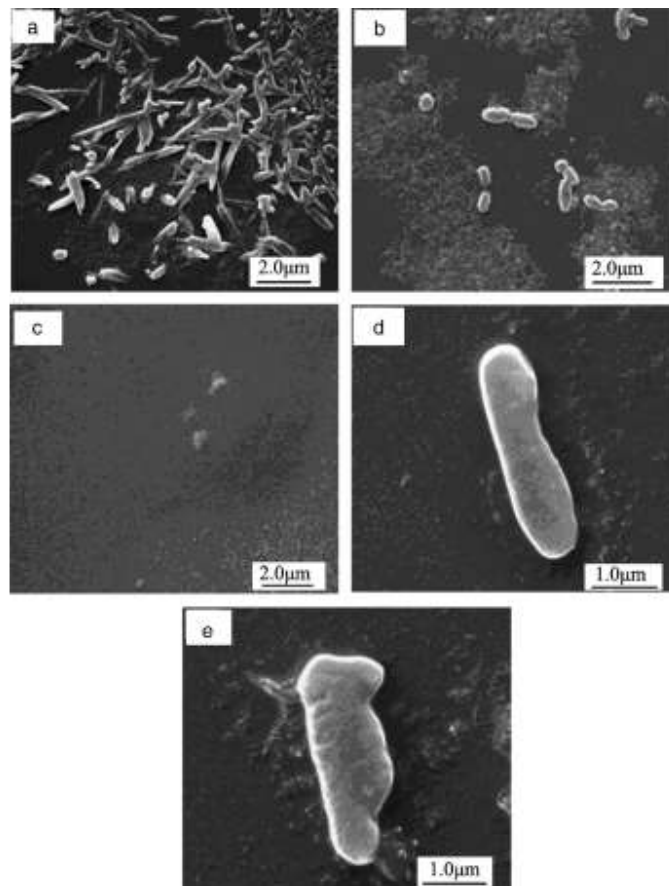


Figure 17 - SEM images of bacteria on the Fe^{3+} doped TiO_2 film surfaces: a) irradiated 0 min; b) irradiated for 120 min; c) irradiated for 240 min; d) single bacteria irradiated for 0 min and e) single bacteria irradiated for 120 min

From this information, we can see that iron ion present excellent antibacterial properties and the optimum concentration is about 0.5% (mol). In detail, comparing the bacterium before and after 120 minutes of fluorescent light irradiation (as you can see in the Figures 17 d and e respectively) we can observe that the bacterium loses its regular shape showing the formation of swellings on its cell wall

*Antibacterial activity of Fe^{3+} doped $\text{TiO}_2/3\text{SnO}_2$ NPs against *Escherichia Coli**

SnO_2 is among the best photo catalytic material due to its high absorption in the UV region⁶⁰. Doping with metal or metal oxide shows improvements in the photo catalytic activity⁶¹.

Characterization of the doped SnO₂

As well known^{51,62} the anatase is a better phase of TiO₂ compared to rutile. The crystalline size of Fe³⁺ with doping in the range of 0.3 – 1.2 % (mol) and after calcination at 400°C for 2 h, exhibits nearly the same crystalline size as the anatase phase (Table 2)⁵¹.

Table 2: Crystalline size and phases of TiO₂/3SnO₂/Fe³⁺ powders synthesized with various Fe³⁺ quantities after calcination at 400°C for 2 h.

<i>Fe³⁺ content (mol %)</i>	<i>Crystallite size (nm)</i>		<i>Phase content (%)</i>	
	Anatase	Rutile	Anatase	Rutile
0.3	18.46	-	100	0
0.5	16.53	-	100	0
0.8	20.59	-	100	0
1.0	16.52	-	100	0
1.2	18.44	-	100	0

The photocatalytic activity of Fe³⁺ doping (evaluated by degradation of Methylene Blue Dye - MB) indicates that in some concentration Fe³⁺ has a better efficiency than those of pure TiO₂/SnO₂⁵¹. The number of viable colonies of E. Coli when added TiO₂/3SnO₂/0.5 Fe³⁺ and exposed to UV and visible light decreased with increasing time (see Figure 18).

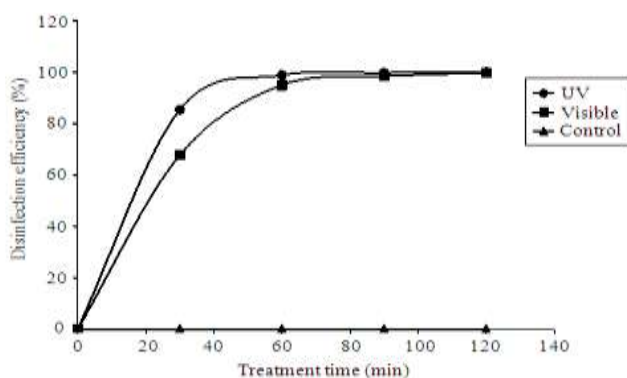


Figure 18 - TiO₂/3SnO₂/0.5Fe³⁺ photo catalysis against *E. Coli*

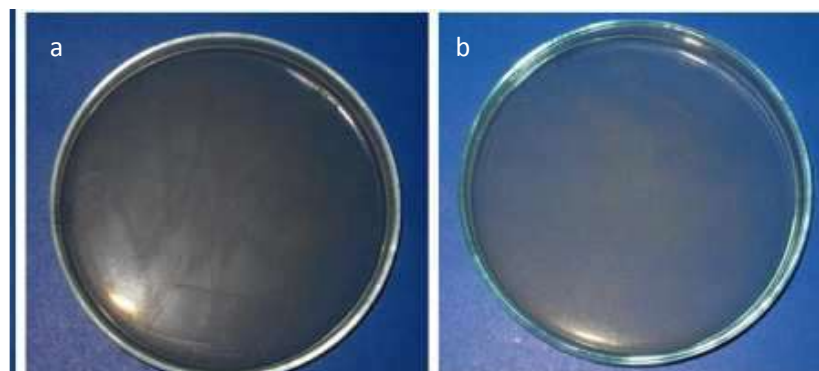


Figure 19 - Growth of *E. coli* on Nutrient Agar (NA) plate with the presence of $\text{TiO}_2/3\text{SnO}_2/0.5\text{Fe}^{3+}$ under UV irradiation or visible light and control (a) after visible light irradiation for 90 min and (b) after UV irradiation for 90 min

The bacteria *E. Coli* with the presence of $\text{TiO}_2/3\text{SnO}_2/\text{Fe}^{3+}$ was completely inactivated within 90 min under UV irradiation, as shown in Figure 19a, and the degradation reaches 99.7% when exposed to visible light for 90 minutes, as shown Figure 19b⁵¹. In conclusion, Fe^{3+} doping acts as obstacle for anatase crystal growth, therefore the crystalline size of the $\text{TiO}_2/3\text{SnO}_2/\text{Fe}^{3+}$ nanoparticles (16-20 nm) are smaller than those of pure TiO_2 (33nm) and un-doped $\text{TiO}_2/3\text{SnO}_2$ (25nm)⁵¹ and this leads to an enhancement of the photocatalytic activity due to larger specific surface area of the $\text{TiO}_2/3\text{SnO}_2/\text{Fe}^{3+}$ nanoparticles. These nanoparticles have demonstrated strong antimicrobial properties through a mechanism including the production of reactive oxygen species that damages cell components and viruses⁵¹.

*Antibacterial activity of Boron doped TiO_2 against *E. Coli**

Boric acid is a typical microbicide. However, due to its low melting (185°C) and boiling (300°C) points it cannot be applied in a high temperature environment. As known,⁶³ the boron atoms are often replaced by oxygen atoms or incorporated into the TiO_2 lattice. Therefore, boron-doped TiO_2 can improve the photocatalytic efficiency⁵².

Characterization of Boron doped TiO_2

XRD patterns demonstrate that the phase transformation of anatase to rutile occurs at 700°C⁵². The proportion of the rutile phase becomes larger as the calcination temperature

increases. Calcinated at 900°C, the anatase phase disappears and the rutile phases becomes predominant. The crystalline and the crystal phase are crucial factors in the antibacterial activity of TiO₂, where the crystalline anatase phase is considered to be the most active form of TiO₂, while rutile and amorphous TiO₂ are believed to be relatively inactive^{51,52}. Table 3 shows how boron doped TiO₂ inhibits the grain growth, since boron ions may enter the interstitial site of the TiO₂ anatase crystal structure and therefore lead to the growth of a unit cell volume⁵²

Table 3: Effect of calcination temperature on lattice parameters of B/TiO₂.

<i>Catalysts</i>	<i>Crystallite diameter (nm)</i>	<i>Unit-cell parameter (101)</i>		
		a (b) (nm)	c (nm)	V (nm ³)
<i>TiO₂-500 °C</i>	70	3.7820	9.5076	135.992
<i>B/TiO₂-500 °C</i>	40	3.7801	9.2531	132.219
<i>B/TiO₂-600 °C</i>	18	3.7821	9.3874	134.280
<i>B/TiO₂-700 °C</i>	48	3.7803	9.7237	138.958
<i>B/TiO₂-800 °C</i>	73	3.7897	9.5298	136.865
<i>B/TiO₂-900 °C</i>	-	-	-	-

TEM analysis demonstrates that the grains of TiO₂ are of a round shape, and after doping the particle with boron, their sizes become smaller and they have a better dispersion. This shows that doping with boron ions prevents the agglomeration of the particles in the heat treatment process; thereby increases the specific surface area of the antibacterial materials (see Figure 20)⁵².

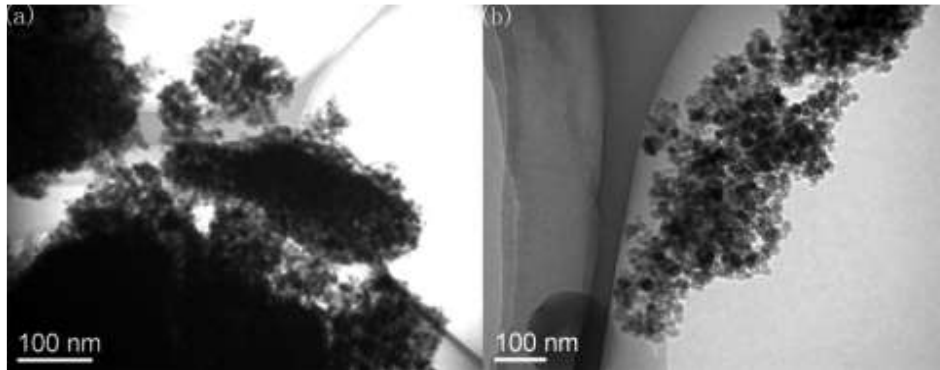


Figure 20 - TEM images of TiO₂ (a) and B/TiO₂ (b)

The performed XPS measurements show:

B1s peak that consist of three peaks

- 193 eV B-O-B bonds in B₂O₃
- 192 eV Ti-O-B (related to boron probably penetrating into the interstitial TiO₂ structure)
- 191 eV O-Ti-B (boron incorporates into the TiO₂ lattice through occupying O sites)

O1s peak that consist of three peaks

- 532 eV B-O-B
- 531 eV corresponds to oxygen into TiO₂ crystal lattice.
- 529 eV B-O-B

The oxygen O1s confirms that boron atoms incorporate into the TiO₂ matrix.

TiO₂ exhibits two lines

- 459 eV Ti(IV)2p_{3/2}
- 464 eV Ti (IV) 2p_{1/2}

A blue shift is observed in the Ti (IV) lines with the increasing of the calcination temperature. This suggests that oxygen atoms in the lattice of TiO₂ may be partially substituted by boron atoms⁵². FT-IR measurements show the presence of two lines at 3400 and 1650 cm⁻¹ corresponding to the surface adsorbed water and hydroxyl groups. This indicates the presence of free hydroxyl groups of all the materials⁵². The production of the some free groups (OH⁻ and O²⁻) on the material surface causes the destruction of the bacteria membrane and the change of its morphology⁵².

UV-Vis diffused reflectance spectra of Boron doped antibacterial materials calcinated at 500-900°C compared to TiO₂ at 500°C demonstrate that the absorption edge positions of all boron-doped materials extend into the visible region⁵². Consequently, this absorption suggests that the photo catalyst antibacterial can be activated by visible light⁵².

Moreover, the band gap decreases (rutile phase) with increasing temperature, as observed when comparing the absorption of boron-doped materials at low temperatures with those at high temperature. Boron doped TiO₂ nanoparticles can destroy or inhibit the growth of E. Coli. The Boron atoms can be weaved into the interstitial TiO₂ structure or incorporated into the TiO₂ lattice by occupying O sites (this is a metastable configuration which evolves into a new structure where the Boron ion is displaced from the O lattice position, occupying an interstitial site and inducing absorption in the visible region). In the contrary, the B³⁺ electron deficient character hydroxyl ions (OH) increase. In this case hydroxyl ions can capture electron hole pairs and transform them into free groups (OH⁻), causing the rapture of the cell membrane⁵².

Antibacterial activity of Nano crystalline Zinc Oxide by doping Mg(II) and Sb(III) against Escherichia coli, Staphylococcus aureus, Saccharomyces and Aspergillus niger

Generally, antimicrobials can be classified into three categories: organic, inorganic and polymeric. The organic and polymeric antimicrobials are rarely used due to their low fire resistant properties⁴⁸. In comparison, nano size inorganic antimicrobials are photocatalytic materials, such as ZnO. These materials are capable of producing hydroxyl radicals (OH) under light irradiation, and the resultant radicals can kill or inhibit the proliferation of microbes⁴⁸. ZnO is a semiconductor with a wide band gap (3.3eV) and n-type conductivity: these characteristics make this material attractive for many applications among those photo catalysis and antibacterial coatings⁶⁴.

Characterization of Nano crystalline Zinc Oxide by doping Mg(II) and Sb(III)

As can be seen in the Table 4, the non-doped ZnO powder shows considerable inhibition potencies on *E. Coli* and *S. Aereus*⁴⁸. Moreover, under the same incubational conditions, the antibacterial potencies of Sb doped ZnO crystal are greater than those of Mg doped ZnO. In particular the doping of Sb (III) in ZnO leads to more lattice defects in ZnO than those caused by Mg(II), which

increase the photocatalytic activity of Sb doped ZnO⁴⁸. In the case of fungi, the bacteriostatic effects are lower, which implies that the physiological characteristics are different for bacteria and fungi. The bactericidal effect of the powder on yeast is better than that on mold, because the cell wall of mold is thicker; hence the effect of ZnO nano powder against it is limited.

Table 4: Bactericidal Potencies of Different Nano-ZnO Powders

<i>Nanocrystal</i>	Doping ratio	<i>Bactericidal potencies (%)</i>			
		<i>Escherichia coli</i>	<i>Staphylococcus aureus</i>	<i>Saccharomyces</i>	<i>Aspergillus niger</i>
<i>ZnO</i>		65.4	70.2	36.2	8.2
<i>Sb-doped ZnO</i>	1:45	75.3	78.1	53.3	16.3
	1:15	91.5	94.8	61.6	18.4
	1:10	93.4	95.9	65.4	18.2
	1:5	83.5	88.2	55.5	12.9
<i>Mg-doped ZnO</i>	1:45	70.1	77.3	47.3	11.5
	1:15	81.6	90.1	49.1	13.5
	1:10	84.7	91.4	52.9	14.2
	1:5	74.4	84.6	46.4	10.8

Visible light irradiation tests show that the lighting in incubation considerably improves the bactericidal potencies of un-doped and doped materials⁴⁸, as such, light plays an important role in the antibacterial behavior of the tested nanomaterials. Such antibacterial behaviors are due to the radical produced by the reaction between nanoparticles and water molecules under visible light irradiation⁴⁸. A free radical is a highly active bactericidal agent that can oxidize a variety of organic materials. Zone inhibition tests show that ZnO, unlike some antibacterial agents that kill microorganisms by ion dissolution, has a similar effect as the photo catalysis. In Figure 21 one can see that the size of the halon depends on the amount of free radicals produced by ZnO nanomaterials⁴⁸.

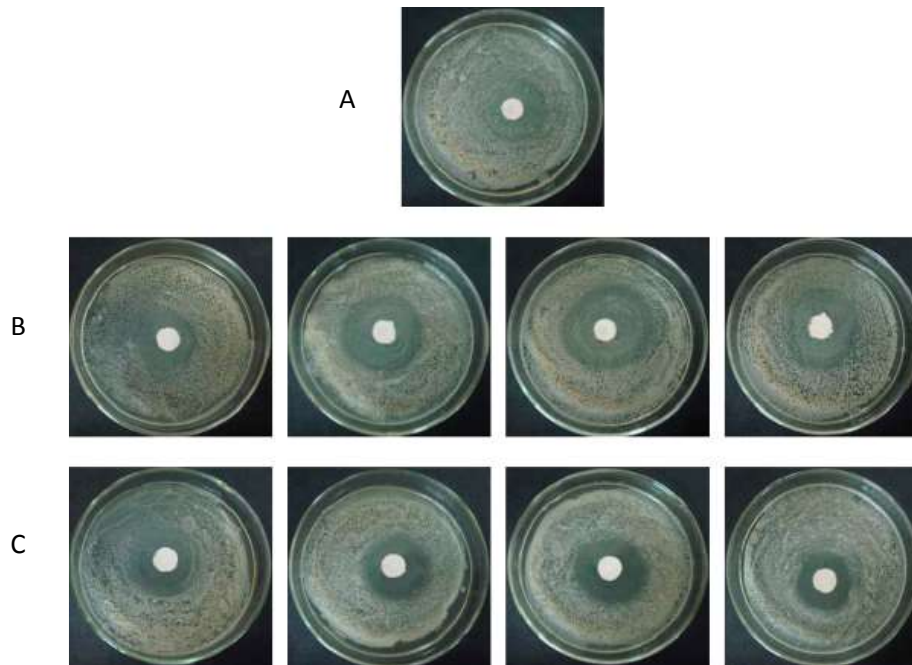


Figure 21 - Zone of inhibition test of nano ZnO crystals doped with Mg (B) and Sb (C) at different concentrations on Escherichia coli. The upper one (A) shows the inhibiting zone of a non-doped ZnO nanocrystal

The XRD patterns demonstrate (as can be seen in Figure 22) that with the higher doping level (higher than 1/10 mole ratio) the crystal lattice of the zinc oxide underwent a significant change. The XRD patterns of the doping ratio at 1:5 for Mg-doped and Sb-doped ZnO crystals and 1:10 for Sb-doped ZnO indicate the formation of a new crystal phase (as evidenced in the circled zones in Figure 22).

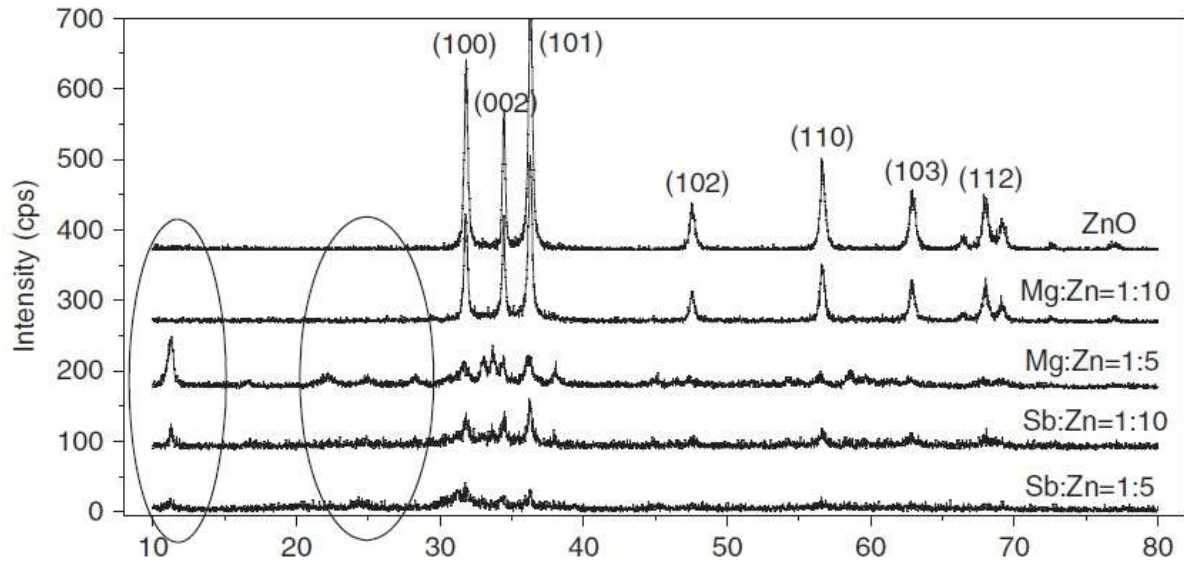


Figure 22 - XRD patterns of a ZnO nanoparticle doped with Sb^{3+} or Mg^{2+} under heavy doping

Figure 23 (an enlarged figure of partial patterns) shows that the new crystal phase caused by Sb doping is different from the new phase resulting from Mg doping in the crystal structure, which might be one of the major reasons that led to the difference in the bacteriostatic potency between Mg doped and Sb doped ZnO crystals. The Mg doping contributed to the appearance of five new XRD peaks at 17.0, 22.4, 25.5, 28.6, and 38.31 (2θ), while the Sb doping gives rise to three new peaks at 17.0, 24.6, and 38.31 (2θ)

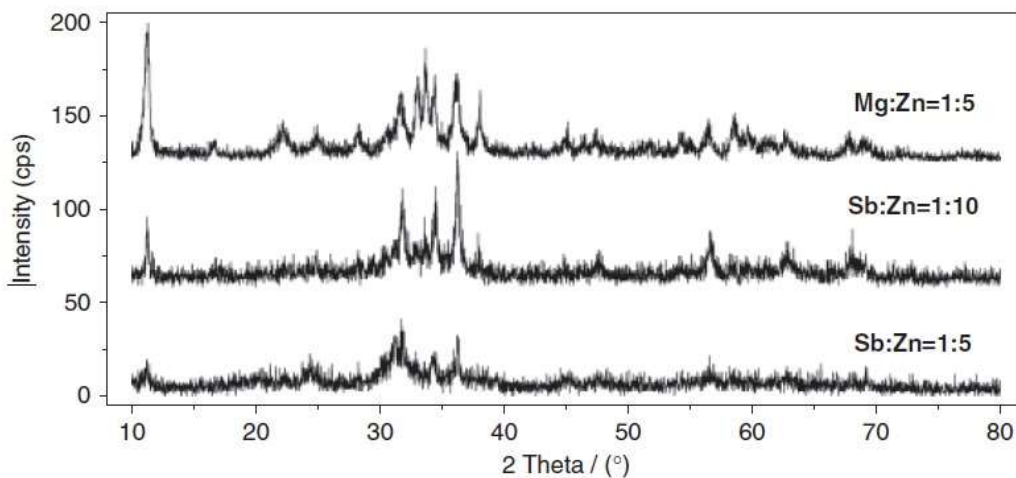


Figure 23 - XRD patterns of a ZnO nanoparticle doped with Sb^{3+} or Mg^{2+} under heavy doping

Based on the TEM pictures (see Figure 24), it is believed that the new crystalline phases were not independent crystal forms but some regional aberrations on the original ZnO crystal.

Figure 22 and 23 indicate that these peaks of new crystalline phases have low intensities while the main peaks still belong to ZnO, and the positions and the numbers of the peaks are varied between doping elements Mg and Sb and at different doping levels. All of this demonstrates that the new crystalline phases have no definite crystal lattice and form.

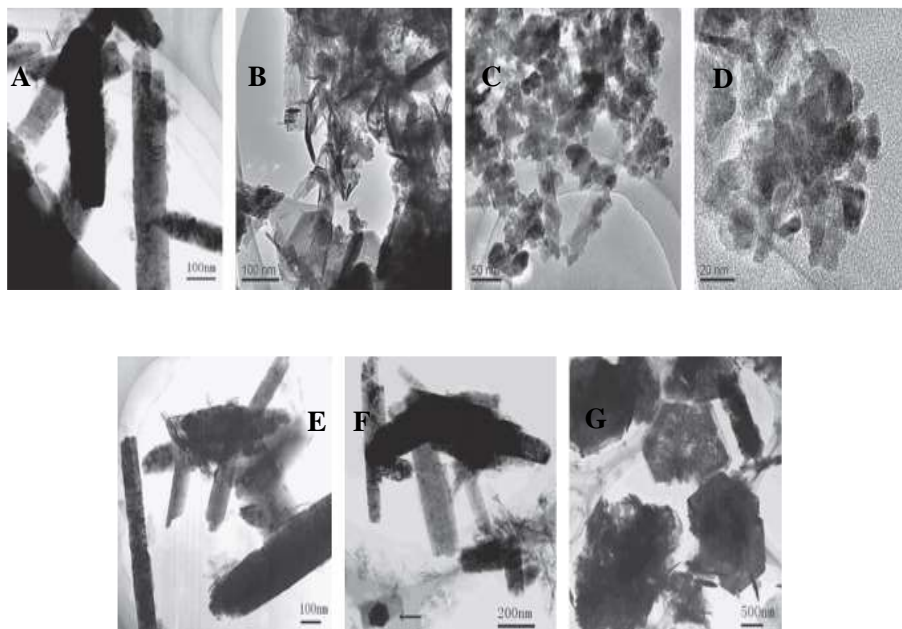


Figure 24 - TEM images of doped and non-doped zinc oxides. (A) is a pure ZnO, (B) Zn:Sb51:15, (C) Zn:Sb51:10, and (D) Zn:Sb51:5. The low group, (E) is a pure ZnO, (F) Mg:Zn51:10, and (G) Mg:Zn51:5.

TEM images (see Figure 24) show the variation induced by Mg and Sb doping. The images demonstrate that the crystals of non-doped ZnO are characterized by nano rods and larger size crystals (see subplot A and E), while the size of the Sb doped ZnO crystal decreases with increasing amount of doping (see subplot B-D) and the crystals present an high number of grained crystals. In the case of Mg-doped ZnO, instead, the size of the crystal does not change considerably⁴⁸, but the crystalline form varies from six-rowed rods to six-rowed lamellar. The lamellar crystal appears in a very small amount at a low doping level (see Figure 24E, indicted by arrow), and in a huge amount as the doping ratio reached 1:5 (see Figure 24F). Therefore, when the doping is heavy, the differences in the number of outer-shell electrons and in the ionic radius between the doping

element and the matrix element will be more distinct, contributing to the transformation of original six-rowed columnar crystals of zinc oxide into a new crystal phase.

The most important cause for the variation in the crystalline form is the different valence of the doping elements from the matrix element⁴⁸. When the element Mg (II) is doped into matrix element Zn (II), the distortion of the ZnO₂ lattice results from the difference in the ionic radius between the matrix and the doping elements⁴⁸. In the case of Sb(III) doped ZnO crystal, the cause for the variation of the crystal is relatively complex. Sb (III) within the crystal has one more oxygen atom around it than Zn (II), which, as Sb was doped into the Zn matrix, caused a hanging bond on Sb atom, or unbounding valence electrons.

These unbounding electrons within the crystal lattice facilitate the formation of an n-type semiconductor with a lower band gap energy⁴⁸. Consequently Sb doping promotes the semiconductor characteristic of ZnO crystal, conferring a more effective photo catalysis nature than Mg doped ZnO and leading to the variation of ZnO crystal more obvious than when doped with magnesium. In addition, the obvious difference in the ionic radius also aids the distortion of the crystal lattice. The analysis here suggested that the new phases found in the XRD patterns are just regional crystalline distortions caused by doping instead of a new crystalline form, as the distortion can lead to hanging bonds and unbounding electrons but a new crystal cannot.

The bacteria tests are performed on both types of bacteria: prokaryote and eukaryote. In details, *E.coli* and *S. aureus* are prokaryote, while *Saccharomyces* and *A. niger* are eukaryotes. The cellular properties of prokaryotes and eukaryotes are different⁴⁸. Although both *E. coli* and *S. aureus* are prokaryotes, *E. coli* is a Gram-negative organism and *S. aureus* is a Gram-positive organism, which suggests that there are differences between them in the cell wall⁴⁸. In particular antibacterial potencies of Sb doped ZnO are found to be 93.4% for *E. coli*, 95.9% for *S. aureus*, 65.4% for *Saccharomyces* and 18.2% *A. niger*; while those of non-doped ZnO are found to be 65.4%, 70.2%, 36.2%, 8.2%, respectively.

The antibacterial strength of Sb doped ZnO and Mg doped ZnO are stronger on a prokaryote than on a eukaryote⁴⁸. Therefore, the reduction of size of ZnO crystal confers enhanced photocatalytic activity to the crystal. Probably, the bacterial strength of the inorganic nanomaterial depends on the amount of OH free radical produced under irradiation. With a smaller size, the specific surface area of the nanosized metal oxides increase and therefore the photocatalytic activity of materials increases too. The doping contributes to reducing the grain size of the ZnO

crystal increasing its photocatalytic activity. Both Mg doped and Sb doped ZnO crystals show excellent bactericidal strength, especially on *E. coli* and *S. aureus*⁴⁸.

Antibacterial activity of ZnO and Co doped ZnO nanoparticles toward bacteria cells

Characterization of ZnO and Co doped ZnO nanoparticles

The XRD patterns of the pure ZnO and 5% -10% Co doped ZnO (see Figure 26) show how the Co doping in ZnO increase the crystalline size. This can be attributed to the less solubility of Co in the ZnO matrix⁵⁴. Since the doped Co concentration is far below the solubility limit of Co in ZnO matrix, this can effectively diminish the possibility of secondary impurity phases⁶⁵.

The increase of ZnO in the crystalline size indicates that the Co²⁺ ions have substituted the Zn²⁺ ions in the samples without changing its crystal structure. The increase in cell parameters may be due to the octahedral coordination of the Co²⁺ ions, which replace Zn²⁺ ions in the ZnO matrix. This means that Co doping has only a small effect on the lattice parameters of ZnO and this result is attributed due to a small mismatch in radius between Zn²⁺ and Co²⁺. The SEM images (see Figure 26) show how the size of un-doped ZnO crystal is slightly lesser than the Co-doped ZnO⁵⁴. In addition, the same images reveal that the crystallinity is in the order of nm without changes in the grain size⁵⁴.

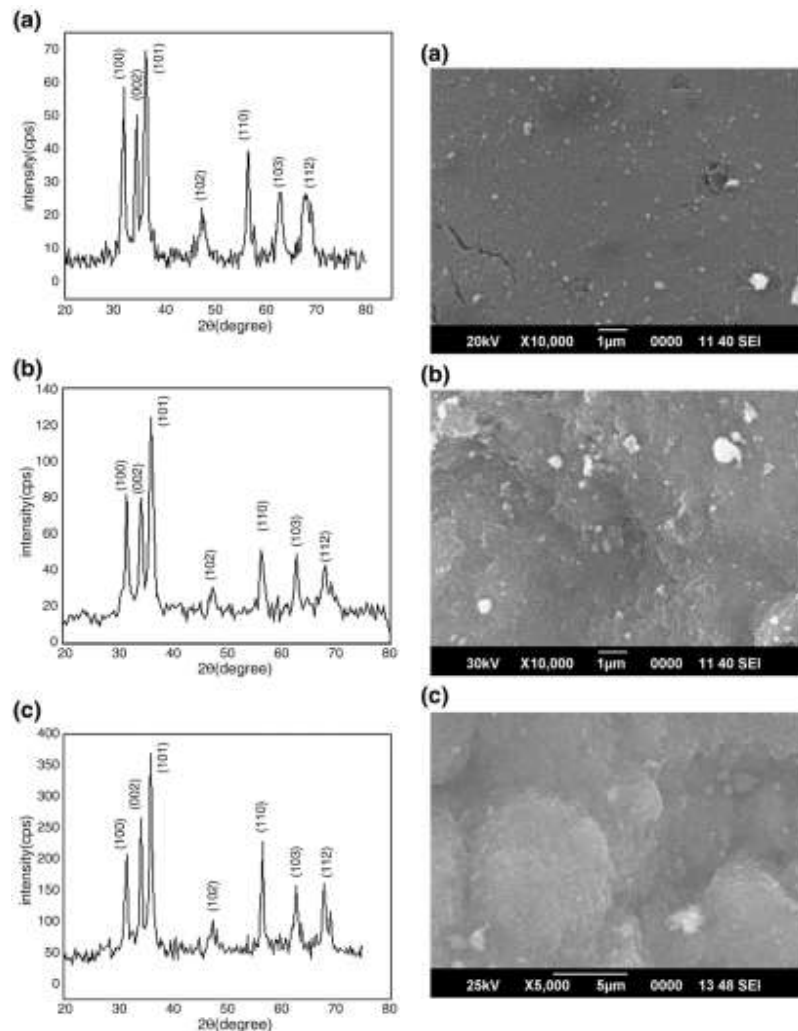


Figure 25 - XRD of a) ZnO;
b)Zn_{0.995}Co; c)ZnO_{0.9}Co

Figure 26 - SEM images of a)ZnO;
b)ZnO_{0.995}; c) ZnO_{0.9}CO

In the ZnO absorption spectra the shift toward shorter wavelengths grows with the increase of the concentration of doping Co⁵⁴. The shift indicates that the band gap of ZnO increases with the doping concentration of Co²⁺ ions. The increase in the band gap or blue shift can be explained with the Burstein–Moss effect. According to the latter, the Fermi level merges into the conduction band with the increase of a carrier concentration. The photo catalytic activity of ZnO and Co-doped ZnO are investigated using MB and reveal that un-doped ZnO decolorizes the MB faster than doped ZnO.

Photo catalytic activity of un-doped ZnO is attributed both to the donor states (which are caused by the large number of defect sites such as oxygen vacancies and interstitial zinc atom) and to the acceptor states (which arise from zinc vacancies and interstitial oxygen atoms). Lower photo-degradation of MB with UV and doped ZnO (ZnO:Co²⁺) may be attributed to the change in absorption characteristics caused by Co²⁺ doping⁵⁴. The antibacterial activity of pure and Co doped ZnO are investigated on different bacterial strain of *Escherichia coli*, *Klebsiella pneumoniae*, *Shigella dysenteriae*, *Salmonella typhi*, *Pseudomonas aeruginosa*, *Bacillus subtilis* and *Staphylococcus aureus*. Co doped ZnO exhibit remarkable antibacterial activity against all tested bacterial strains⁵⁴. Then the doping of Co enhances the antibacterial property of ZnO. These results suggest that ZnO with Co²⁺ nanoparticles can be used as immobilized photo catalysts for water and environmental detoxification from bacteria⁵⁴.

Antibacterial activity of silver modified graphene oxide (GO)

The antibacterial activity of GO has been attributed to membrane stress induced by sharp edges of graphene nano sheets, which may result in physical damages on cell membranes, leading to the loss of bacterial membrane integrity and the leakage of RNA⁶⁶.

The silver nanoparticles, through the release of silver ions, can inactivate the microorganism cells by increased membrane permeability, leakage of cellular content, disruption DNA replication and later death⁶⁷. The mechanisms behind the activity of silver and bacteria can be summarized in:

- 1) Uptake of free silver ions followed disruption of adenosine triphosphate (ATP) production and DNA replication;
- 2) Generation of Reactive Oxygen Species (ROS) (Ag⁺ can interact with thiol groups in proteins, resulting in inactivation of respiratory enzymes and leading to the production of ROS⁴⁹) between silver NPs and silver ions (if excess ROS production may produce oxidative stress⁶⁸);
- 3) Damage to cell membranes⁶⁹.

In Figure 27 hypothetical interaction between silver nanomaterials and bacteria cells are shown⁵⁸.

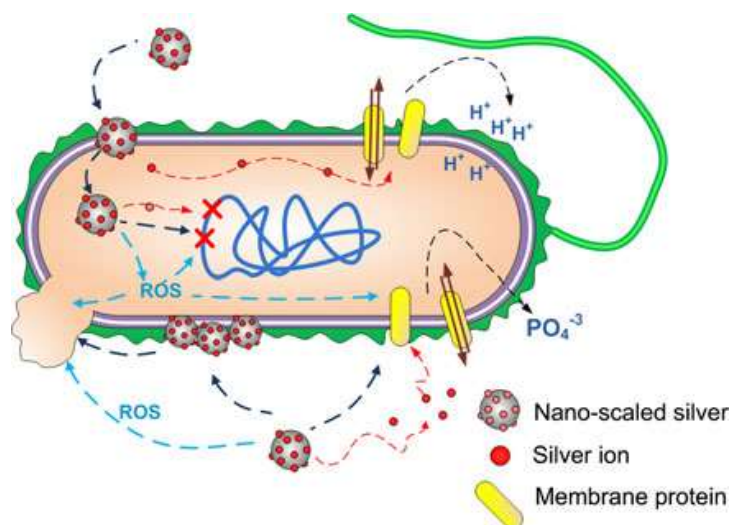


Figure 27 - Diagram summarizing silver interaction with bacteria cells

Characterization of silver modified graphene oxide (GO)

The Figure 28a shows the UV-Vis spectra of GO (which is prepared from natural graphite by using a modified Hummers method⁵⁶) and Ag-GO composite (which is obtained employing Ag NPs by using a glucose reduction method in the presence of ammonia at room temperature⁵⁶). In particular the UV-Vis spectrum of the Ag GO composite displays an absorption band at about 415 nm, which is the characteristic absorption band of Ag nanoparticle due to plasmon resonance⁵⁶. Figure 28b in addition to the peak of GO at 10.4°, shows the other peaks typical of the diffractions of metallic Ag suggesting the formation of metallic Ag nanoparticles⁵⁶.

63

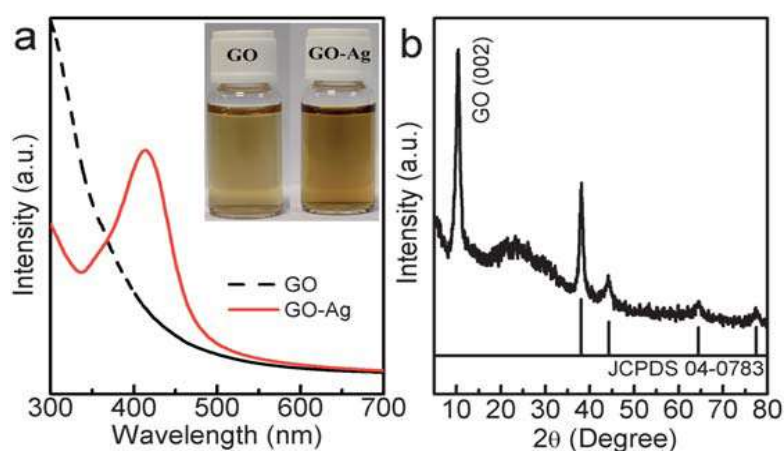


Figure 28 - UV-Vis absorption spectra

The performed XPS measurements indicate that the peaks of Ag 3d core level at 368.1 eV and at 374.1 eV are assigned to Ag 3d_{5/2} and Ag3d_{3/2} photoelectrons respectively⁵⁶. The splitting of the 3d doublet of Ag is 6.0 eV, indicating the formation of metallic silver⁵⁶. The antibacterial activity was evaluated by using *Escherichia Coli*: Gram negative.

As can be seen in the Figure 29, the composite Ag-GO exhibits a very high bactericidal activity; this composite is able to form colonies after 5 minutes of contact and without more cells viable after 10 minutes⁵⁶.

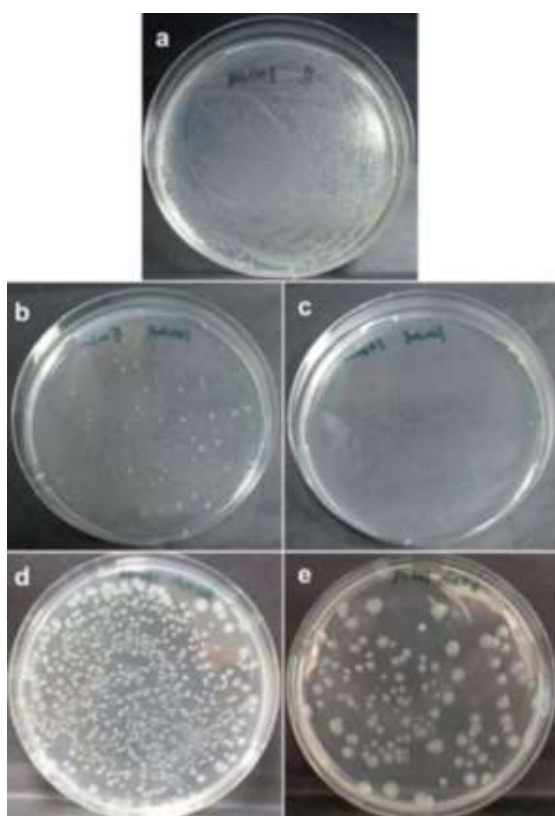


Figure 29 - Bacterial colonies formed by *E. coli* cells (a) in the absence of Ag-GO (control experiment) and bacterial colonies treated with Ag-GO for b) 5 min, (c) 10 min in a slurry system and (d) 30 min and (e) 60 min in a partition setup system

As we can see in the Figure 29, there are still plenty of bacteria cells survived also after treatment for 30 and 60 minutes. Finally Ag⁺ exhibits antibacterial properties at high concentration⁵⁶. The TEM images (see Figure 30) demonstrate that *E. Coli* is a bacterium with an elongated shape and intact surface (a), while after being in contact with Ag-GO for 30 minutes the

ends of the cells are destroyed (b)^{56,58}, indicating that the external and internal membranes are damaged.

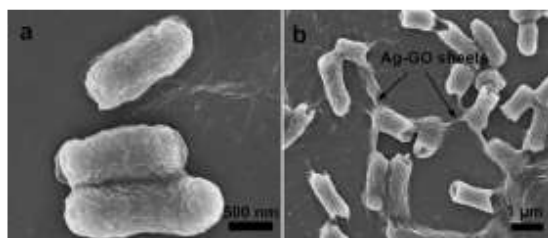


Figure 30 - FESEM images of *E. Coli* cells (a) without being treated (control) and (b) treated with Ag-GO for 30 min

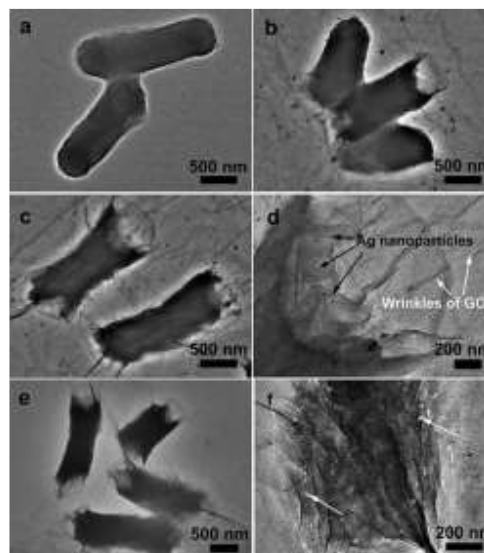


Figure 31 - TEM images of *E. Coli* cells after the control experiment (a) and treated with Ag-GO for (b) 5 min, (c and d) 20 min, and (e and f) 30 min

Antibacterial Activity of Graphite, Graphite Oxide, Graphene Oxide, and Reduced Graphene Oxide against E. Coli

In the following work is reported a comparison of antibacterial activity of four types of graphene-based materials against a bacterial model *E. Coli*.

Characterization of four types of graphene-based materials

E. Coli is incubated to evaluate antibacterial activity of four types of graphene-based materials. *E. Coli* cells are incubated with the same concentration (40 µg/mL) of Graphite (Gt), Graphite Oxide (GtO), Graphene Oxide (GO), and Reduced Graphene Oxide (rGO) dispersions in isotonic saline solution for 2 h, respectively⁵⁵. As one can clearly see in Figure 32a, GO and rGO exhibit a higher bacterial activity than Gr and GrO. Moreover, Figure 32b shows that the loss of *E. Coli* viability steadily increases with incubation time.

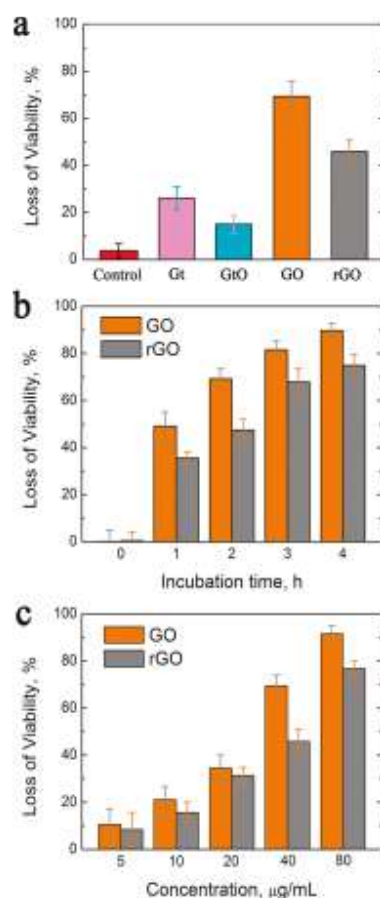


Figure 32 - a) Cell viability measurement after incubation with Gt, GtO, GO, and rGO dispersions; b) Time-dependent antibacterial activities of GO and rGO and c) Concentration dependent antibacterial activities of GO and rGO

For both materials, a large fraction of the cells dies in the first hour of incubation. Comparing GO and rGO dispersions, the first ones have much higher antibacterial activity than the second ones, for all tested incubation intervals⁵⁵.

Lastly, the loss of *E. Coli* viability progressively increases with GO and rGO concentration, as shown in Figure 32c. These results suggest that antibacterial activity of graphene-based materials is concentration dependent too.

SEM images showed in Figure 33, illustrate the interactions between graphene-based materials and *E. Coli* cells. The panels in Figure c-d and e-f show the different behavior of the GO and rGO, respectively.

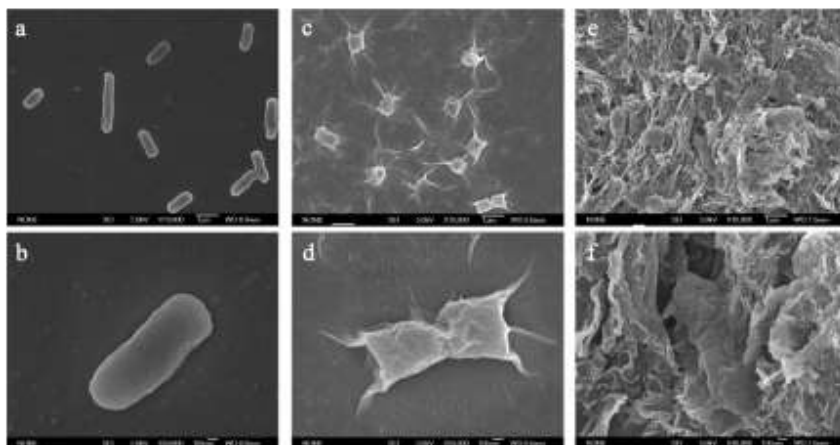


Figure 33 - SEM images of (a, b) *E. coli* after incubation with saline solution for 2 h without graphene-based materials, (c, d) *E. coli* cells after incubation with GO dispersion and *E. coli* cells after incubation with rGO dispersion

The panels c and d show that thin layers of GO Nano sheets are wrapped on *E. Coli* cells, while the panels e and f show that *E. Coli* cells are embedded in large rGO aggregates⁵⁵. The different behavior of GO and rGO observed in SEM images suggests that the aggregation/dispersion of graphene-based materials may play an important role in their antibacterial activity. Moreover, after exposure to GO or rGO dispersions⁵⁵, *E. Coli* cells become flattened and lose their cellular integrity: it is important to understand that this damage on the bacterial cells is irreversible⁵⁵.

The correlation among antibacterial activity, oxidative stress (GSH oxidation) and aggregate size are summarized in Table 5 below.

Table5 : Correlation among Antibacterial Activity, Oxidative Stress (GSH), and Particle Size

	<i>loss of cells (%)</i>	<i>loss of GSH (%)</i>	<i>particle size (μm)</i>
<i>GtO</i>	15.0 ± 3.7	21.4 ± 1.1	6.28 ± 2.50
<i>Gt</i>	26.1 ± 4.8	29.9 ± 0.7	6.87 ± 3.12
<i>rGO</i>	45.9 ± 4.8	94.2 ± 1.1	2.75 ± 1.18
<i>GO</i>	69.3 ± 6.6	22.2 ± 0.7	0.31 ± 0.20

Comparing GtO and GO, they have similar capacities in oxidizing GSH, but GO dispersion can kill much higher fractions of *E. Coli* than the GtO dispersion. GtO and GO contain almost the same chemical functional groups. Their difference is that GO is a single Nano sheets with average size of $0.31 \pm 0.20 \mu\text{m}$, while GtO are aggregated stacks of GO Nano sheets with average particle size of $6.28 \pm 2.50 \mu\text{m}$ ⁵⁵.

Their distinct antibacterial activities suggest that the aggregation of graphene Nano sheets is important in the antibacterial mechanism. Materials having smaller size (as GO) have higher cytotoxicity than those with larger size (GtO). However, the antibacterial activity of Gt ($26.1 \pm 4.8\%$) is much higher than that of GtO ($15.0 \pm 3.7\%$). This is correlated with their different GSH oxidation capacities. Metallic Gt can oxidize more GSH than insulating GtO, suggesting that the metallicity of graphene materials also plays a role in their antibacterial activity. Comparing GO with rGO, although rGO shows much stronger oxidation capacity toward GSH, smaller size GO has much higher antibacterial activity than rGO.

Results in Table 4 suggest that the antibacterial activities of graphene-based materials are attributed to their dispersibility, size, and oxidization capacity⁵⁵. In conclusion GO has the highest antibacterial activities, followed by rGO, Gt and GtO under the same dispersion concentration. Their antibacterial activities are time and concentration dependent. In general, graphene materials, which contain a higher density of functional groups, have smaller sizes and have more chances to interact with bacterial cells. By direct contact, graphene nano sheets can induce membrane stress by disrupting and damaging cell membranes, leading to cell death.

Antibacterial activity of Graphene based antibacterial paper

The antibacterial activity of this nanomaterial carbon based has been attributed to membrane stress induced by sharp edges of graphene nanosheets, which may result in physical damage to cell membranes, leading to the loss of bacterial membrane integrity and the leakage of RNA.

Characterization of Graphene

The TEM measurements demonstrate that GO nanosheets are inside the endosome of the cytoplasm (see Figure 34), suggesting that GO nanosheets itself could be internalized within cells⁷⁰.

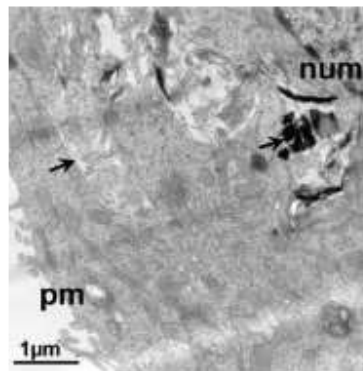


Figure 34 - Cellular uptake and cytotoxicity of GO nanosheets.
 (a) TEM images of A549 cell incubated with 85 g/mL GO nanosheets for 6 h. GO nanosheets were internalized in A549 cells

The antibacterial activity of GO nanosheets is evaluated by the interaction between *E. Coli* cells with GO nano sheets. The results of metabolic activity of *E. Coli* cells in presence of GO nanosheets suggests a strong inhibition ability of GO nanosheets to *E. Coli*⁵⁹.

The microbial viability of *E. Coli* is evaluated employing a classic colony counting method. The results show that GO almost completely suppressed the growth of *E. Coli*, leading to a viability loss up to 98.5%. TEM images reveal that *E. Coli* loses its cellular integrity, with the disruption of its cell membrane and the flowing out of the cytoplasm (see Figures 35 a and b)⁵⁹.

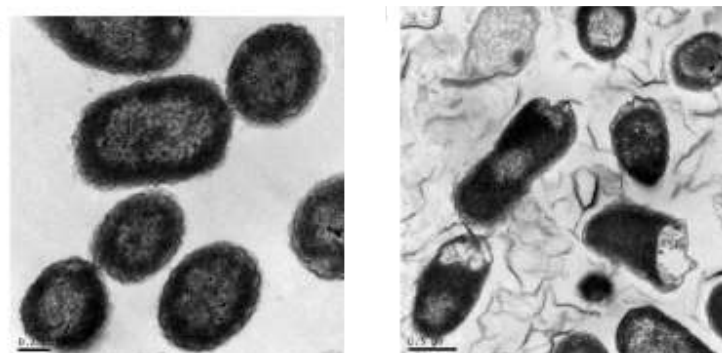


Figure 35 - a) TEM images of *E. Coli* (a) and *E. Coli* exposed to GO nanosheets at 37 °C for 2 h (b)

In conclusion, graphene-based nanomaterials have been found to be excellent antibacterial materials with low cytotoxicity. It has been demonstrated that macroscopic GO and rGO paper can be easily fabricated from their suspension via simple vacuum filtration. Due to the superior antibacterial effect of GO nanosheets and the fact that GO nanosheets can be mass-produced and easily processed to make freestanding and flexible paper with low cost, it is possible to expect that this new carbon nanomaterial will offer new opportunities for the development of antibacterial materials

3. Growth and Characterization of Nanomaterials and Nanostructured Materials for Conservation of Cultural Heritage

Artifacts are often exposed to humidity and to harsh environmental conditions (chemical and biological). This results in the formation of a corrosive patina on surfaces which irremediable damages to the artifacts (as in the case of the bronze where the formation of a bronze disease can damage the artifacts until its complete destruction). Usually, the restoration and conservation process consists in the removal of the corrosive patina (often by laser ablation process as indicated in Chapter 2), the consolidation with mortar (for stone and ceramic) and in the coating of a hydrophobic and bactericidal film. Therefore, the materials used for this purpose strongly modify the artifacts surfaces, covering decoration and pigments, and the process is often irreversible. In the following, we discuss the results obtained in the research of new innovative materials for surface protection.

3.1 Synthesis and Characterization of thin-transparent nanostructured films for surface protection

This thesis section demonstrates that very thin and optically transparent nanocomposite films can be conveniently applied on surface materials, displaying strong antibacterial properties without affecting the aesthetics of the underlying material. In our approach, we propose new composite materials, which ensure the surface protection by inactivating the bacteria before a biofilm can be formed. The films contain very small loadings of TiO₂, graphene, or fullerene, and can easily be applied on large surfaces using conventional brushes or air-brushes. These nanocomposite films are very promising candidates for the preservation of statues, mosaics, floors, buildings, and other objects that are exposed to challenging environmental conditions such as Architectonical Heritage or building materials (materials featuring stone, pigments, bronze, granite, marble, and glass).

3.1.1 Nanostructured protective films for CH surfaces: the idea

The use of embedded nano-materials has become popular in many fields such as medicine, biochemistry, nano-electronics, energetics, and material science, since they can improve the properties of macro-materials without provoking changes in the chemical composition. Strong interest has been devoted to the growth of nanostructured films with enhanced capabilities in optical transparency, super-hydrophobicity and bactericidal activity. These materials can form protective layers on surfaces, which can be useful for many applications: protection of artworks, realization of durable surfaces in civil engineering or in architecture, realization of new hydrophobic fabric to the coating of biological and medical devices, or in the food industry. Damages on material surfaces are, often, attributed to the metabolic activity connected with the growth of living organisms^{1,2,3,4,5,6}.

Therefore, one of the major challenges in surfaces conservation lies in the development of antibacterial protective coatings which do not alter the aesthetic, physical, or chemical properties of the underlying material^{7,8}. The problem of surfaces preservation becomes particularly challenging for materials exposed to harsh atmospheric conditions or located underwater. For these conditions, very typical in the architecture and building materials fields, the formation of microorganisms (microbes) in the biofilms has a strong negative impact^{9, 10, 11,12} since the microbes attack the material by producing nitric and sulfuric acids¹³. These acids destroy the surface or generate a green patina which completely covers the surface¹⁴. Furthermore, biofilms can deteriorate the material surface, leading in many cases to the complete destruction of decorations, colours, and pigments^{15,16}. By forming a biofilm on the surface, microorganisms provoke aesthetic and structural damage: they produce extracellular polymeric substances that cause swelling and contraction inside the pore system, which results in altered pore sizes and mechanical stress on its structure¹⁷.

The biological deterioration level, observed for different materials, depends on several factors, such as the chemical and mineralogical composition (i.e., mineral constituents, pH, relative percentage of various minerals, salinity, texture), environmental factors (temperature, humidity, light conditions, atmospheric pollution), and exposure time¹⁸. The biofilm formation process begins with the attachment of free-floating microorganisms onto a surface. These first colonists adhere to the surface initially through weak, reversible adhesion, such as van der Waals forces. If

the colonists are not immediately separated from the surface, they can anchor themselves more permanently using cell adhesion structures such as aspili. Hydrophobicity also plays an important role in determining the ability of bacteria to form biofilms, as biofilms with increased hydrophobicity have reduced repulsion between the extracellular matrix and the bacterium. Many different bacteria form biofilms, including gram-positive (e.g. *Bacillus spp*, *Listeria monocytogenes*, *Staphylococcus spp*, and lactic acid bacteria, including *Lactobacillus plantarum* and *Lactococcus lactis*) and gram-negative species (e.g. *Escherichia coli*, or *Pseudomonas aeruginosa*). Biofilms are also formed by bacteria that colonize plants, e.g. *Pseudomonas putida*, *Pseudomonas fluorescens*, and related *Pseudomonads* which are common plant-associated bacteria found on leaves, roots, and in the soil.

A large amount of work has been devoted to the surface protection of outdoor heritage assets¹⁹. In particular, since the preservation of objects of interest for Civil Architecture represents a major challenge in current research, has more stringent conditions than other surfaces, and has therefore attracted great attention by policy makers, industry and the scientific community. One of the most studied preservation methods is the application of hydrophobic coatings. However, these hydrophobic coatings, which are commonly composed of polymeric films, often alter the object aesthetics by changing brightness and coloration. For instance, Manoudis et al.²⁰ have evaluated super-hydrophobic composite protective layers composed of Syloxane and SiO₂ nanoparticles for three types of stones used for the restoration of the Prague Castle.

The authors only observed super-hydrophobicity when the stone is treated with high-loading dispersions (>0.5%). Unfortunately, the coloration and brightness of the three tested stones was highly affected by the protective layer, leading to a modification of the stone's appearance. Moreover, the protection of the film from microbial agents was not tested. Bactericidal properties of nanomaterial-based bactericidal agents, such as nanoparticles, nano-sheets, nano-tubes, and quantum dots, have already been examined for many other applications. While establishing the mechanisms behind their bactericidal activity remains a topic of active investigation, these bactericidal properties have most commonly been related to the nanomaterial causing a physical stress to the cell's membrane in addition to causing chemical changes, mostly as oxidative stress^{21, 22, 23, 24, 25}.

In this paper we propose a new composite materials based on bactericidal nanomaterials, acting as protection for surfaces, which can very efficiently protect a variety of materials of current

interest for Civil Engineering, Architecture, and Cultural Heritage in general, from exposure to the most common bacteria. The resulting coatings are very thin and can be easily deposited on large surfaces (statues, mosaics, walls, and floors). Furthermore, they do not affect the aesthetics of the underlying material.

3.1.2 Preparation and Characterization of Protective Films

The protective films are realized with a process of mixing and sonication of two different solutions containing the hydrophobic and nanomaterial components, respectively, followed by a high-temperature heating phase on a hot plate in air for favouring matrix polymerization. Different amounts of the obtained solutions are then deposited on the material's surface by a drop cast method to perform the laboratory tests. The spray-dry deposition is performed with a precision airbrush or using a conventional paintbrush, in order to test the deposition of the protective film on large areas. The effectiveness of the protective films is tested on five materials of interest for engineering and architecture: glass, granite, bronze, marble, and ceramic.

Nanomaterials (TiO₂ P₂₅ nanoparticles, fullerenes C₆₀, and graphene flakes) are purchased from Plasma Chem, GmbH and are dispersed as follows: TiO₂ (1 mg/mL) and graphene (1 mg/mL) are dispersed in distilled water and sonicated (Branson 2510) for 30 minutes and 4 hours, respectively, in order to obtain fine colloids with well separated TiO₂ nanoparticles and graphene flakes. Fullerene (1 mg/mL) is dispersed in dichlorobenzene and sonicated for 30 minutes. The bactericidal action mechanism of selected materials is well known for NMs colloidal solution and investigated in many literature works^{26,27,28,29}.

Titania nanoparticles and fullerene's aggregates have smaller dimensions than those of cell membranes, therefore they attack directly the external cell membrane, causing a disruption of the membrane itself, preventing exchanges between the bacterium and the external environments and causing the death of the cell³⁰. Moreover, TiO₂ nanoparticles penetrate into the membrane interacting between the proteins and the cell DNA as indicated in³¹. Graphene flakes have dimensions similar to those of bacterium (in the order of 1 micron) and have a planar structure. This generates the following interaction mechanism: first an initial cell deposition or adhesion on the graphene sheet, then a stress in the external cell membrane caused by the direct interaction between sharp micro-flakes, causing looser contacts between the bacterium and the nutritive

buffer^{32,33, 34}. Moreover, all the investigated nanomaterials cause an oxidative stress³⁵ caused by reactive oxygen species generated during the interaction between nanomaterials and bacterium or by the disruption of some specific microbial process and the oxidation of vital cellular structures (see in Figure 5 a sketch of main bactericidal effects of investigated nanomaterials).

Five materials commonly used in statues, mosaics, and historical buildings are tested: (i) “pink-granite” (granite with high concentration of k-pheldespar); (ii) Carrara white-marble; (iii) Greek-roman bronze (an historical alloy constituted by 90 % copper, 10 % tin, and lead impurities); (iv) ceramic with composition typical of Greek-roman artworks (aluminium-silicates with inclusions of quartz, feldspar, calcium carbonate, and iron oxides); and (v) a silicon dioxide based glass. All these materials are obtained from the consumer market and have dimensions of 3 cm × 3 cm. Sylgard 184 is purchased from Sigma-Aldrich in a Silicone Elastomer Kit, which is comprised of Base/Curing Agent to be mixed in a 10 (base) :1 (curing agent) ratio by weight for manual mixing.

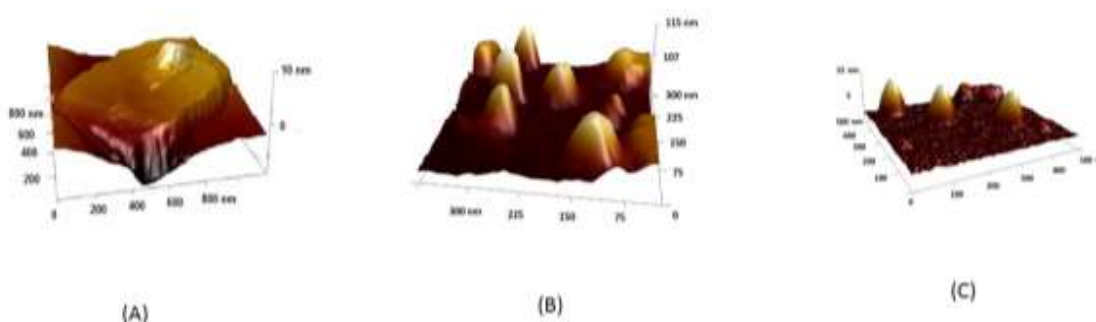


Figure 1 - AFM images of nanomaterials used for Film preparation

Synthesis and deposition on surfaces

3 g of Sylgard 184 (containing 10 wt% of curing agent for catalyzing the polymerization reaction) are dissolved in 30 mL acetone by sonication for 30 min.³⁶ Sylgard 184 is chosen for its well-known properties of hydrophobicity and transparency³⁷. An appropriate volume of the nanomaterial dispersions (1 mg/mL) is then added to the Sylgard 184 solution (100 mg/mL) so that the final weight percentage of the nanomaterial relative to Sylgard 184 is 0.1 wt%, 0.5 wt%, or 1 wt%. The mixture is sonicated for 30 minutes in air at room temperature. For the sample containing both TiO₂ and graphene flakes (ratio 1:1), an equal volume of the mixtures above containing the individual nanomaterials alone is combined and sonicated for 30 minutes. Different

amounts of the final solutions (from 0.1 to 3 mL; total volume) are deposited on the material's surface by drop casting, painting, or by spray-drying.

The area covered by the film is fixed using a metallic mask of 1 cm × 1 cm on the central region of each surface. Spray-drying is performed using precision airbrush (Genesis XG from GREX) or painted using a classic paintbrush (CWR, ART. K577/8). The deposited drops are then heated on a hot plate in air at 100 °C for 1 hour to induce polymerization. Polymerization on large surfaces is achieved by maintaining the system at room temperature for 48 h.

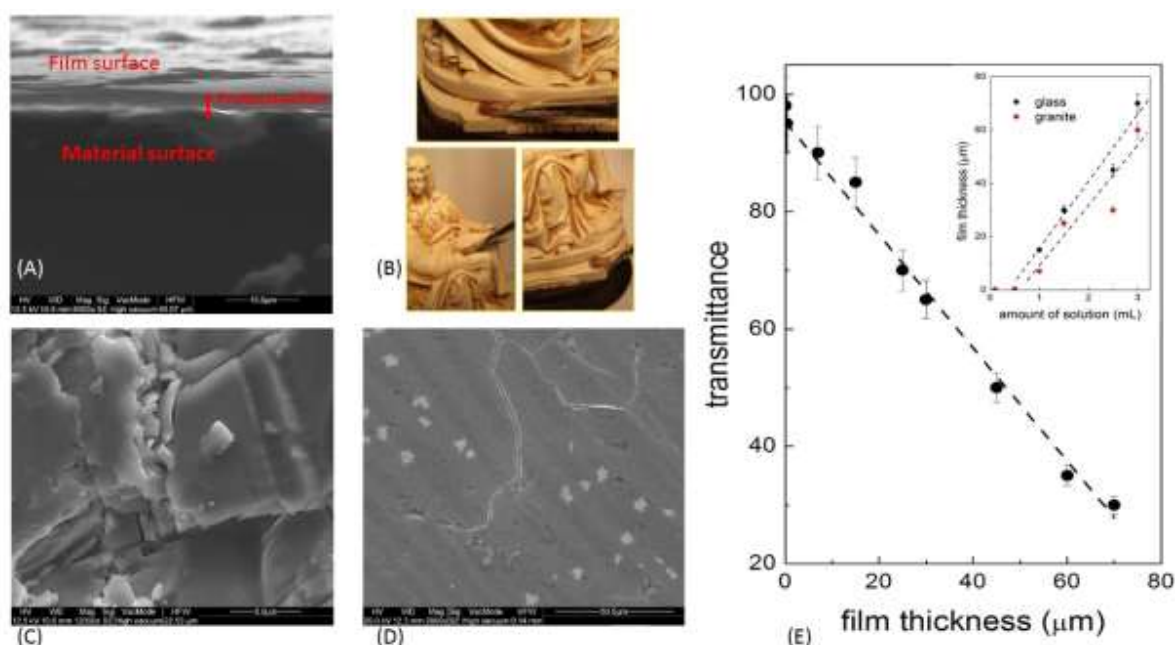


Figure 2 - Representative SEM image of (A) a graphene-loaded film deposited on a glass surface and (B) on a marble reproduction of “La Pietà” of Michelangelo; (C) SEM image of native granite, and (D) graphene-loaded film on granite surface; (E) transmittance (in %) obtained on non-porous (glass) surfaces. Data presented as average ± standard deviation (n = 10). The lines are showing the best linear fit of the data points. Inset in E: Film thickness (in μm) obtained on non-porous (glass) and porous (granite) surfaces (respectively black and red dots).

Aging method

Aged films are prepared according to the standard European procedures for artwork and architecture^{38,39}. Two accelerated aging procedures are evaluated, as suggested by European regulations. The first process simulates the effect of solar irradiation by exposing the film to a solar lamp (1.5 SUN) for 12 h. The used solar lamp is a Solar-3A by Oriel operating with a power at the

sample's surface of 100 mW/cm², which was constant in the entire light spot size (700 cm²). The second aging method simulates exposure to several cycles of freezing and thawing. Substrates are soaked for 1 week in cold water (constant temperature of 4 °C), which corresponds to the equivalent of 25 freeze-thaw cycles.

Analytical techniques

Morphological analysis of the material's surface before, during, and after bacteria exposure are performed by scanning electron microscopy (SEM) and atomic force microscopy (AFM). AFM images are obtained using an ICON AFM microscope from Bruker working in tapping mode. Each image is taken with a resolution of 512 × 512 pixels and a frequency of about 1 Hz. The shape and dimensions of the NPs are analysed by image analysis of a droplet of nanomaterial dispersion deposited onto a silicon substrate (~300 nanoparticles were analysed for each material). SEM analysis are conducted using a field emission SEM microscope (Quanta 200 F FEI/Philips) working with an energy of 20 keV.

Chemical information of all samples are obtained by Electron Dispersion X-ray (EDX) spectroscopy, under SEM conditions, simultaneously to the image acquisition, and X-ray Fluorescence Spectroscopy (XRF). The weight percent of each element in the film is obtained by the standard oxide analysis of the EDX data.

The optical transmittance of the films with different thicknesses is measured by depositing the films with different thicknesses on a glass substrate and irradiating the films with a white lamp (Energetiq LDLS, Laser Driven Light Source) under confocal microscope conditions (Olympus 900 by Horiba). The transmitted spectra are taken by a Triax 320 (Horiba–Jobyn–Yvon) spectrometer working in the 300–800 nm range. The transmittance is then evaluated using the standard equation:

$$t(\lambda) = \frac{I_t(\lambda)}{I_0(\lambda)} \quad (1)$$

where I_t and I_0 are, respectively, the transmitted and source intensity at each wavelength. The total transmittance is evaluated as the integral of $t(\lambda)$ on the whole visible range.

The hydrophobicity of the films is investigated by measuring the contact angle of a distilled water droplet of 5 μL (using a KSV NIMA Instruments Ltd CAM 200 optical contact meter). Each sample is measured 10 times to ensure data robustness and monitored during 24 h hours to determine how this parameter changes during the period allotted for exposure to bacteria.

Biological Tests

Preliminary test of the bactericidal activity of the films are performed against *E. coli* strain B in a standard “drop-cast” test. *E. coli* is chosen because it is a common bacteria, present in most environments and in contaminated water^{40,41,42}. Moreover, the inactivation of *E. coli* is crucial for preventing the bio-film formation caused by the contact between surface and contaminated waters^{43,44}.

Finally, *E. coli* is the best candidate for testing new materials because, differently from other bacteria, its action mechanism in biofilm formation and its interaction with graphene, fullerene, and TiO_2 are well-known. An inoculum from frozen glycerol stock (kept at $-80\text{ }^\circ\text{C}$) is streaked onto a LB agar plate and incubated at $37\text{ }^\circ\text{C}$ overnight. A single colony of *E. coli* cells is grown in a culture tube containing 7.5 mL of nutrient LB broth and incubated overnight on a rotary shaker (200 rpm) at $37\text{ }^\circ\text{C}$. A 50 μL droplet of bacteria solution (10^5 colony forming unit/mL) in PBS is deposited on each film to be analysed. The samples are then left at room temperature in the dark for 24 h. After exposure, the bacteria droplet is washed from the surface using 5 mL PBS and poured into a sterile culture tube. Finally, different volumes (1 μL , 10 μL , and 100 μL) of the resulting bacterial suspension sre deposited on the surface of an LB agar plate and incubated overnight at $37\text{ }^\circ\text{C}$. The number of bacterial colonies on the Petri dishes is counted after incubation.

Biological tests are performed on materials freshly coated with Sylgard 184, materials freshly coated with the bactericidal coatings, on correspondingly aged coatings, and on dispersions of nanomaterials in water (0.5%). The bactericidal properties are quantified as the percentage of bacterial colonies to survive after the 24 hours exposure, compared to the initial number in the bacterial test solution. The exposure time is chosen taking into consideration what typically performed in literature and in conventional tests of bactericidal agents for *E. coli* in water. These indicate a bacteria inactivation occurring in about 5-6 hours of contact with the bactericidal element^{45, 46}.

Finally, the analysis of the bacteria evolution as function of the exposure time to nanomaterials was performed on films loaded with 0.5 wt% TiO₂ deposited on granite. A series of bacteria droplets is deposited on 10 different samples. At given time intervals between 1 h and 24 h, the droplet is removed and the morphology of the film (and any bacteria present) is analysed by AFM.

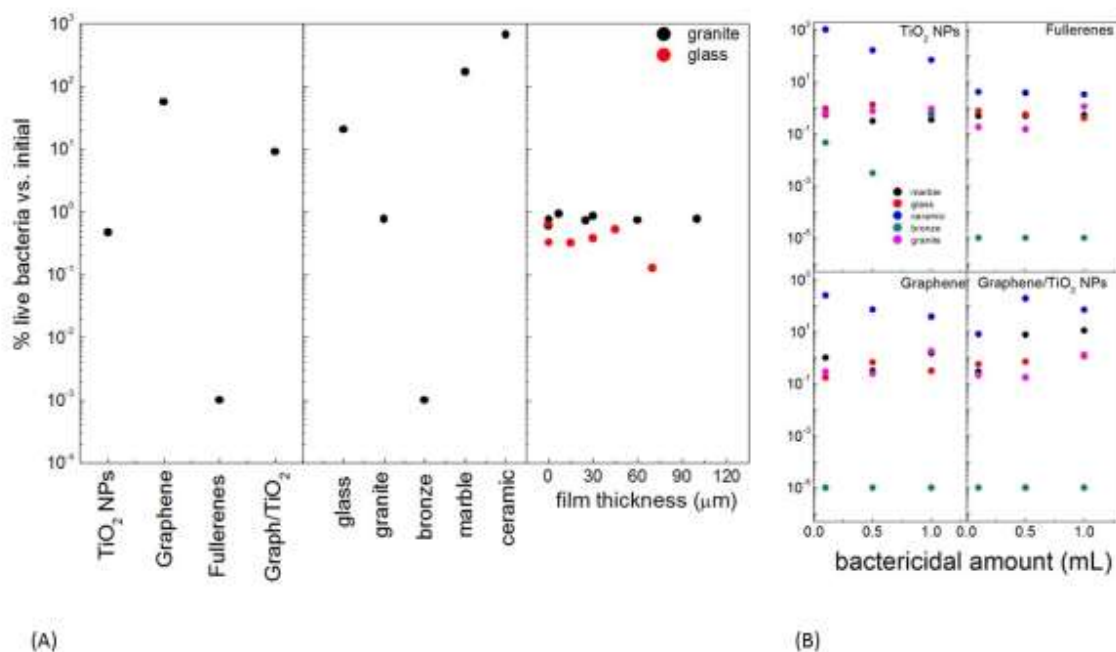


Figure 3 - (A) Survival (in %) of bacteria after 24 h of exposure to (from left to right) nanomaterial dispersions (water solution 0.5%), Sylgard films (500 nm), and films containing TiO₂ (0.5%) (as function of film thickness). Data presented as average \pm standard deviation ($n = 3$), error bars fall within the data point. (B) Survival (in %) of bacteria after a 24 h exposure to nanomaterial-loaded films. The value 10⁻⁵ % corresponds to case when no live bacteria were detected. Data presented as average \pm standard deviation ($n = 3$), error bars fall within the data point

3.1.3 Effectiveness of Protective Films

The thickness and uniformity of the films prepared by the different deposition methods are verified using SEM measurements. The representative SEM images shown in Figure 2 indicate that the film is uniformly deposited on the material surface (Figure 2A and 2B) and covers the porous and disordered surface of the materials (Figures 2C and 2D). The upper surface of the film appears smooth, without cracks or fractures that could allow the penetration of bacteria into the matrix. Measurements of the film thickness by SEM (Inset in Figure 2E for glass and granite) show that different thicknesses are obtained for porous and non-porous surfaces under identical deposition conditions. This suggests absorption of the uncured Sylgard 184 into the porous

materials (granite, ceramic, and marble) prior to polymerization. Finally, AFM images of the films containing nanomaterials show the presence of graphene flakes with dimensions of the order of several μm^2 and thicknesses of 2 nm (graphene multilayer composed by 5–7 layers), TiO_2 nanoparticles, or fullerenes aggregates with diameters of ~ 40 nm (see Figure 1). Films transmittance on glass shows the expected linear behaviour as a function of thickness (Figure 2E), passing from 95% for nanometric films to 10% for thicknesses in the hundreds of microns.

The lack of changes to the spectrum of light when passing through the films indicates that the latter are colourless. In addition, the films can be considered almost transparent up to 200 nm, while the transparency is reduced by about 30 % when reaching a thickness of 40–45 μm . The thickness of the films generated by spray-drying, brushing, and drop-casting are comparable for a given initial amount of uncured solution, suggesting that this coating can be reproducibly deposited on large surfaces by a variety of techniques. EDX and XRF analysis conducted before and after bacteria exposure indicate the absence of changes in the chemical composition of the film.

Preliminary biological tests are first conducted by directly mixing the bacteria solution with the nanomaterial dispersions (in water, Figure 3 A, left panel). After 24 h, no live bacteria remained when the bacteria are exposed to TiO_2 nanoparticles or fullerene aggregates, while a reduction in the survival rate has been observed for bacteria exposed to graphene flakes. Bacteria exposed to both graphene flakes and titania simultaneously, show a lower bactericidal effect than the one obtained when using only TiO_2 nanoparticles, but a higher effect than the one obtained when using only graphene. Differently from what is typically reported in the literature, a bactericidal action of titania nanoparticles is observed, despite the absence of UV-Visible irradiation.

This suggests that in this case bacterial cell death occurs due to an alternative mechanism, such as one linked to the dimensions of the nanoparticles and to the stress that is known to be induced by the interaction between small nanoparticles and the cell membrane. Analysis of the evolution of films containing 0.5 wt% TiO_2 (on granite) by AFM (see Figure 4A) indicates no obvious change to their morphology over 24 h. In addition, while isolated bacteria are observed after a 2 hours' time point, leading to the formation of aggregates ($\sim 15 \mu\text{m}$) after 3 hours, all traces of bacteria disappear after 6 h.

The bactericidal properties of films composed solely with Sylgard 184 (chosen as reference/control sample) are dependent on the material on which the Sylgard 184 is deposited. Strong bactericidal properties are observed for granite and bronze, while for ceramic, marble, and

glass, the bacteria are able to proliferate. The bactericidal properties of films containing TiO_2 are independent of their thickness for both porous and non-porous surfaces (Figure 3A, central panel), suggesting that the interaction between the nanomaterials and bacteria occurs directly at the film–water interface, without involving materials present in the bulk matrix of the material, such as residual Sylgard 184 monomers/oligomers. This result indicates that very thin and thus invisible films can be employed to protect surfaces without changing their esthetical properties.

To confirm this statement, the bactericidal properties of thin films (200 nm) containing different loadings of nanomaterials are examined when applied on different materials (see Figure 3B). Films containing fullerenes and titania nanoparticles are found to be more antibacterial than graphene. This is consistent to what has been found when testing only the NPs, without loading

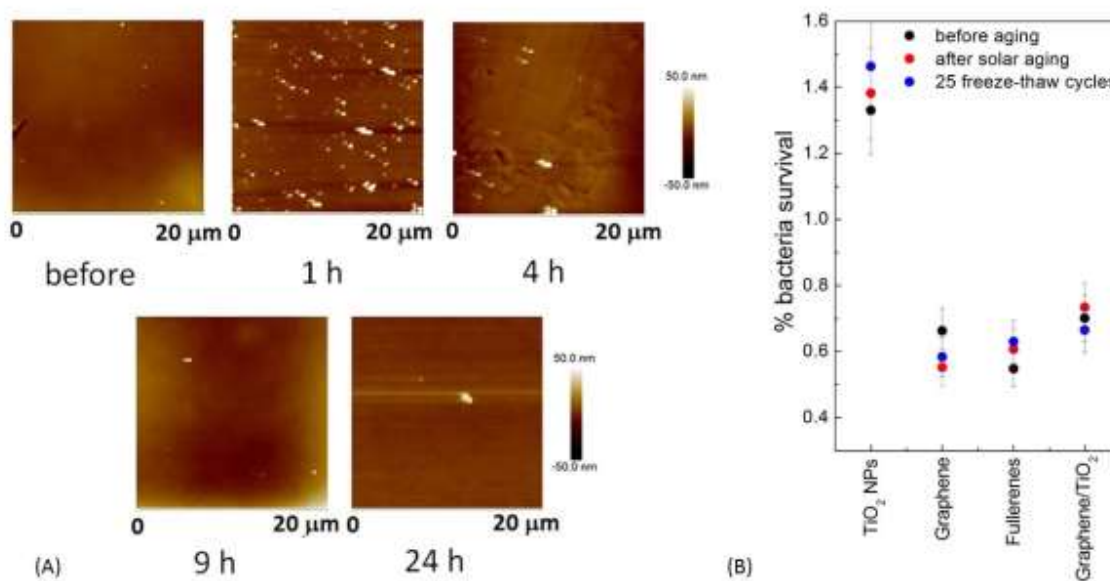


Figure 4 - (A) 2D AFM images of TiO_2 -loaded (0.5 wt%) films deposited on granite (as well as adsorbed bacteria) as function of exposure time. (B) Survival (in %) of bacteria after 24 h of exposure to loaded films (0.5 wt%) on granite for both, before and after accelerated aging processes. Data presented as average \pm standard deviation (n = 3).

them into a film. It should be noted that only very low loadings (0.1 wt%) of nanomaterials are necessary to observe potent antibacterial properties (no living bacteria detected), which is beneficial for maintaining transparency and colourlessness of the film. Films on porous ceramic surfaces behave differently from other materials, and show cell proliferation for all investigated nanomaterials. This suggests that diffusion of the film's constituents into the bulk material prior to polymerization may be occurring, leaving only a minimal amount of nanomaterial constituents on the unmodified exposed surface. This strongly reduces the hydrophobic effect and the amount

of nanomaterials at the interface with the bacteria. The value of the contact angle on the surface ceramic, in fact, is lower if compared to the ones of the other coated substrates.

Furthermore, all bronze samples (containing nanomaterials or not) display strong antibacterial properties. Indeed, XRF analysis indicate that copper atoms and ions are able to diffuse into the Sylgard 184 solution mixture, even before polymerization can occur. These species are well-known antibacterial agents. Thus, the deposition of a thin film of Sylgard 184 on bronze could be used to confer hydrophobicity, while diffusion of copper into the film act as an intrinsic antibacterial agent.

Finally, antibacterial tests performed before and after accelerated aging (Figure 4B), indicate the stability of the films for an equivalent of 25 freeze-thaw cycles and under solar irradiation. The bactericidal properties of the films are identical before and after the aging process (ANOVA, Tukey test, significance level <0.001 for both series of data).

In conclusion, this study demonstrates that very thin and optically transparent coatings can be conveniently prepared on the surface of materials of relevance for Civil Engineering, Architectonical Heritage, and building materials, including materials such as bronze, granite, marble, and glass. The films display potent antibacterial properties, and prevent the formation of biofilms under different test conditions. In addition, the antibacterial properties are unaffected by two accelerated aging tests, suggesting longevity in the real world setting.

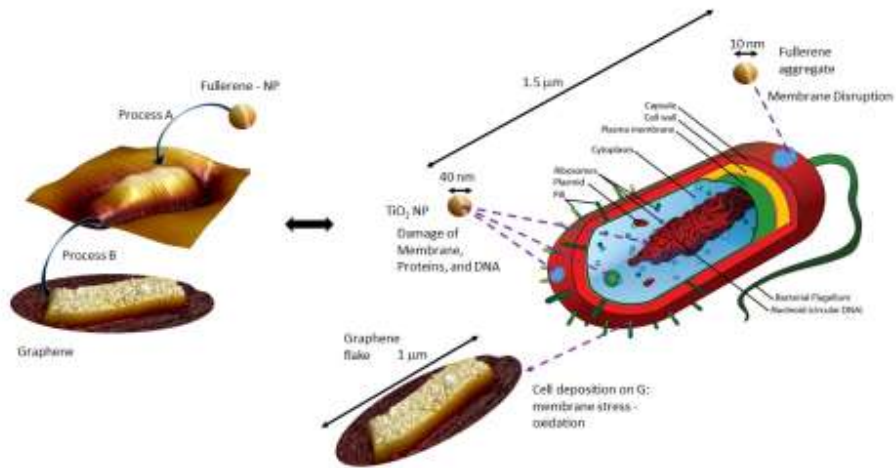


Figure 5 - Sketch of main bactericidal effects of investigated nanomaterials

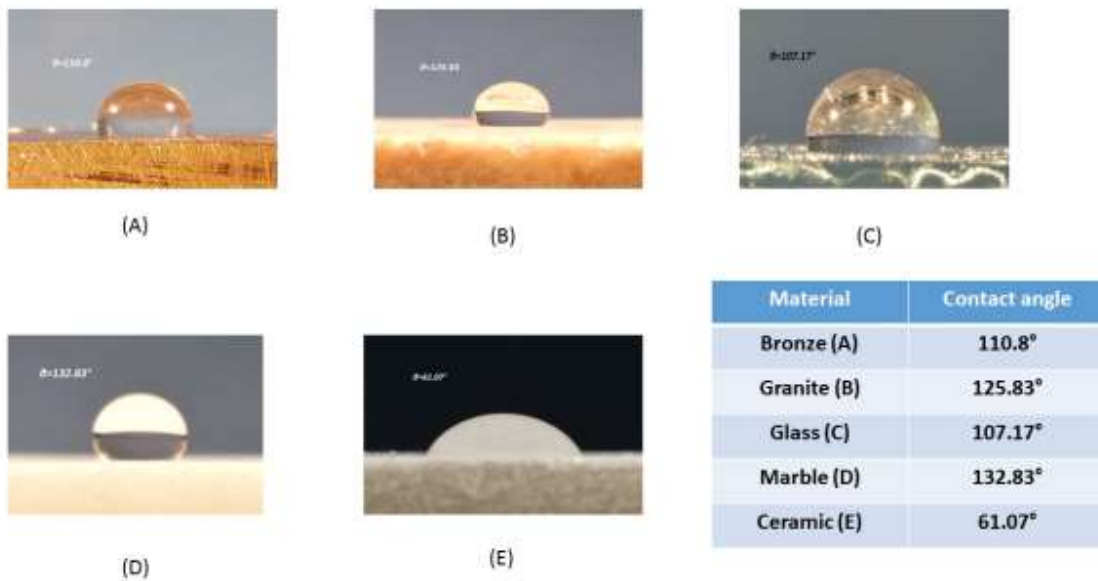


Figure 6 - Contact angle measurements for testing the film hydrophobicity

3.2 TiO₂ and SiO₂ nanoparticles film for cultural heritage: conservation and consolidation of ceramic artifacts

In the following, it is described a study of consolidation of ceramics artifacts with SiO₂ and TiO₂ nanoparticles. The nanoparticles are grown by laser ablation in solution and their shape and dimensions are monitored by optical absorption and AFM morphology studies. The colloidal solutions are mainly made of spherical nanoparticles with dimensions of about 10 and 15 nm following a LogNorm distribution with a standard deviation less than 1 nm.

The colloidal solution is then deposited on pottery surfaces to obtain a transparent film with thickness of about 1 micron. All chemical and morphological analysis indicate that the NPs consolidate the artifact penetrating in the deeper layer of surface and forming a transparent and hydrophobic film on surface. The adsorption process is a typical physisorption without formation of chemical bonds between NPs and constitutive elements of ceramic or introduction of external impurities, which can damage the materials.

Following the idea at the basis of nanostructured films growth, the main idea of this work is to realize highly roughness film on artifact surface using TiO₂ and SiO₂ NPs without causing chemical, morphological or aesthetical changes on artifacts. The difference in two works is that in the first case the particle are embedded into the Sylgard matrix, while now they are isolated on the artworks substrate. The NPs, in fact, are prepared as colloidal solution and then deposited on ceramic artifact.

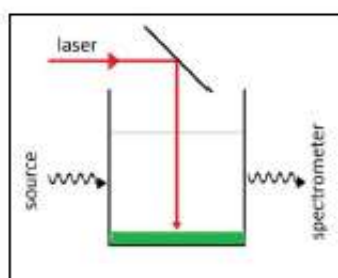
Table 1 : Element's percentage as function of depth profile

	<i>1.4 nm</i>	<i>1 nm</i>	<i>0.17 nm</i>
<i>Si</i>	9.69	9.82	4.6
<i>C</i>	64.6	66.4	8.02
<i>Ca</i>	8.12	4.1	2.8
<i>O</i>	15.4	17.9	11.9
<i>Ti</i>	1.67	0.88	0.36
<i>Sn</i>	0.44	0.84	

3.2.1 Particle preparation and characterization

TiO₂ and SiO₂ nanoparticles are produced by a laser ablation in solution (LASiS) method. 250 mg of TiO₂ grains, or a wafer of SiO₂ (both purchased from Good fellow with a purity greater than 90%), are deposited on the bottom of a cuvette, filled with 10 ml of acetone, and then irradiated with the first harmonic (1064 nm) of a Laser Nd:YAG (fluence of 500 mJ/cm², pulse of 7 ns and a frequency of 20 Hz).

Shape and dimensions of produced nanoparticles are controlled measuring the optical absorption of solution during irradiation and comparing the measured extinction cross section with that expected from electrodynamics theory^{47,48} (a sketch of experimental setup is showed in Figure 7A). Theoretical data for TiO₂ and SiO₂ NP are evaluated implementing the exact algorithm of Mie-Gans theory and using as chemical parameter for both materials the data in Palik Handbook⁴⁹.



(A)



(B)

Figure 7 - A) Sketch of experimental setup for LASiS; B) Picture of the altar of Sotterra Church (archeological site) and altar's fragment analyzed

Two different amounts of colloidal solutions (5 ml and 50 ml), are collected in the first 30 s of laser irradiation and spray-dried on several fragments of ceramic artifact (extracted from the altar of the “Sotterra” Church, south of Italy, Figure 7B), while a droplet of 50 μ l of colloidal solution is deposited on a silicon wafer for morphological and chemical analysis.

The two different amounts are deposited in order to study the penetration depth of NP in artifact (5 ml) and the formation of a NP layer on surface (50 ml). As in previous work, morphological analysis of both NPs are conducted by AFM microscopies, while SEM microscopy is used to study the morphology of particle layer deposited on ceramic artifact. Measurements of optical absorption during laser irradiation are obtained by irradiating the solution with a white lamp (Energetiq LDLS, Laser Driven Light Source), and taking the transmitted spectra by means of a Triax 320 (Horiba-Jobyn–Yvon) spectrometer, which works in the 300-800 nm range. The extinction cross-section and optical absorption are then evaluated using the standard equations:

$$\epsilon(\lambda) = -\text{Log} \frac{I_t(\lambda)}{I_0(\lambda)} \quad (2)$$

$$a(\lambda) = 1 - \frac{I_t(\lambda)}{I_0(\lambda)} \quad (3)$$

Where I_t , I_0 , a , and ϵ are, respectively, the transmitted and source intensity, the absorption coefficient and the extinction cross-section at each wavelength.

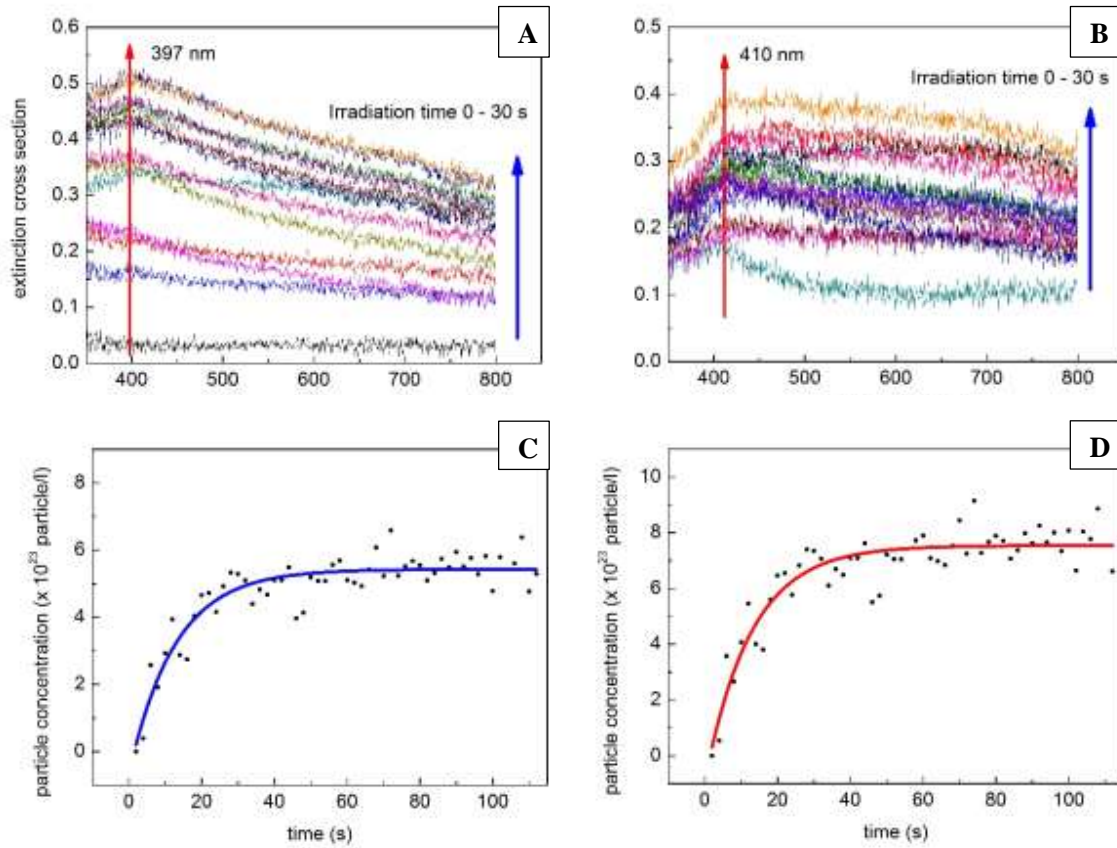


Figure 8 - Extinction cross section in the first 30 s of irradiation for SiO₂ (A) and TiO₂ (B) NP. Particle concentration evolution during LASiS for SiO₂ (C) and TiO₂ (D).

Particle concentration in solution is evaluated from optical absorption of colloidal solution using the Lambert and Beer law:

$$a = c * \sigma * l \quad (4)$$

Where c is the particle concentration, σ the molar extinction cross section (obtained from chemistry handbook⁴⁹) and l the optical path length in our experimental setup (1 cm).

Chemical information on all samples are obtained from Electron Dispersion X-ray (EDX) spectroscopy, under SEM conditions (realized simultaneously to images acquisition), and X-ray photoelectron spectroscopy (XPS). XPS experiments are conducted in a UHV chamber equipped for standard surface analysis with a pressure in the order of 10^{-9} torr. Non-monochromatic Mg-K α X-ray ($h\nu=1253.64$ eV) is used as excitation source while XPS spectra are calibrated with the C1s peak of a pure carbon sample (energy position 284.6 eV).

All XPS spectra are corrected for analyzer transmission and the background is subtracted using the straight-line subtraction mode. In order to evaluate the penetration depth of NP on surface we evaluate the depth profile of TiO₂. The measurements are taken using data acquired in an angular dependent XPS experiment⁵⁰, where we measured photoemission at three different photoemission angles (45°, 60° and 80°) evaluating the penetration length with the Hill method⁵¹:

$$t = -\lambda \cos\theta \ln\left(1 + \frac{I_0/S_0}{I_s/S_s}\right) \quad (5)$$

Where t is the penetration length and λ the mean free path of photoelectron.

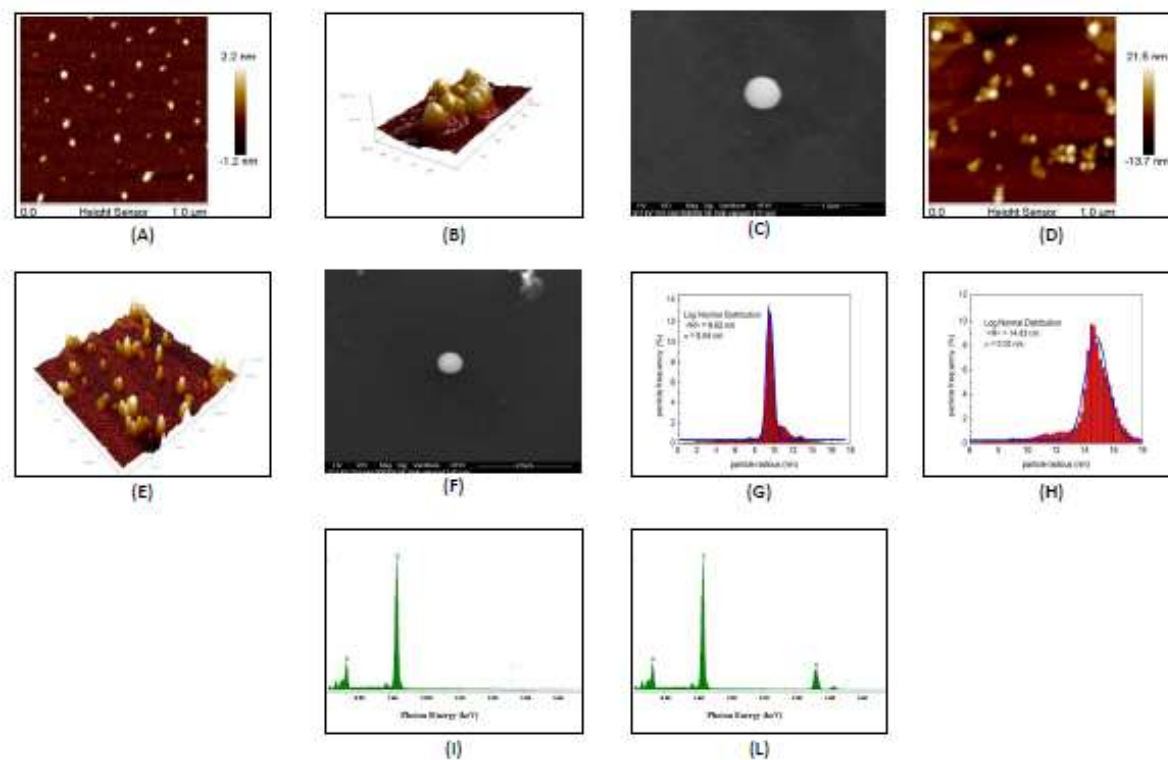


Figure 9 - AFM and SEM images for SiO₂ (A B C) and TiO₂ (D E F). Distribution of particle radius for SiO₂ (G) and TiO₂ (H). EDX measurements taken on a single NP for SiO₂ (I) and TiO₂ (L)

We assume that the ceramic matrix is mainly constituted by amorphous Silicon Dioxide and assume that the mean free path of Ti 2p photoelectron in this network is 2.04 nm⁵². In order to verify the influence of NP introduction on natural luminescence emission and, then, on thermoluminescence (TL) dating process, Photoluminescence (PL) measurements are taken. PL spectroscopy is performed by an Olympus microscope (Horiba-Jobyn Yvon) mounting objectives with 10X, 50X and 100X magnifications. The microscope is equipped by a 375 nm-laser source with a power of 15 mW, for PL, and by a Triax 320 (Horiba-Jobyn–Yvon) spectrometer working in the 200-1500 nm range. Finally, the hydrophobic properties of artifact is measured by contact angle measurements obtained depositing a droplet of 2 μ l on artifact surface.

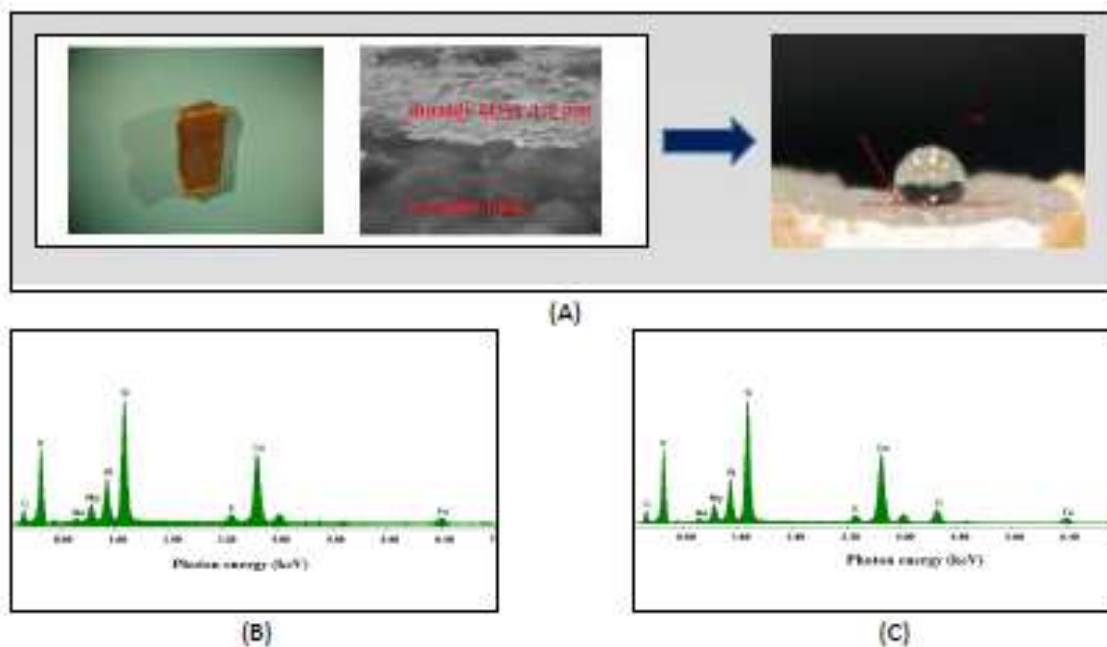


Figure 10 - SEM and optical images (A) of TiO₂ layer on ceramic surface, contact angle on layer (A) and EDX measurements before (B) and after (C) NP deposition

3.2.3 Nanoparticles effectiveness in artwork consolidation process

Analysis of extinction cross-section during irradiation (Figures 8A and 8B) and of temporal evolution of particle concentration (Figures 8C and 8D) indicate the formation of particle with radius of 10 nm for SiO₂ and 15 nm for TiO₂ NP in the first 25 s of irradiation. After that time, an aggregation between NP start and particles with greater dimensions nucleate in solution. In the first 25 s the extinction cross-section increases in intensity while the plasmonic peak is fixed at position 397 nm for SiO₂ and 410 nm for TiO₂, indicating that particles with well-defined dimensions are present in solution and their concentration increases linearly (as visible in concentration evolution in Figures 8C and 8D).

We can conclude that in this case only the primary particles produced by laser irradiation are present in solution. For irradiation times greater than 25 s, the solution becomes dark, the plasmonic peak shows a red-shift, and the concentration of primary particles reaches a saturation level: therefore, we can conclude that at 25-30 s a process of particle aggregation starts in solution. Only the particles

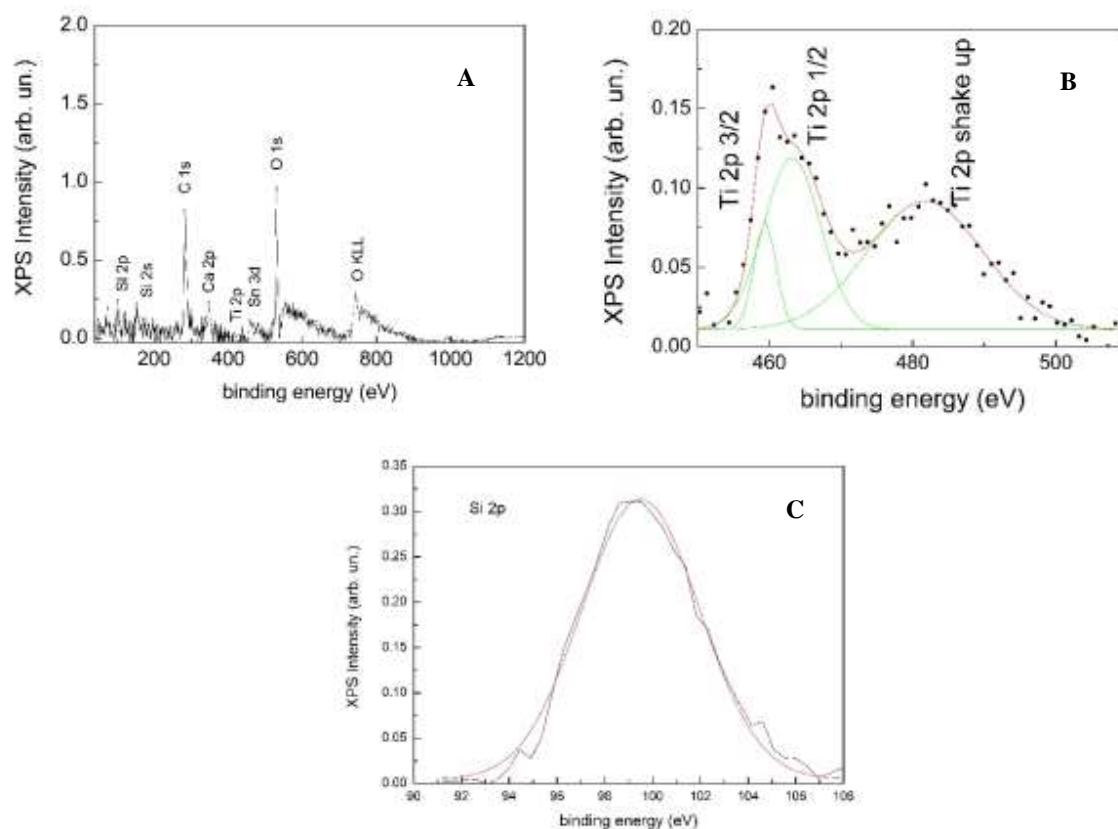


Figure 11 - XPS survey spectrum (A), Si 2p (B) and TiO₂ (C) details

produced in the first 25 s are deposited on artifact surface and characterized by AFM and SEM microscopies. AFM and SEM images (Figures from 9A to 9F) confirm the previsions of extinction cross section analysis showing the presence of particles with dimension distributed as a LogNorm distribution⁵³ (see Histograms in Figure 9G and 9H), with averages at 9.82 nm and 14.83 nm for SiO₂ and TiO₂ NPs, respectively, and very low standard deviations (in the range of 0.02 nm for both particles species). EDX measurements (fig. 9I and 9L) conducted on a series of NPs indicated the only presence on particle of titanium, oxygen, and silicon, without presence of external impurities introduced during the growth process.

SEM and EDX analysis conducted on ceramic artifacts with deposited NPs layer (50 ml of colloidal solution, Figures 10A, 10B and 10C for the deposition of TiO₂ NPs as example for both species of NPs), indicate the formation on sample surface of a uniform layer of NPs, without introduction of external impurities or damage on surface. Moreover the layer is perfectly

transparent. The results of depth profile analysis, taken on fragments with a deposition of 5 ml of solution, are summarized on Figure 11 and Table 1.

The XPS spectra, as EDX, show the only presence on surface of constituting elements of ceramic and of NPs, confirming the absence of external impurities. Ti 2p and Si 2p lines are centered at positions typical of corresponding dioxide⁵⁴, indicating the absence of chemical bonds between NPs and chemical elements in artifacts and the physisorption nature of NPs adsorption. The depth profile, taken for Ti 2p photoelectron, indicates that, after a deposition of a small amount of colloidal solution (5 ml), the NP are prevalently concentrated in the lowest layer of surface. This

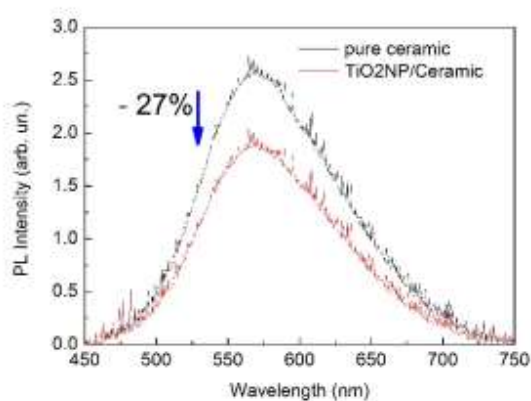


Figure 12 - Photoluminescence spectrum taken after deposition of solution

suggests that NP penetrates the pore of ceramic consolidating the Photoluminescence spectra material's surface

PL measurements (Figure 12) indicate a decrease in natural luminescence emission of about 27% after deposition of both NPs without shift in band position which keep these typical of ceramic artifacts and ascribed amorphous silicon dioxide^{55, 56}. The shift absence in PL bands confirm the absence of chemical bonds obtained by XPS measurements while the decreases of PL intensity is caused by the reconstruction of ceramic pores which can change the network structure (PL intensity is strongly related to the network configuration of a material). These results suggest a strong influence of insertion of NP on the possibility of dating by thermoluminescence measurement. Finally, contact angle measurements (Figure 10A) indicate that only the formation of NP layer on surface can ensure the hydrophobicity; in fact, only the fragments with a deposition of 50 ml and a formation of NP layer show a great contact angle.

3.3 AFM and Pulsed Laser Ablation Methods for Cultural Heritage: Application to Archaeometric Analysis of Stone Artifacts

This section introduces the use of the Atomic Force Microscope (AFM) and of the Pulsed Laser Ablation (PLA) as methods for morphological diagnostic with nanoscale precision of archeological artifacts and corrosive patina removal from stone artifacts. We test our methodology on stone artifacts extracted from the Church of Sotterra (located in Calabria, south of Italy). The AFM microscopy is compared with different petrographic, chemical, optical and morphological analysis methods for identifying the textural characteristics, evaluating the state of preservation, and formulating some hypotheses about the provenance and composition of the impurity patina located on the artifact surfaces.

We demonstrate that with the nanometric precision obtained with AFM microscopy it is possible to distinguish the different states of preservation, much better than using conventional petrographic methods. The surface's roughness is evaluated from very small artifact's fragments, reducing the coring at micrometric scale with a minimal damage for the artworks. After the diagnosis, we performed restoration tests using the PLA method and compared it with the more common micro sand blasting under dry conditions. We find that the PLA is highly effective for the removal of the surficial patina, with a control of a few hundreds of nm during the surface cleaning, without introducing chemical or morphological damages on the artifacts. Moreover, PLA can be easily implemented in underwater conditions; this has the great advantage that stone and pottery artifacts for marine archeological sites don't need to be removed from the site.

3.3.1 Nanoscience Methods for Protection and Restoration: the idea

Correct interpretation on the age and the history of Cultural Heritage requires the use of very sensitive diagnostic techniques, which allow identification of the constituent materials and, from there, the understanding of the artwork origin. This information is required when designing a restoration project, which preserves not only the visible aspect of the artworks but also their original chemical and mineralogical composition.

The Diagnostic and Restoration methods are, generally, based on physical and chemical methods for defining artifacts properties and better conceiving the restoration and conservation projects^{57,58,59}. Unfortunately, in most cases, they give only a macroscopic description of the artifacts on a scale in the order of mm or microns, without being able to control the corrosive patina on the surfaces and the damage caused by the restoration processes with higher spatial precision, e.g. on a nanometric scale. A nanometric control is highly desirable since it allows the removal of the corrosive patina in its initial phase of formation with a strong reduction - in terms of time and cost – in the restoration process, thus making all conservation actions more efficient.

In this work, we propose the use of two well-known physical analysis methods, the AFM and the PLA, as support to the more common Cultural Heritage analysis methods, in order to have a nanometric control on the morphological properties of the stone artifacts and to achieve a controlled removal of the nanometric patina layer. These two methods are routinely applied in the field of nanoscience and nanotechnology for nanomaterials growth and characterization, with a control in the few to hundreds of nanometers scale. These dimensions are comparable to the ones of a corrosive and biological patina on the artifacts in its initial formation phase.

In this paper, we demonstrate the effectiveness of these methods in a particular case study using some stone artifacts extracted from the Church of *Sotterra* (Paola, Calabria - Italy). We applied the AFM and PLA methods jointly with the common diagnostic methods (either in-situ and in laboratory), in order to characterize the materials, identify the pits of their origin, detect the chemical composition of surface patina, and define a strategy for the restoration and conservation^{60,61, 62}.

3.3.2 The case study: the *Sotterra* Church

The Church is located in an underground site on the Tyrrhenian coast of South Italy (see the geographical collocation on Figure13A). Its architecture is Paleo-Christian and can be described as a basilica with a single nave, rectangular and slightly elongated, terminating in an apse, with smooth walls and divided up by three arches made of local stone (Figure13B)⁶³. In addition, the Church is considered as one of the main representation of Byzantine art in Calabria^{64,65}. A strong moist environment, caused by frequent flooding, characterizes the Church atmosphere and contributes to the formation of a corrosive patina on the surface and in the

deterioration of paints and stone artifacts. Several restoration processes, conducted since the Middle Age, make it difficult to identify the original materials and the dating of the Church.

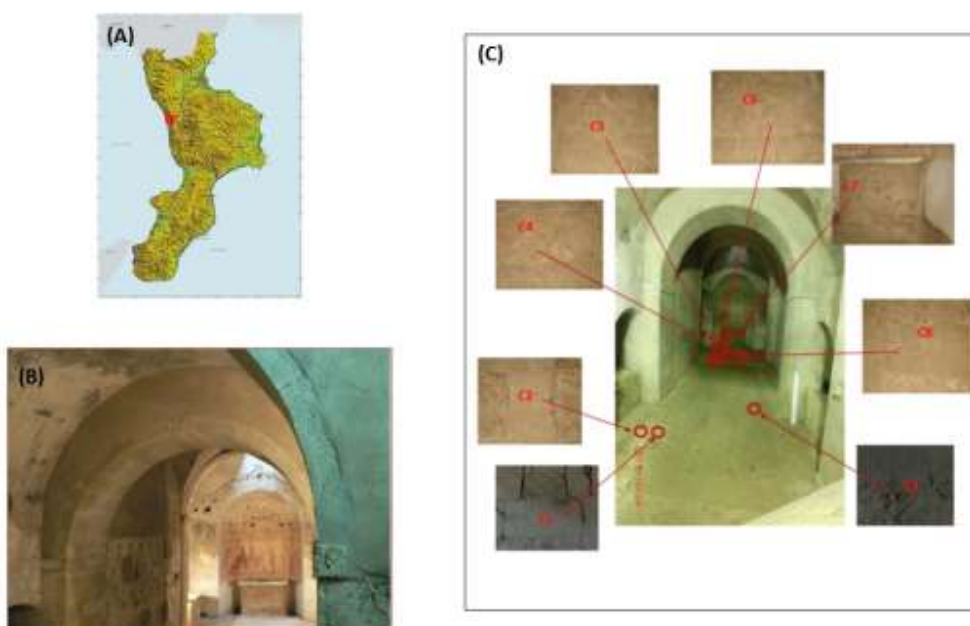


Figure 13 - Archeological site: (A) geographical position, (B) the inside of the Church, (C) samples and position where they have been found within the church

A dating of the Church, based on the analysis of some paint pigments, indicates that in the first Middle Age the Church was already built while some ecclesiastic documents indicate that the consecration and construction of Church occurred only in the late Middle Age^{63,65}. A dating process of the Church using direct methods such as Thermoluminescence of Radiocarbon is impossible due to the absence of any ceramic, wood, or organic (tissues, bones, etc...) remains, the only artifacts attributable to the original construction being the floor, the altar, and the paints. Hence, a deeper analysis is necessary to better understand the pits of provenience of the materials and to better define the origin of the Church.

Our analysis has been made based on 8 stone fragments taken from the floor and the altar and using 1) Optical microscopy (OM), 2) SEM and 3) AFM microscopies, 4) EDX (energy dispersive X-ray analysis), 5) XPS (X-ray photoelectron emission), 6) XRF (X-ray fluorescence), and 7) PL (photoluminescence) spectroscopies. Moreover, each sample is restored with the pulsed laser ablation⁶⁶ to check if this method can be considered an alternative to those conventionally

used in-situ⁶⁷. For Italian Cultural Heritage, conventional restorative processes are regulated by the UNI Normal standard⁶⁸.

They suggest very different restorative processes: 1) laser ablation (continuous laser) cleaning with water spray, 2) micro sand blasting under dry condition, 3) cleanup by chemical solvents (distilled water, solvents, and slightly basic solutions such as AB57 the ICR and ammonium carbonate), and 4) technical extraction of soluble salts by chemical reactions. The choice of the correct methods to apply depends on the artifact's materials and on their conservation status.

Table 2: Sample Roughness evaluated from AFM images

<i>Sample</i>	Roughness (nm)
<i>C1</i>	89
<i>C2</i>	166
<i>C3</i>	61
<i>C4</i>	129
<i>C5</i>	52
<i>C6</i>	87
<i>C7</i>	16
<i>C8</i>	96

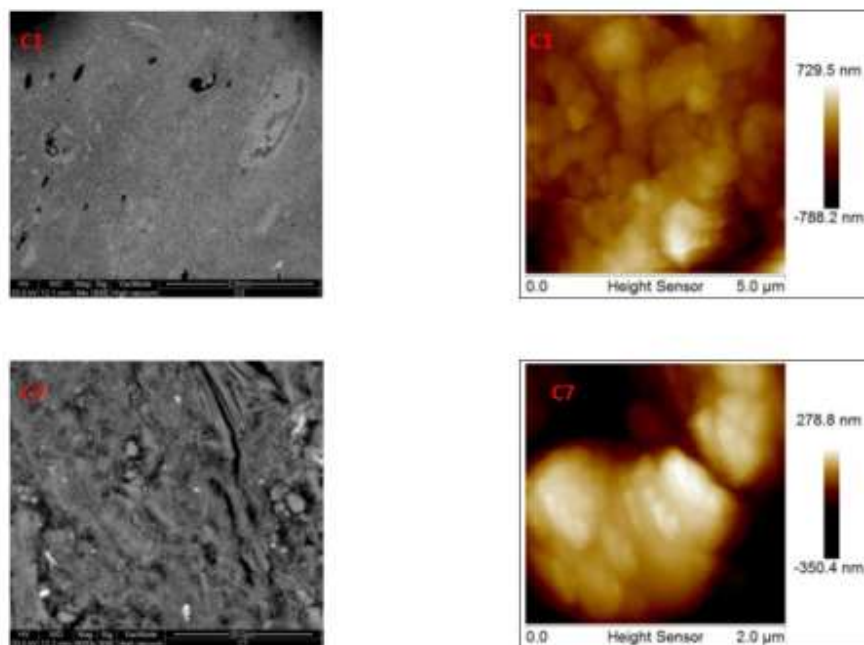


Figure 14 - SEM and AFM images of C1 and C7 samples as example for all samples

The experiments are conducted on a series of samples (C1-C8) with areas of 1 cm x 1 cm and thicknesses of about 2 cm (Figure 13C). All samples are composed, in a first analysis, by stone, and are strongly deteriorated by moist and biological agents, as witnessed by the presence of a white patina on the surface. The samples have been taken from different sites distributed on the floor and on the altar of the Church, as indicated in Figure 13C. Each sample is subjected to petrographic, chemical, optical and morphological analysis using different techniques (XPS, XRF, -EDX, PL, SEM, AFM), in order to identify the mineralogical and chemical composition of the materials and their alterations. Moreover, after samples characterization, their surface has been treated by a PLA cleaning process in order to eliminate the surface patina⁶⁹.

This process is compared with the traditional method of micro sand blasting conducted under dry condition⁶⁷. All the chemical, optical, and morphological analysis have been conducted before and after the cleaning process. The mineralogical and petrographic studies of the collected samples are performed by OM on thin sections using a Zeiss–Axioplane Microscope equipped with polarizing and reflected optical light. Chemical analysis are performed by XPS and XRF

spectroscopies to obtain information on both surfaces (XPS) and the bulk (XRF) of the artifacts. XPS measurements are conducted in an ultra-high vacuum (UHV) chamber equipped for standard surface analysis with a pressure in the range of 10^{-9} Torr. Non-monochromatic Mg-K α X-ray ($h\nu = 1,253.64$ eV) is used as excitation source. The XPS spectra are calibrated with the C1s peak of a pure carbon sample (energy position 284.6 eV) and the data are fitted assuming a Gaussian distribution. XRF measurements are conducted with a X-123 SDD apparatus (Amptek - USA), equipped by a gold cathode and a beryllium revelator, operating at fixed angle.

PL measurements are taken with an Olympus microscope (Horiba-Jobyn Yvon) mounting objectives with 10 \times , 50 \times and 100 \times magnifications. The microscope is equipped with a 378 nm-laser source with a power of 12 mW and by a Triax 320 (Horiba Jobin Yvon) spectrometer working in the 200 - 1500 nm range.

Finally, morphologic information has been obtained by both, SEM and AFM microscopies. The SEM images are taken using a Cambridge Stereoscan SEM working with a 20 keV electron beam and a current of 3.4 mA, in either secondary electron acquisition mode (SE-SEM) and backscattering acquisition mode (BSE-SEM). The AFM images are taken with a Bruker AFM microscope (Icon Bruker) working in the tapping mode. Each image was taken with a resolution of 512 x 512 pixels on an area of a few microns (we took images with a maximum scan size of 5x5 μ m). The AFM images are analyzed by the Nanoscope software by Bruker in order to retrieve the surface roughness and control the damage on the surface on a hundreds of nm scale.

After characterization, the samples C1 and C8 are subjected to a PLA process in order to evaluate its effectiveness in removing the surface patina and to verify a possible change in the chemical composition or in morphology. The pulsed laser ablation procedure is performed by irradiating for 30 minutes each sample with a Nd: YAG laser with energy of 550 mJ/pulse operating at 1064 nm, 20 Hz, and a pulse length of 7 ns (Commercial Quanta-Giant series 710 laser).

PLA process is performed in air and in water by vertically placing the sample in a glass vessel (transparent to the wavelength 1064 nm) filled with marine water. The aim of testing PLA in underwater condition is to verify its effectiveness in removing the patina surface in locations with a high level of humidity (such as can be found in *Sotterra*) or underwater (among the common restoration methods, only the laser ablation can be performed in under-water condition).

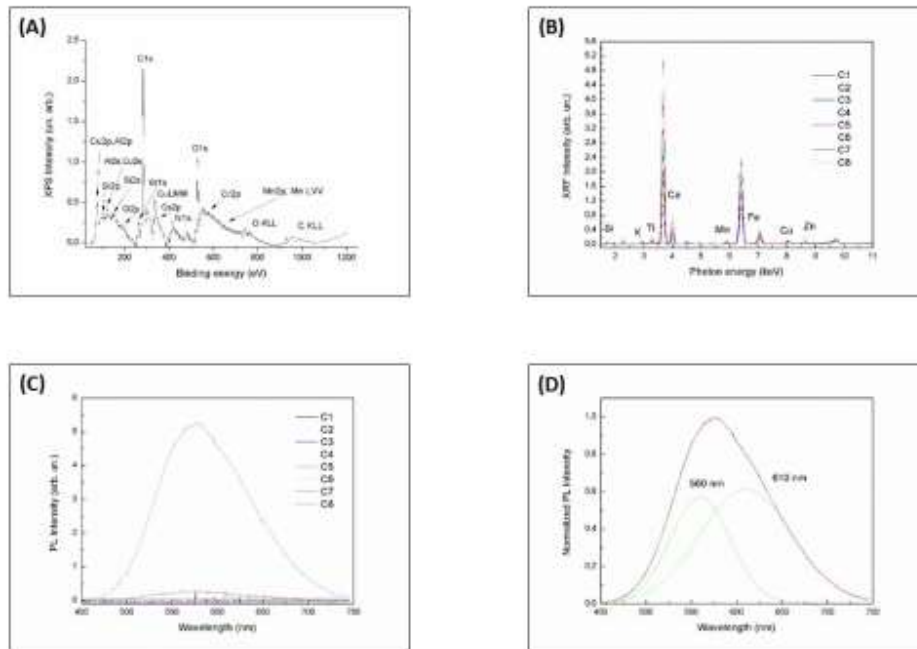


Figure 15 - Chemical analysis on samples: (A) XPS survey spectrum, XRF (B), Photoluminescence (C), and Gaussian analysis of PL spectrum of C4 sample (D)

Finally, the laser ablation cleaning process is compared to the micro sand blasting technique⁶⁷, conventionally used for the restoration of buildings external walls⁷⁰. The blasting dry is performed with a micro sandblasting on which we mounted nozzles with a diameter from a few tens of microns up to 0.8 mm and with a working pressure of 2 to 4 bar.

Morphological images of the samples surfaces (see Figure 14 showing SEM and AFM images of samples C1 and C7 as example for all samples) indicate that all samples show the same morphology, consisting in a random distribution of the grains with a size in the order of a few nanometers.

Analysis of the surface roughness indicates that the conservation status of each artifact is strongly dependent on the extraction zone: in fact, a reduced roughness is observed on sample C7, which comes from the altar (see Table 2) but, due to its intrinsic location within the church, is also the less exposed to usury. As we describe in the following, all the diagnostic methods are in perfect agreement with the AFM analysis and the roughness measurements, indicating that the items

extracted from the floor show the same morphological composition and a conservation status perfectly described by the roughness analysis.

Moreover, as indicated in the experimental section, the AFM analysis requires fragments with dimensions of the order of few microns, while for petrographic and mineralogical analysis we need thin sections with dimensions of the order of several mm.

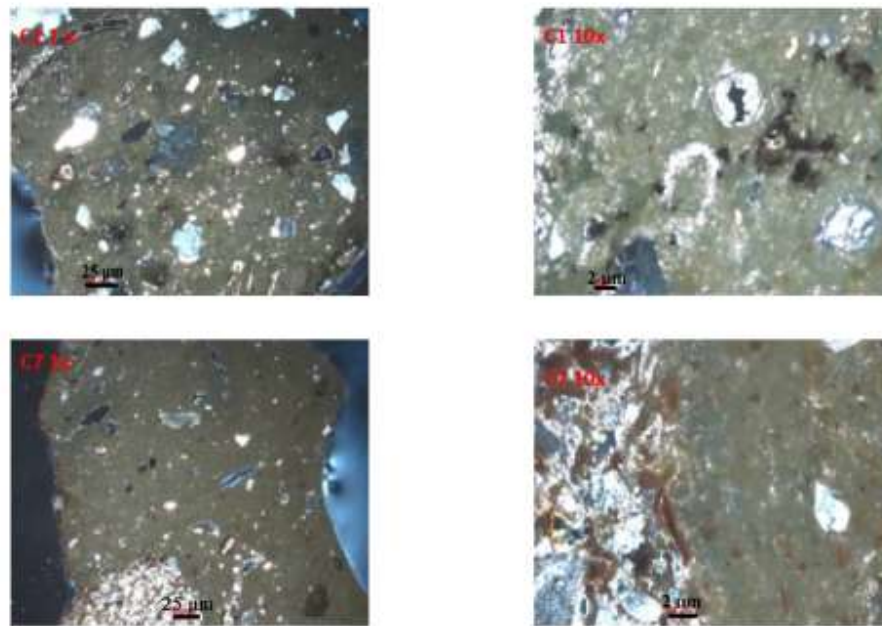


Figure 16 - Optical microscopy images for petrographic analysis (samples C1 and C7 as example for all samples)

Table 3 : Position of main XPS peaks for each element

	<i>C1</i>	<i>C2</i>	<i>C3</i>	<i>C4</i>	<i>C5</i>	<i>C6</i>	<i>C7</i>	<i>C8</i>
<i>Si 2p</i>	103.6	103.2	103.8	102.7	102.9	102.5	103.1	103.9
<i>C 1s</i>	284.2	284.8	283.4	284.1	284.8	284.2	284.2	283.9
<i>O 1s</i>	531.6	531.9	530.8	531.1	531.7	531.0	531.0	531.8
<i>Ca 2p</i>	350.9	349.1		351.5	350.1	349.2	349.2	348.2

The chemical composition information of the samples are obtained from XRF and XPS spectra (see Figures 15A and 15B). The spectra indicate that the main elements on the surface are C, Si, O and Ca, with trace elements of F, Na, Mg, Al, Cl, K, Cr and Fe. The main positions of the XPS peaks for each element, summarized in Table 3, are those of pure elements, without formation of chemical bonds between impurities and the matrix. The only exception is represented by the position of a Ca 2p line, at about 351 eV, indicating the presence of Ca-O or Ca=O structures⁵⁴ and, then, of a calcium carbonates matrix (CaCO₃)⁵⁴.

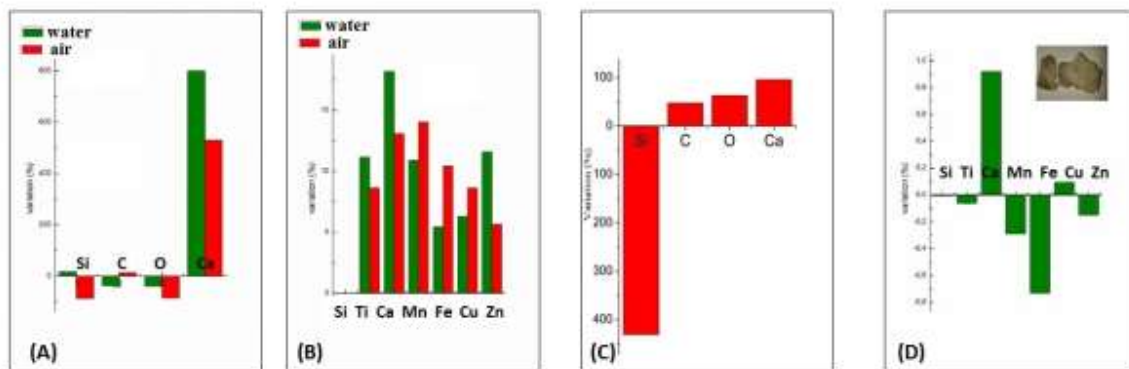


Figure 17 - Variation of elements with LA and sand blasting cleaning on surface and bulk evaluated respectively by XPS and XRF (A-B for LA and C-D for sand blasting). Inset in D: a fragment of sample broken after sand blasting cleaning

These conclusions are confirmed by petrographic and mineralogical analysis conducted using OM on thin sections. The optical images (Figure 16 shows the images for samples C1 and C7 as benchmark for all samples) indicate that all the samples are composed in general by a matrix of marl with silico-clastic fragments of granite origin.

The different matrixes, as easily obtained from the roughness analysis by AFM images, show a different status of conservation, clearly visible in the grain size of the granite, which varies from gross to fine. In details, the fragments with higher roughness (C1, C2, and C4) appear, also at petrographic analysis, as the most deteriorated, showing an altered matrix with secondary porosity while C3, C7 and C8 (lower roughness) show a well preserved matrix without sign of band dissolution.

The found items can therefore be classified as natural stones mainly composed by sedimentary rocks of carbonate in a marl matrix; the different distribution of the aggregate may indicate that the fragments were picked up from different stratigraphic levels of rocks.

Finally, PL measurements in Figure 15C show a lower intensity of the PL signal, with the exception of C4, suggesting that the origin and the composition of these fragments is different from that of the others. After a Gaussian analysis (Figure 15D), the luminescence signal reveals two main bands around 560 and 610 nm, which can be attributed to quartz inclusions (SiO_2)⁷¹. Indeed, these bands are both typical for quartz and are intrinsic of the bulk structure⁷¹.

The comparison between the chemical and mineralogical composition of our finds and a series of previous geological studies on the pits of Calabria, allows to conclude that the materials used in the Church construction were taken from a quarry found along the Tyrrhenian coast of Northern Calabria, rich in this natural stone⁷².

As described in the experimental section, PLA cleaning was performed in air (C8) and marine water (C1) to investigate process effectiveness for in-situ restoration for both terrestrial and underwater sites^{69,73}. In the following, we demonstrate that PLA is much more efficient than classical restoration methods and moreover it does not cause any damages to the artifacts. In the classical Laser Ablation the continuous irradiation with a high energetic laser beam can strongly increase the surface temperature (the irradiated area can reach temperatures in the order of a few thousands K)⁷⁴.

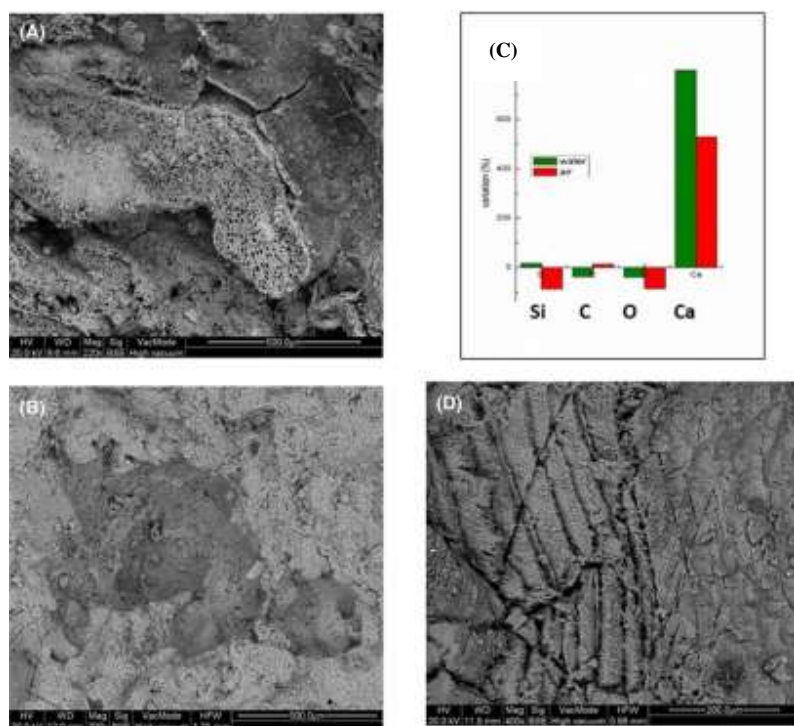


Figure 18 - Variation of surface morphology and chemistry with PLA cleaning on surface; a) and b) SEM images of biological patina before and after PLA; c) variation of chemical elements on surface verified by XPS analysis before and after PLA; d) SEM images after sandblasting cleaning

In PLA, however, the temperature increases only during the pulse interaction (with a duration in the order of ns) and the average temperature on the sample surface is in the order of a few hundred K, without damaging the artifacts. Moreover, with PLA it is possible to remove only the surface patina, controlling the thickness of the removed layer simply varying the duration of the ablation and without changing the chemical composition of the artifacts matrix.

The white patina on the stones artifacts, with a thickness of about 500 nm, has been completely removed after 30 seconds of irradiation in marine water and 40 seconds in air. The variation of the percentage of constitutive elements, obtained by XPS measurements before and after the PLA (see Figure 18C), demonstrates that PLA, as LA, is more effective in water than in air. In fact, the percentage of C on the surface increases on the sample ablated in air, indicating absorption of CO₂ from the atmosphere. Conversely, the sample ablated in water shows an increase of the percentage of Si and Ca, and a decrease of C and O.

The percentage of the elements evaluated by XRF (see Figure 17B) shows an increase of the intensity of all constituents indicating the effectiveness of the PLA in the removal of the patina. Cleaning process by micro sand blasting dry was performed on sample C6 using grains with dimension of a few hundreds of microns injected at a pressure of 3 bar for a duration of 10 seconds. As it is well known, this method completely removes the surface patina (Figure 17C and 17D for XPS and XRF measurements) but creates some micro-fractures on the surface, which can seriously damage the artifact (see Inset in the Figure 17D). XRF results confirm those of XPS also for the bulk, only Cu and Ca increase in concentration (Figure 17D).

In conclusion, with PLA is possible to remove only the surface patina coatings without altering the chemical composition of the samples or creating micro-fractures, which could cause damage to the artworks.

4. Innovative Laser-Plasma Diagnostics for Cultural Heritage

This Chapter discusses two innovative laser-plasma based diagnostics for application in the Cultural Heritage (CH) world. In details, it demonstrates the feasibility of a *one-shot PIXE* spectroscopy and of *Plasma-Induced Luminescence*. For both diagnostics, the Chapter starts describing first the conceptual method, then the design of the experimental setup, the theoretical simulations, the method's feasibility, the experimental results, and finally discusses the results. All the results are compared with those obtained by the corresponding classical methods (see Chapter 2 for the details).

Furthermore, the design of the proton beam line for *one-shot PIXE* suggests the possibility to conceive new nanostructured targets to model proton beams dedicated to CH diagnostic. The discussion about these new nanostructured targets is included at the end of the paragraph about the One-Shot PIXE.

4.1 *One-shot PIXE* diagnostic

As previously discussed, during the last years, many research groups have carried out several studies to improve diagnostics able to investigate the Cultural Heritage based on morphological and chemical analysis. The efforts aim to obtain the highest possible number of chemical information at the same time without causing any damage to the artifact as well as revealing both the array elements and the trace elements. In order to obtain a complete chemistry of the bulk material, the use of more sophisticated (and expensive) nuclear physics techniques such as Particle (proton) Induced x-ray and Gamma Emission (PIXE and PIGE)¹ is typically required.

In the classic PIXE and PIGE, heavy charged particles (i.e. protons, alpha-particles or sometimes heavy ions) are used to create inner-shell vacancies in the atoms of the specimen. This leads to the emission of X-rays and Gamma-rays produced by de-excitation of these vacancies. The X-ray and Gamma-ray radiation can be measured in order to have a characteristic fingerprint of each chemical element present in the analyzed bulk sample. In conventional facilities, a small Van de Graff accelerator or a compact cyclotron produce the incident charged-particle beam (typically consisting of protons with a mean energy of 1-5 MeV). The advantages of PIXE spectroscopy on the other X-ray spectroscopies are various:

- The proton beam can be focused and transported by electrostatic or electromagnetic devices/optics over large distances
- The analysis is characterized by a variable spatial resolution, since it is easier to manipulate a proton beam's geometry. Hence, it is possible to obtain a more accurate analysis.
- The protons can reach a higher depth than that reached by the X-rays, which, in the case of Cultural Heritage might allow to go back to the period of its manufacturing or to the discovery of a different construction technique.

Furthermore, PIXE allows performing analysis with a high spatial resolution, since protons can be focused up to a beam diameter in the micrometer range.

Currently, PIXE is used for the analysis of a wide range of materials, from proteins to cells and tissues, from polymers to ancient pigments and artifacts. Typically, in the classical PIXE the mean energy of the proton beam is $\sim 1\text{-}5$ MeV, the beam current lies in the 10-150 nA range and a spectrum with an x-ray count rate in the order of 800-2000 counts/seconds is generated². In the Cultural Heritage field, PIXE and PIGE spectroscopy are performed in few worldwide typical facilities, such as AGLAE³, located at the French Louvre Laboratory C2RMF⁴ or INFN-LABEC^{5,6} located in Florence with a conventional proton accelerator (energies 1 to 5 MeV, beam current from 10 pA to nA). Both these facilities are able to perform measurements on spot areas in the order of ~ 10 μm (up to 500 μm). This means that it is necessary to take numerous measurements, from 10 to 100 (where each point requires around 100-9000 s), to collect the complete chemical information retrieving the elemental composition of the sample. The great disadvantage of these facilities is the extremely long analysis time that they require, which implies a potential damaging of the artifacts induced by the proton irradiation⁷. The maximum analysis depth that can be obtained in these facilities is between 2-20 microns, due to the limited energy range of conventional facilities. This depth is typical for biological film, surface patina, or bronze cancer (cuprite and malachite). The analysis is therefore limited to deteriorated layers without information on the pristine material bulk. Moreover, these conventional diagnostic methods are not easily tunable and adaptable (typically, tuning the accelerator energy requires at least tens of minutes) which often reduces their application to certain energy ranges and to micrometric surface areas.

4.1.1 Laser-driven PIXE: the idea and the conception of the experiment

The advent of high-power, ultra-short lasers has opened up possibilities of laser-based particle acceleration, including protons^{8,9} as a potential alternative to conventional accelerators based on radio-frequency (RF) or electrostatic technology. The investigation and application of these laser-accelerated beams is currently challenging many research laboratories especially for the attractive characteristics of these sources such as compactness, efficiency, versatility and tunability. Laser-based particle beams present the advantage of having a high current (kA), strong laminarity at the source (emittance about 100 times better than conventional accelerators), short duration (ps scale), and small source size (tens of μm)¹⁰. One of the more commonly exploited laser-driven proton acceleration mechanisms is the TNSA (Target Normal Sheath Acceleration), where a focused laser pulse irradiates a solid target that acts as proton source as pictured in Figure 1. In this acceleration process the laser pulse generates hot electrons that escape the bulk of the target and form a negatively charged sheath at $\sim 1 \mu\text{m}$ distance from the rear surface of the target. Over this short distance a charge separation field (up to TV/m) is created, leading to the ionization and acceleration of the water contaminants (mainly Hydrogen) that are present on the back surface. The ion beam is therefore accelerated normally from the rear surface of the irradiated target.

Currently, multi-hundred-TW power, table-top laser systems can generate on-target intensities of $\sim 10^{19}$ - 10^{20} W/cm², accelerating proton beams up to energies of ~ 15 - 20 MeV, with a typical laser-to-proton energy conversion efficiency of 1-6 %^{11,12, 13} and a peak current in the kA regime (each laser shot produces about 10^{13} protons).

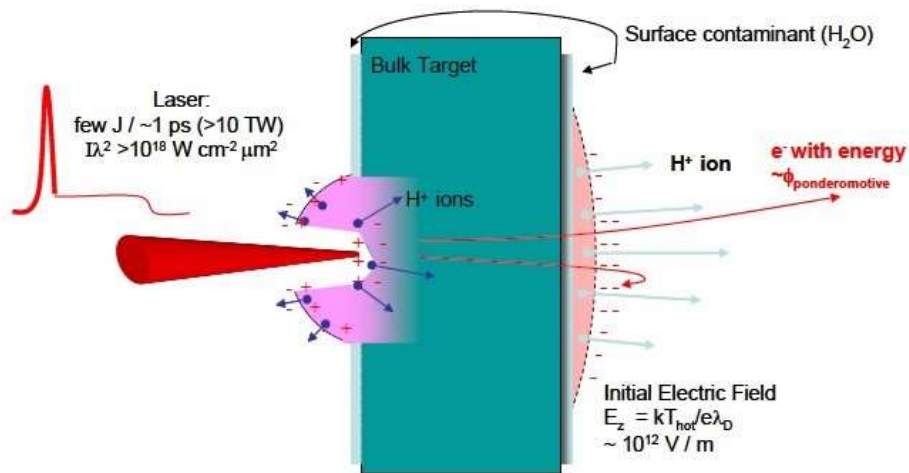


Figure 1 - Basic scheme for the TNSA acceleration process from the rear surface of a solid target. Electrons from the bulk are accelerated and create a strong electric field on the rear surface that ionizes water contaminants and accelerates them orthogonally from the back side of the target. Extracted from the PhD thesis of P. Antici [61]

The main purpose of the work that is presented in this section, is to study the use of laser-accelerated proton beams as a novel excitation source for performing PIXE analysis of materials (see Figure 2A). The laser-accelerated proton beams can be used as a diagnostics tool in the field of Cultural Heritage and, moreover, can improve the techniques that are based on conventional PIXE and PIGE spectroscopies. In details, laser-based protons have the potential advantage of allowing:

- 1) a complete chemical analysis on a larger volume of the artworks, analyzing surfaces in the order of cm²;
- 2) a scan of a larger bulk volume allows a quicker identification if there are chemical elements in it requiring further investigation (e.g. harmful elements);
- 3) a deeper and more precise “layer by layer” analysis, since the beam energy can be tuned from few MeV to tens of MeV within a very short timescale;
- 4) a more precise investigation can then be performed with higher resolution, i.e. a smaller spot size and a more precise depth, in the considered volume (e.g. in order to find harmful elements, or in the contrary e.g. if no harmful elements could be detected on the larger volume, this means that the scanned area is “clean/healthy”, and the analysis can continue on another part of the artefact);
- 5) depending on the facility, a higher punctual dose (obtained in one or more shots).

The thesis work focuses on improving diagnostic techniques performed with non-portable, quite costly facilities (accelerators). Since in this case the criteria of portability for both technologies (conventional and laser) is not applicable, a direct comparison is justified (current table-top lasers obtaining laser-driven MeV protons are still far from being portable, as well as conventional accelerators in this energy range). Our setup is similar to a typical PIXE setup used in the Cultural Heritage field, with the only difference being that the conventional ion source is replaced with a laser-based one (the detailed setup is described later). The high-power laser is impinging on a commercially available solid target, which acts as the proton source. The laser-generated protons are used to irradiate a sample positioned at a variable distance from the source, as reported in Figure 2).

The X/Gamma-rays produced in the interaction between the laser-generated protons and the sample to be probed, are detected by an X/Gamma-ray detector that is monitoring the interaction region. Our approach and experimental methodology has a strong technical similarity with other recently developed techniques aiming at using laser-generated protons in different applications, particularly medical applications¹⁴.

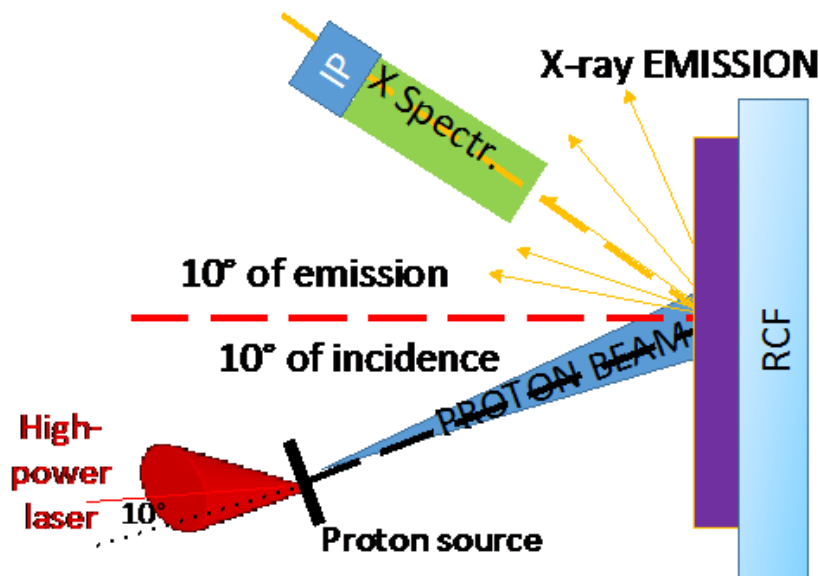


Figure 2 - Experimental Setup used for the one-shot PIXE

Different pioneering papers have tackled issues linked to our approach and experimental methodology, such as:

- 1) availability in air (obtained e.g. using a 7.5 μm -thick polyimide vacuum window¹ or 23 to 50 μm Mylar or Krypton window^{15,16};
- 2) suppression of parasitic radiation (obtained e.g. using a deflecting magnet in order to avoid unwanted X-ray radiation from the target interfering with the direct source-aperture line-of-sight^{1,15} or stopping potential contributions from low-energy carbon ions using a thick foil¹⁷);
- 3) fast energy selection (obtained e.g. using chicane of magnetic dipoles¹⁸ or a combination of Radio-Frequency Cavity and quadrupole-sequence¹⁹). In this thesis, we have not emphasized these adjustments since they have already been covered by the above-cited references.

4.1.2 Numerical simulations: the feasibility of the method

Using numerical simulations, we reproduce the effects of irradiating materials of interest for Cultural Heritage (CH) with laser-accelerated proton beams. The aim is to reproduce the thermodynamically induced stress on the sample's surface in order to test the possible induced damage and to choose the best experimental conditions and parameters.

The interaction between the different laser-generated proton spectra and the sample target is simulated with a two-dimensional Montecarlo code, in which we inserted as proton heating source a laser-generated proton beam obtained in previous published experiments (see references later). The laser-generated proton beam is modelled as the projection of a proton virtual point source with diverging rays, generating a proton source with diameter of 50 μm . This proton source modelling is similar to the one described in Ref.¹¹ with the laminarity of the beam calculated as indicated in Ref¹⁹. The half angle divergence of the proton beam (α) has been adjusted depending on the considered proton energy, as reported in Ref²⁰. Within the opening angle, all particles are uniformly distributed. This modelling is a standard in the field of particle-matter interaction for measuring proton-induced heating effects²¹.

Regarding the proton spectra, since the laser-driven proton yield is heavily dependent on the laser-facility, we need to consider different laser scenarios which - for simplicity - we rationalize as being able to be represented by the following four different laser-categories:

- 1) Very high-energy, long pulse laser - currently difficult to obtain commercially such as the LLNL-TITAN laser (maximum energy: up to 220 J, typical pulse duration: 700 fs, central wavelength: 1.056 μm , repetition-rate $\ll 1$ Hz)^{22,23};
- 2) High-energy laser, long pulse laser - currently difficult to obtain commercially, but not out of reach for industry, such as the LULI-ELFIE (30 J, 350 fs, 1.056 μm , rep-rate $\ll 1$ Hz)²⁴;
- 3) High energy, short pulse laser - similar to what can be obtained commercially as 1 PW laser (e.g. from Amplitude Technologies or Thales Optoelectronics), such as the ASTRA-GEMINI (10 J, 45 fs, 800 nm, envisioned rep-rate for future facilities 5-10 Hz (e.g. at the Extreme Light Infrastructure)²⁵);
- 4) High-energy, short pulse laser - commercially available as 100-500 TW laser (e.g. from Amplitude technologies) such as the FZD-DRACO laser (5 J, 25 fs, 800 nm, rep-rate 10 Hz)²⁶

A comparison of the different spectra obtained from the different laser-facilities is shown in Figure 3. The TITAN spectrum has been obtained during the experimental campaign described later on in this chapter.

As a starting point for our simulations, we use the spectra having the highest number of particles, i.e. the TITAN spectrum with 10^{13} particles produced for each shot (as you can see in the Figure 3), in order to have a sufficient flux to perform a “one-shot” PIXE analysis. On the other side, it is likely that this proton flux will heat the irradiated target to the highest temperatures (“worst case scenario”).

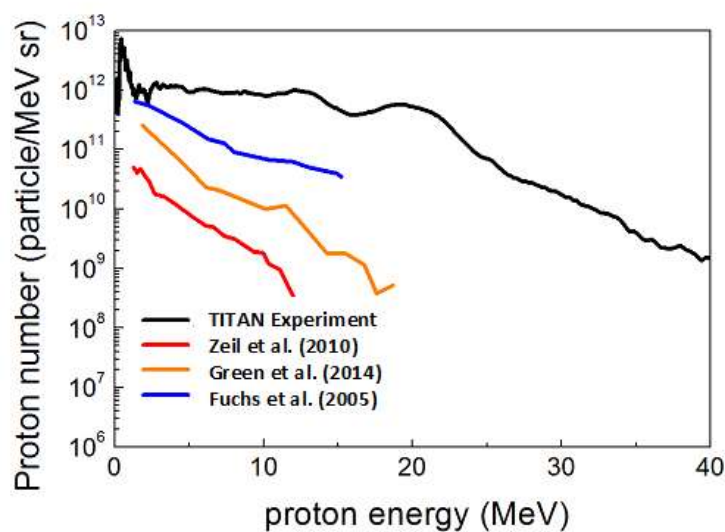


Figure 3 - Comparison of different proton spectra obtained for 4 different laser-facilities operating in different energy/pulse duration ranges. The TITAN spectrum is obtained during the experimental campaign

We focus firstly on a few main material categories of interest in the Cultural Heritage, which include bronzes, marbles (stone carbonates), noble metals (gold, silver) and ceramics. In the simulations, we position the sample at different distances from the proton source and evaluate the heating effect. We need to ensure that the temperature within the sample stays safely below the melting point. However, as we mentioned before the more proton flux goes onto the sample, the more X-ray emission will occur, which will improve the signal-to-noise ratio of the PIXE diagnostic.

In our setup conditions (TITAN laser) and for the ceramic sample (which is one of the most critical items, having a melting temperature of $\sim 1600^{\circ}\text{C}$), the safe distance in order not to reach the melting point of the sample, is found to be about 6 cm from the proton source (see Figure 4A). In order to find the right distance to which the samples should be placed we did a series of simulations. We chose the minimum distance from the source that did not cause the melting of all investigated materials.

The results of the numerical simulations are shown in the temperature maps of Figure 4B, obtained for the cases of silver, ceramic and marble samples (we took them as references for the most common CH materials). These data have been obtained at 50 ps after arrival of the protons on the target using the TITAN proton spectrum. One can see that within the whole analysed depth of the samples, the temperature stays safely ($\sim 25\%$) below the melting point for all the considered materials (the melting temperature of marble, silver and ceramic are respectively about 960, 1400 and 1600°C). We check the temperature map 50 ps after the irradiation because the heating onset time for the samples is in the order of tens of ps²⁷. Therefore, in this timeframe the materials have reached their maximum temperature during the heating process. The simulations also reveal that the temperature stays almost constant for a few ns before the cooling phase starts and the samples cool down almost completely in a few tens of ns.

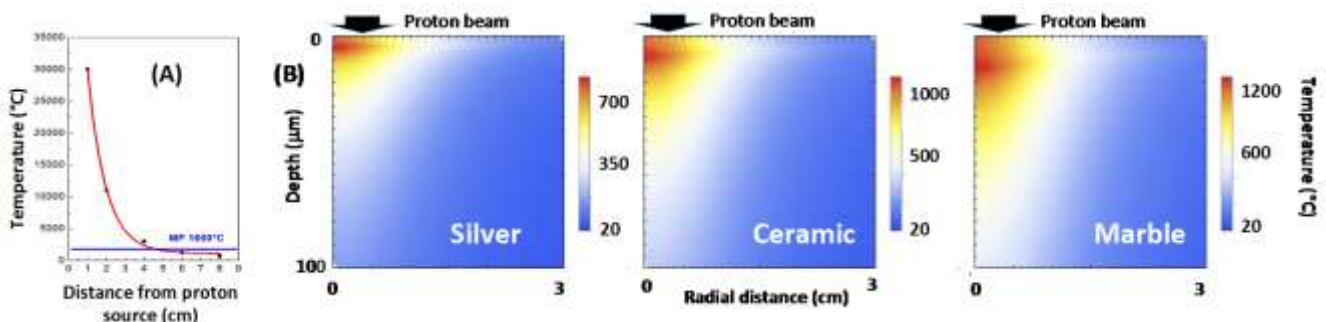


Figure 4 – (A) Simulated maximum temperature vs. distance from the proton source for a ceramic artifact when irradiated with the laser-generated proton beam as obtained on the TITAN laser. (B) Temperature maps, obtained with the Montecarlo code, of a silver, ceramic and marble

4.1.3 One-shot PIXE: the experiments

We validate the numerical results obtained for the above mentioned cases by performing a series of experiments using the TITAN laser of the Jupiter Laser facility (Lawrence Livermore National Laboratory - LLNL). This laser system is capable of producing laser pulses of about 220 J in 700 fs and operating at a wavelength of $1.054 \mu\text{m}^{22}$. The laser beam, focused down to a spot with $\sim 9 \mu\text{m}$ diameter (FWHM) and having an intensity of $I \sim 10^{20} \text{ W/cm}^2$ on the target, interacts with a commercially available solid target in order to accelerate protons in the laser-forward direction using the TNSA²⁸ mechanism. The Amplified Spontaneous Emission (ASE) has been measured to be $< 10^{-6}$ in contrast, i.e. delivering $\sim 10 \text{ mJ}$ in energy. As proton source targets, we used solid $15 \mu\text{m}$ thick Au (or Al targets), manufactured by Goodfellow, depending on the artifact to be probed. The Al target has been used instead of the Au target for those cases where a Gold sample has been proton-irradiated for performing PIXE analysis. This allowed us to differentiate the X-ray signal coming from the proton source from the one coming from the irradiated sample. The incident laser was tilted by 10° with respect to the target normal direction, in order to differentiate between the trajectories of the protons stemming out normally from the back surface and the electrons following the laser-direction. As proton diagnostics, we used two calibrated Thomson parabolas (TPs) and spectrometers located at 0° (TP 0°) and 9° (TP 9°) with respect to the main laser pulse axis, in order to measure the forward generated proton spectrum.

The TPs were placed respectively at a distance of 690 and 565 mm from the proton source (distance to the entrance slit). The proton spectra measured by the TPs were readout in an absolute manner^{29,30} using Image Plates (IP) of the type BAS-TR 2025 from Fuji Photo Film Co. Ltd, which were analyzed using a FUJIFILM FLA-7000 reader. Additional information about the proton spectra were obtained using Radio Chromic Films (RCFs) of the type HS, which also allowed to analyze the beam spatial distribution. A typical laser-generated proton spectrum obtained at TITAN during the experiment is shown in Figure 5

The spectrum shows energies starting from a few hundreds of keV to a maximum energy cut-off as high as tens of MeV and an higher number of particles (10^{13}) that allow us to have a sufficient flux for performing a “one-shot” PIXE analysis.

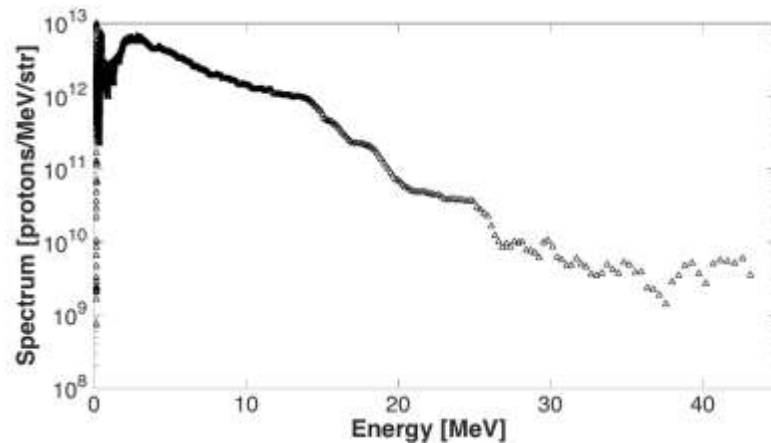


Figure 5 - Typical energy spectrum of a TNSA accelerated proton beam as obtained on the TITAN laser facility in 2016. The number of protons decays exponentially, reaching a maximum energy of tens of MeV.

As sample we used pure silver (97%, thickness 200 μm , impurities of Cr, Ti and Cu, manufacturer: Good fellow), gold and bronze (thickness 200 μm , manufacturer: Goodfellow), pure Carrara marble (provider: Le pietre srl), and one ancient ceramic (taken from the medieval archaeological situ of Nicastro, South of Italy, see Figure 6A; provider: Sovraintendenza ai Beni Culturali of the Region of Calabria, Italy). The latter is a decorated fragment of an amphora (Figure 6A) dated year 1650 AD³¹. All the samples were located at 6 cm from the proton source and the laser-generated protons were impinging the sample with an incidence angle of 10° . At first, we verify the effect of the proton irradiation on the target surfaces (see Figure 6) for the above-described setup (as you can see in Figure 2). This is performed by morphological and chemical analysis on all the irradiated materials before and after the irradiation (as reported in the following paragraph).

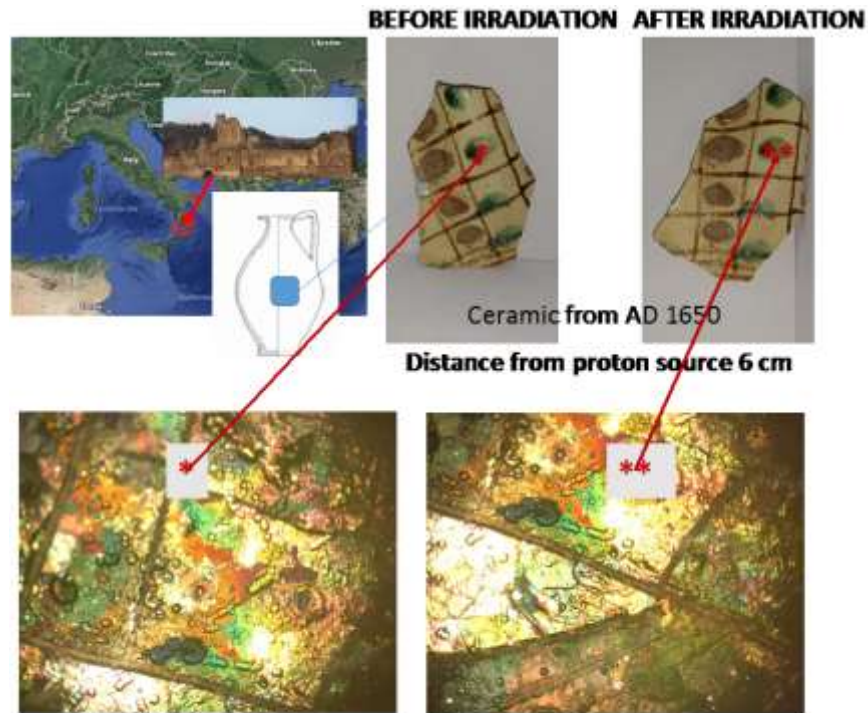


Figure 6 - Archeological situ and details about the ceramics used for testing the damaging effect of the laser-generated protons during the one-shot PIXE; Images show the artifact before and after the irradiation

4.1.4 One-Shot PIXE: Results and Discussion

All tests performed on the irradiated samples positioned in the above-described setup indicate non-perturbative morphological or chemical changes on the artifacts. Figure 6 and 7 show, as an example for all, the results obtained for the ceramic sample, which is the most critical sample we irradiated. The morphological analysis, conducted by optical microscope (OM), indicates the absence of fractures and cracks on surface, confirming then the possibility to use the proton beam on fragile artifacts too (as you can see from the optical images in the Figure 6). The chemical analysis, conducted firstly by EDX analysis under SEM conditions, shows the absence of chemical changes on the materials surface and inside the bulk (within an analyzed depth of 10 microns). Furthermore, we have monitored the XRF emission of the sample before and after irradiation (see Figure 7A), which indicates a slight decreasing of the Ca, Fe and Cu lines: the proton beam causes an ablation of the first micron of the surface on the sample. However, this effect is not recognizable by eye and can also occur in the case of irradiation with conventional proton beams.

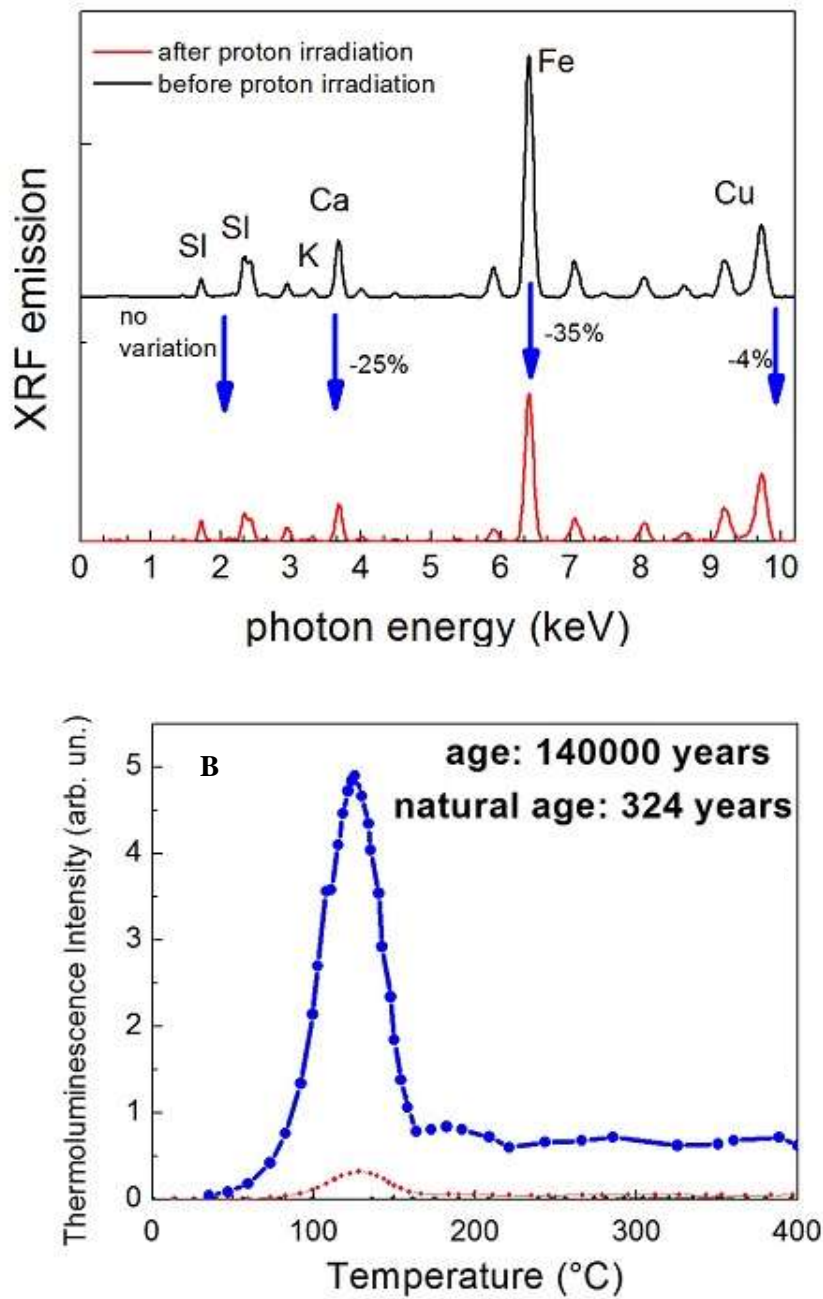


Figure 7 – (A) XRF optical image of the sample before and after irradiation; (B) Results of the dating process performed before and after irradiation

This said, as it is the case when applying conventional methods, it is no longer possible to obtain the dating of the artifact, because the high-cumulated dose during the PIXE strongly affects the thermoluminescence (TL) of the material sample.

As specified in Ref.³¹, the TL technique for analysing most artifacts is based on the amount of radiative dose cumulated during the artifact's lifecycle (Paleodose). In detail, the sample age is evaluated as the ratio between the Paleodose (Gy) and the Dose Year (Gy/year) of the archaeological site. The irradiation with high energetic protons can strongly change the radiation cumulated into the finding, changing the Paleodose and affecting the dating process. We checked the (non) applicability of TL dating techniques using the conventional method as described in Ref³². Figure 7B shows the TL emission before (red line) and after laser-driven proton irradiation (blue line). Our artifact would now be dated with an age of 140000 years instead of 324. However, conventional PIXE methods also invalid the use of this dating mechanism. Therefore, there is no difference in using laser-driven or conventional PIXE from the point of view of the feasibility of TL analysis.

We can conclude saying that the irradiation of the samples, even the most fragile ones such as ceramic, does not induce irreversible damage on the artifacts. Therefore, the *one shot PIXE* method can be used as diagnostic safely.

Once assessed the suitability of this distance in order to cause any damage to the samples, we now test the proton induced X-ray emission.

The PIXE produced by the laser-generated protons is measured at an angle of 10° from the sample, using a spectrometer that is sensitive to X-ray emission ranging from few keV to 50 keV³². As a detection medium, the spectrometer we implemented uses IPs of the type BAS-TR2025, which were readout by the same IP scanner as for the proton diagnostic (as discussed before in the description of the experimental setup). Behind the artifacts we placed a stack of RCFs (of the type HD) in order to verify the trajectory of the proton beam onto the artifact. Due to the limited sensibility range of the spectrometer, we tested the validity of our method only on the silver sample, since all the other materials that we tested for potential damaging by the proton beam, have their K lines outside the main detectable spectral range of the spectrometer. The results of a single-shot PIXE analysis performed on silver are shown in Figure 8. As it is visible from the RCF positioned behind the sample (see 8A), the silver target is fully covered by the impinging proton beam, i.e. the protons irradiate a surface of several cm^2 . The signal on the IP of the PIXE spectrometer (see inset in 8, 8B) shows three well-defined bands corresponding energy of the X-ray emitted from the material sample. The energy has been evaluated using the Bragg law:

$$\lambda = 2d \sin \frac{\theta}{2} \quad (1)$$

$$E = \frac{hcR}{2dx} \quad (2)$$

Where, λ and E are the wavelength and the energy of the X-ray, θ the diffraction angle, x the distance of the line from the zero-order, d is the lattice parameter of the crystal (in our case 0.68 nm), R is the distance the IP and the crystal in the spectrometer (in our case 0.1 m).

The convoluted spectrum (Gaussian convolution, obtained using the cross sections for each line³³) is shown, in Figure 8C (the amplitude of the lines is normalized to the typical X-ray emission efficiency of the different elements that are present in the artifact). The leftmost line, close to the zero-order (the intense round dot), corresponds to the first order K-alpha line (22.2 keV) while the two adjacent lines on the right side can be K-beta lines of Ti and Cr respectively (4.93 and 5.94 keV). The *one-shot* PIXE data are in perfect agreement with those obtained by conventional XRF on the same sample (inset in Figure 8C), which indicate the presence of the L-alpha line of Silver (about 3 keV) and K-beta lines of Ti (4.93 keV), Cr (5.94 keV), and Cu (8.97 KeV).

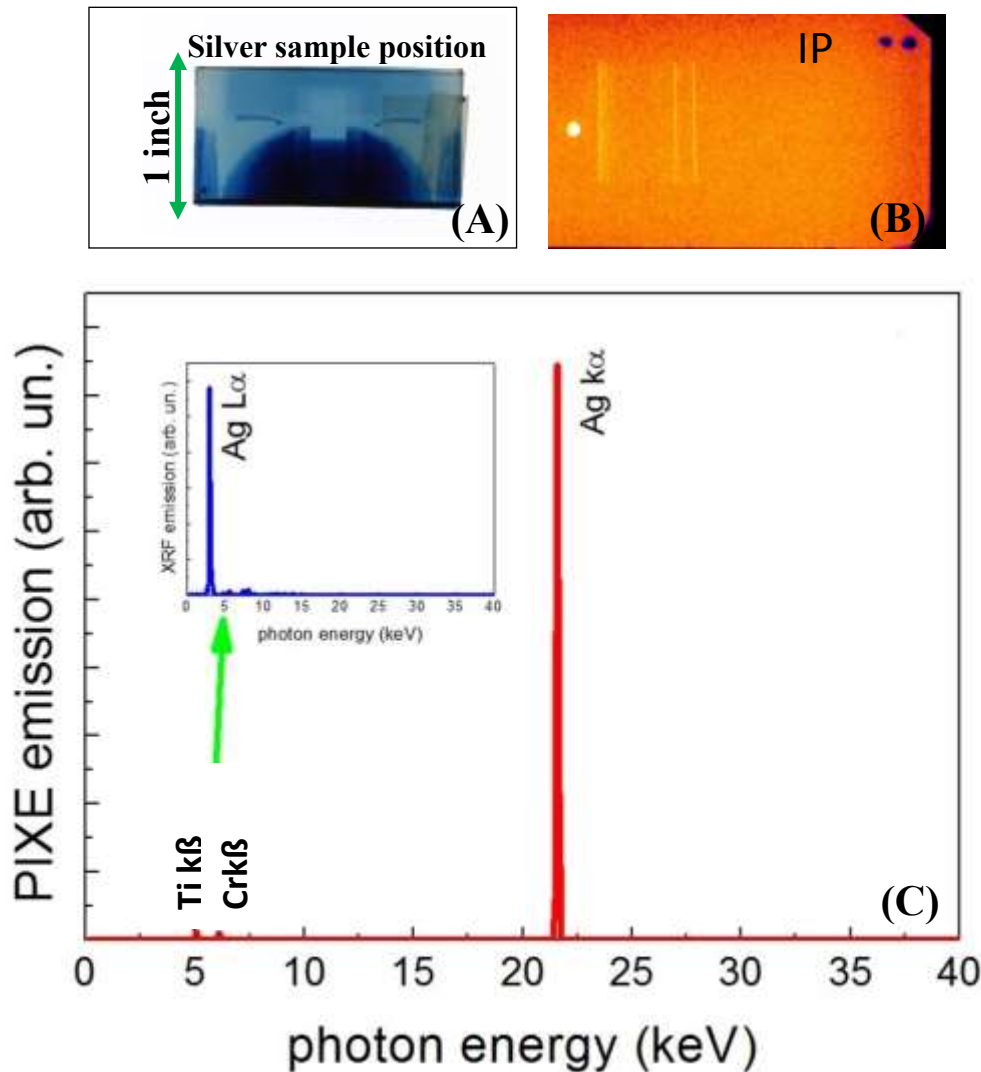


Figure 8 - (A) Silver sample mounted in front of the RCF (shown below) indicating the footprint of the laser-generated proton beam; (B) Image Plate (IP) positioned behind the X-ray spectrometer showing the different lines and the zero-order; (C) Convolved PIXE spectrum obtained by Bragg analysis on the IP shown in (B)

These results confirm the feasibility of laser-driven PIXE, which can be performed on a larger surface than what performed conventionally, in addition to being obtained in a single sub-ns laser shot. We have performed the experimental validation using laser-generated protons obtained on the TITAN laser, which probably is not the most suitable laser to routinely perform this kind of analysis. More appropriate lasers for making ensuring a broader use of this application are those commercially available and having a higher repetition rate^{25,26}. In those facilities, the integrated number of protons is typically at least one order of magnitude lower than what is obtainable with the TITAN laser (see Figure 3). However, the lack of proton flux

can easily be balanced by cumulating a certain number of shots, and with this reproducing the same X-ray signal as obtained during one single shot on the TITAN laser.

A proton flux deficit ratio of 100 in a 10 Hz (an example could be the red spectrum shows in the Figure 3 obtained with 150 TW laser Draco- Dresden laser acceleration source) laser can be balanced with 100 consecutive shots, ideally lasting 10 s in a high-repetition rate target setup. Given the lower proton flux, the temperature conditions (i.e. that the samples stays safely below melting point) are still ensured. Even when using higher-repetition rate lasers, the time interval between two consecutive shots is sufficiently long to ensure that the temperature within the sample cools down and the cumulative effect of the shots does not cause any damages to the artifact even at higher repetition rate operation.

A last point to consider is the more punctual analysis on different layers (depths) within the material. This analysis is necessary if the sample exhibits zones requiring further (more precise) investigation (e.g. harmful elements). A potential way to perform this is using an energy selector, i.e., a device that only selects a fraction of the proton beam within the entire broad-band spectrum around a tunable central energy and reduces the energy-spread of the particles^{32,33}. Since protons deposit most of their energy at the end of their trajectory (Bragg peak), this device allows to perform the analysis on different layers with a depth precision depending on the allowed energy spread. An additional advantage is that this kind of “laser-plasma” energy selector can easily and rapidly change its central energy: the main element for the energy selection is a movable slit, which selects the central energy out of the broad-band proton spectrum and that can potentially be moved with within a few seconds. Therefore, this allows a quicker scan than what obtained using conventional accelerators, where each central energy adjustment requires a full reassessment of the accelerator.

In the present study, we have not considered other materials of interest for Cultural Heritage such as glasses (and silicates in general), wood, paper, and one of the most commonly used pigments, the “Realgar” (Arsenic Sulfide As_4S_4), because the available experimental setup did not allow us to do otherwise. For analyzing those materials with the PIXE spectroscopy, the best approach is to test them in air, requiring a more sophisticated setup, which we did not have at disposal. This will be part of future studies.

4.2 Design of nanostructured targets: enhanced proton beams for *one-shot PIXE*

As indicated in the last section, one of the improvements of the *one-shot PIXE* could be the use of a magnetic energy selector, which allows to obtain monochromatic beams and then a PIXE analysis limited to a specific material layer. It is unlikely for the currently used magnetic selectors to strongly reduce the particle number (about 100 times), preventing the possibility to have a good sensibility in *one shot PIXE*.

Nevertheless, many theoretical works indicate that the use of properly designed micro structured targets in the laser-matter interaction could allow the tuning of the produced proton spectrum features in terms of an higher proton number in a well-defined energy range.

On the other hand, the improvement of proton spectra in a specific energy range combined by a simple magnetic energy selector, which cuts the particles outside the desired range, can produce monochromatic beams with a proton number comparable with that of whole energy range (0-40 MeV) proton beams.

In the following paragraph, the design and the realization of nanostructured target, which enhances the proton beam in the range of 3-5 MeV, are described. The design of this type of nanostructured target is only the first step to enhance the laser absorption on the target. The idea is to collect all the energy data obtained from each nanostructured target in order to achieve the database that we could call “*energy/target database*”.

This study is only the first step, other targets are designing for materialize the “*energy/target database*” for one-shot PIXE.

4.2.1 Nanostructured Targets: a new route for enhancing laser-driven proton beam acceleration

Nanostructured surfaces have attracted great attention because of their excellent antireflection and light trapping effects. Patterning a smooth surface with nano-pores or nanostructures has shown to reduce the surface reflection and hence to substantially increase the optical absorption in the visible range^{34,35,36}. Research on high absorption nanostructured materials is of crucial interest in many fields of material science since improvements on the material have a direct consequence on their applications. Therefore, in the last decades, strong effort has been put in the realization of nanostructured surface by superposition of a

nanostructured layer onto a bulk surface or by the use of RX lithography^{37,38}. Many of these methods require very long and expensive processes without allowing a good control in the shape or dimensions of the realized nano-pattern. These properties of nanostructured materials are important for many applications such as optoelectronics, photocatalysis, green energy³⁹, where an enhanced absorption results in increasing the device's performance and the overall operating efficiency.

A more recent research field, where improved light-absorption plays a crucial role, is the laser-matter interaction for high-intensity lasers, in particular the field of laser-driven proton acceleration. One of the most common proton acceleration mechanism, obtained on typical commercially available multi-hundred TW laser systems is the so-called Target-Normal-Sheath Acceleration (TNSA)⁴⁰ in which protons are accelerated at the rear target surface of a solid foil (target) irradiated by a high-intensity ($I > 10^{18}$ W/cm²), short pulse ($t < 1$ ps), laser operating at wavelengths around 800-1056 nm. Improving the acceleration mechanism, i.e. enhancing parameters such as maximum proton energy, laminarity, efficiency, monochromaticity, and number of accelerated particles, is one of the key challenges on which researcher are currently working. In particular, the laser-to-target absorption, i.e. how much energy is transferred from the laser to the target and from there to the particles, is a crucial parameter since it allows to improve the acceleration mechanism efficiency.

Currently this efficiency is at most in the order of a few percent and depends on the target and its structure. Several attempts have been made to use low-density foam, or micro- or nano- structured targets with the aim of improving the laser-to-target absorption⁴¹. These targets optimize the mean energy, collimation, and number of energetic ("hot") electrons that are generated at the target front by the ponderomotive force, travel through the target bulk and establish at its rear surface the electrostatic field that drives the proton acceleration process⁴². Therefore, the research on laser driven proton acceleration using solid targets also focuses on the production of targets with morphological and chemical characteristics, which can increase the optical absorption, enhancing the physical properties (electrical conductivity, mechanical resistance, thermal stability) and improving the driving electrostatic field at the target rear surface³⁵.

In this scenario, several groups^{36,44,45,46} demonstrated that the use of nanostructured targets could enhance the absorption of the laser pulse. In the following, we present nanostructured layer-targets able to increase the light absorption at least three times more than what can be achieved with a classical plain aluminum (non-nanostructured) target. We show that this absorption enhancement is very favorable for being applied in the laser-driven proton

acceleration mechanism and in particular for enhancing the lower-energy proton yield. Compared to existing nanostructured targets, requiring the use of complex and expensive manufacturing procedures (e.g. lithographic methods), our targets present the advantage of being both, simple and cheap to manufacture, and do not exhibit the stringent laser-matter alignment conditions, as required by micro structured targets.

4.2.2 Nanostructured target preparation: a simple, low cost, laser-based method

The nanostructured target is obtained growing a gold nanoparticle film (nanoparticles with a radius of $R \sim 5$ nm adjacent to each other) or Mylar, Carbon Nanotube buckypaper on different solid target surfaces such as aluminum (Al). We considered these target materials since they are the most used target materials in laser-driven proton acceleration and the wetting properties between them and the gold nanoparticles can ensure the realization of a uniform nanostructured film on the surface without local aggregation of nano-particles (NP)⁴³. With our technique, we are able to generate targets having, at the same time, a high absorption, high roughness and low cost. The low fabrication costs of all nanostructured films derives from a simple process combination of Laser Ablation in solution and Spray-Dry, which enhances the surface roughness.

The gold nanoparticles (NPs) are grown by the laser ablation in solution (LASiS) method. A gold plate, with nominal purity greater than 99% (commercially available from Goodfellow) and dimensions of 1 cm x 1 cm, is placed on the bottom of a vessel cuvette containing an aqueous solution of acetone (99, 7%). The plate is ablated with the first harmonic (1064 nm, 20 Hz) of a pulsed YAG:LASER (7100 series of QUANTA SYSTEM). The laser spot covered the entire target surface with a fluence of 500 mJ/pulse. The growth process is monitored by measuring the solution's optical absorption. The analysis of optical absorption and related extinction cross section (as you can see in the Figure 9A) is a useful technique to have rapidly information on the size of a nanoparticle. The extinction cross section of a particle is strictly dependent on its dimensions since the position of the plasmonic peak changes with the particle diameter.

As you can see in the Figure 10 the laser source for LASiS reached the target from the top surface of the cuvette while the white lamp (Energetiq LDLS, Laser Driven Light Source)

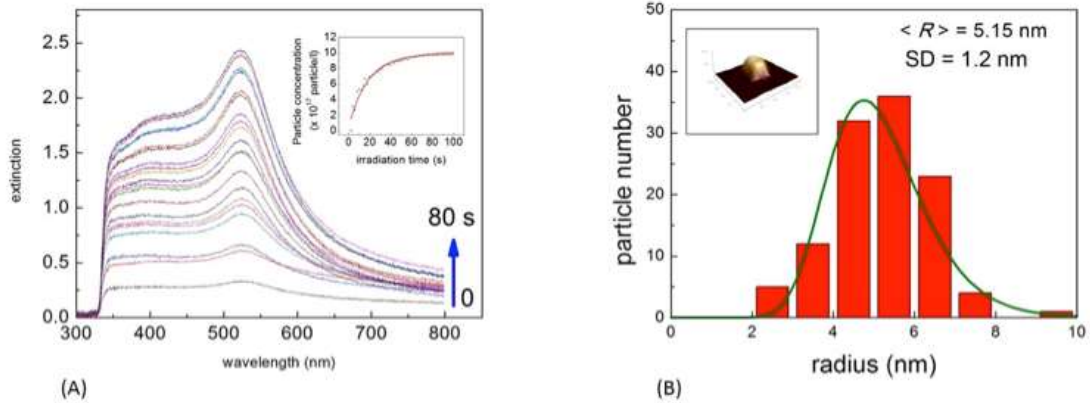


Figure 9 - (A) Extinction spectra of a colloidal solution collected at regular intervals of 4 s during the laser irradiation; (Inset A) Evolution of the particle concentration for primary particles produced during the laser ablation as function of the irradiation time; (B) Histogram of the particles radius distribution; (Inset B) 3D AFM images of Au NPs deposited on a SiO₂ surface

absorption measurements were placed normally to the electron beam, to illuminate the entire liquid region occupied by the plasma plume. White source and optical transmission is transferred between the sample and the equipment with a series of optical lenses and fibers. All the software for the optical absorption analysis have been prepared and tested. During the LASiS the droplets of the colloidal solution are deposited, at different irradiation times, on the silicon dioxide substrate for ex-situ diagnostics (i.e., AFM, SEM, microscopy, and EDX analysis)⁴³.

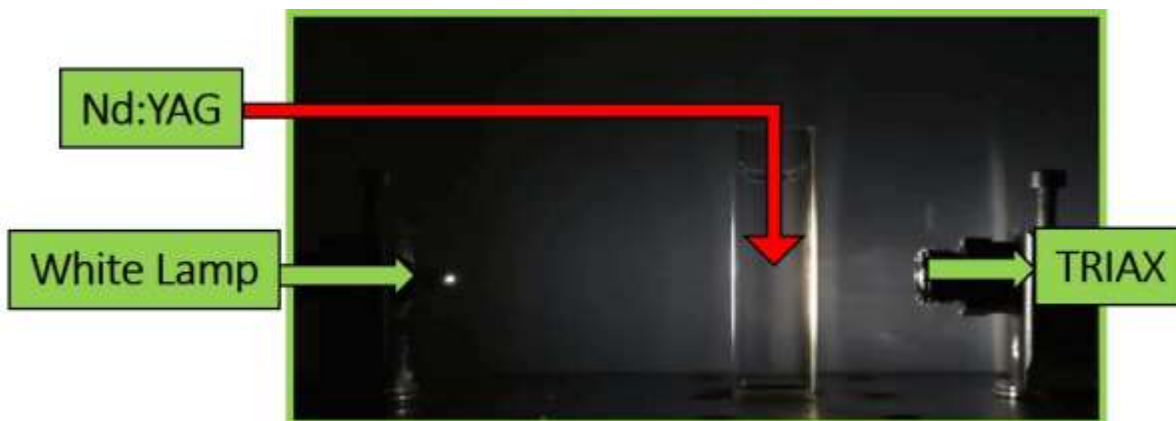


Figure 10 – Sketch of LASiS setup

Nano structuration on the target surface is obtained by a controlled spray-dry process. The solution is sprayed using an airbrush working in “fine line spray” mode and holding it at about 500 μm from the working surface. Different amounts of gold NPs coming from the solution are deposited on a surface of 1 cm² onto three different surfaces: Aluminum foil (purity greater than 99%, thickness of 25 μm), Mylar foil (thickness of 2,5 μm), and Multiwalled Carbon Nanotube (MWCNT) buckypaper (nominal purity 95%, thickness of 30 μm). All the surfaces are heated in Ultra High Vacuum condition before performing the NP deposition in order to remove the adsorbed impurities.

Chemical and morphological analysis on cleaned surfaces do not show presence of external impurities or oxide, which could react with Au NPs, influencing the characterization of the nanostructured materials. After the deposition, each nanostructured material is characterized for retrieving the morphological, chemical and optical properties. Morphological information (i.e.; particle shape, dimensions, density and roughness) of the nanoparticles and the nanostructured surfaces is directly obtained by AFM and SEM microscopies.

The AFM images are obtained by the ICON AFM microscope from Bruker working in tapping mode. Each image was taken with a resolution of 512 x 512 pixels and a frequency of 1 Hz. The dimensions of the NPs are analyzed conducting a statistical analysis on several nanoparticles collected by different AFM images. For each sample, we scanned several areas (about 50) in windows of 500 nm x 500 nm (resolution of 1024 x 1024 pixels).

The images are elaborated by the Nanoscope software (1.40 version from Bruker) to obtain morphological information and measure its dimensions. The morphology and topography of nanostructured materials is investigated in terms of roughness and fractal dimensions. The roughness of nano-nanostructured surface is obtained directly using Nanoscope software, while the fractal dimension for each substrate was evaluated as:

$$D_f = \frac{(8 - \beta)}{2} \quad (3)$$

where β is the slope of the 2D power spectral density (PSD) calculated in a log plot 2D PSD was estimated by a FACA ((fractal analysis by circular averaging))-based approach.

Finally, the chemical composition of the NP and the nanostructured surface is analyzed by Energy Dispersive X-ray (EDX) spectroscopy, taken under SEM conditions, and X-ray

photoelectron spectroscopy (XPS). XPS measurements are conducted in a Ultra-High-Vacuum chamber equipped for standard surface analysis with a pressure in the range of 10^{-9} torr.

The absorption of the particle films is taken by an Olympus microscope (Horiba-Jobin Yvon) mounting objectives of 10X, 50X and 100X magnifications. The microscope is equipped with a white lamp (Energetiq LDLS, Laser Driven Light Source), and a Triax 320 (Horiba-Jobin–Yvon) spectrometer working in the 200-1500 nm range.

4.2.3 The Gold nanostructured target: morphological, chemical, and optical properties

As already shown in the Figure 9A, a collection of extinction cross-sections was taken during the laser irradiation, at regular intervals of 4 s. It is clearly visible that the position of the plasmonic oscillations do not change during the laser irradiation, while the extinction shape is regular in the first 25-30 s of the irradiation and changes for longer irradiation times.

In particular, one can observe that for longer irradiation times the spectra become broader with a widening for wavelengths greater than 500 nm. The comparison with a calculated extinction (following the Mie-Gans theory⁴⁴), indicate the formation of Au NPs with a radius of about 5 nm in the first 30 s of the irradiation and the formation of a bigger aggregate (with radius ranging from for 10 to 20 nm) for longer irradiation times.

These results are confirmed by morphological studies conducted on colloidal droplets deposited on a SiO₂ surface for a laser ablation time of 15 s (Inset in Figure 9A). The AFM images (see Figure 11B) show the presence of many randomly distributed and well-isolated particles on the surface. A radius distribution histogram, obtained from a Bearing analysis on the AFM images, is shown in Figure 9B for a set of more than 200 nanoparticles.

The data can be fitted with a LogNorm distribution, obtaining a mean radius of $\langle R \rangle = 5.15$ nm and a standard deviation of $SD = 1.2$ nm. The absence of clusters in the AFM images and the relatively low SD clearly indicates that the deposited NPs are the primary particles produced directly by the laser impact on the metal target without secondary processes of self-aggregation in the solution. Analysis of the evolution time of the primary particle concentration, performed using the Lambert and Beer's law on the first plasmonic peak, indicates that the concentration of smaller particles linearly increases until 20-30 s and then reaches a saturation value of 10^{18} particles/l (Inset in Figure 9A).

EDX spectra for a single NP (see Figure 11A), taken under SEM conditions, show only the band of gold, with negligible signs of oxygen or external impurities, indicating the

formation of pure nanoparticles without any growth of oxides or radicals due to the crack of solvent molecules during the irradiation.

For the growth of the nanostructured films, we selected the NPs obtained after an irradiation time of 15 s. At this irradiation time, we are confident of selecting only the primary particles produced by the laser ablation, thus excluding big and amorphous NP clusters, which aggregate for longer times. AFM images (Figure 11B) show the deposition of a uniform film of Au NPs on all surfaces when depositing the NPs on a layer using the Spray-Dry method. The surface roughness increases with particle density on the surface (see Table 1 for the case of gold nanoparticles on aluminum substrate (Au NP/Al)) and reaches a deposition saturation value of about 10 nm for 5×10^{14} particles/cm², indicating the formation of a monolayer of NPs on the target surface.

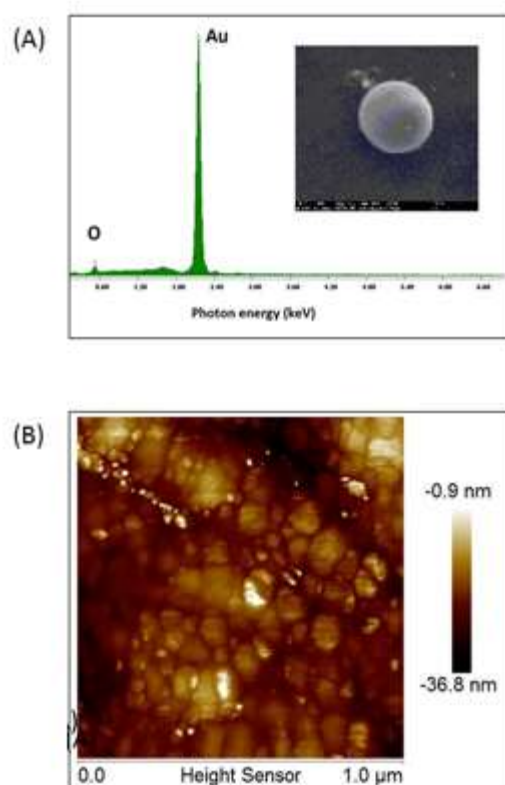


Figure 11 - (A) SEM image of Au NPs deposited on a Silicon substrate and EDX analysis on a NP; (B) AFM Image of a Nanostructured Film on aluminum (Au NP/Al)

Table 1: Roughness properties of the nanostructured target obtained using different Au NP densities

<i>Density ($\times 10^{14}$ particles/cm²)</i>	<i>Roughness (nm)</i>
0	1.48
1	4.10
5	8.99
10	11.8
20	11.9

The morphological properties of the nanostructured materials are strongly different from those of a pure surface (see Table 2). The fractal dimension D_f shows values greater than those of a pure surface, while the roughness increases of about two times for all nanostructured surfaces, clearly indicating the growth of a smoother topography⁴⁵. This can favor the absorption of the laser irradiation during TNSA experiments, enhancing the generation of laser-driven proton beams.

XPS measurements on our NP films indicate an increased presence of gold on the film surface (88%) and only a little amount of C and O (5% and 7% respectively), which can be attributed to atmosphere absorption during the analysis processes. The gold 4f line is centered at 84 eV, without chemical shifts, indicating the formation of chemical bonds⁴⁶ between NPs and substrate and showing the physisorption nature of the grown film.

Table 2: Morphological properties of the pure and nanostructured surfaces

	<i>Roughness (nm)</i>	<i>Fractal dimension</i>
<i>Pure MWCNT</i>	62	2.88
<i>Au/MWCNT</i>	120	3.03
<i>Pure Mylar</i>	7.66	2.03
<i>Au/Mylar</i>	17.2	2.16
<i>Pure Al</i>	8.15	2.01
<i>Au/Al</i>	19.3	2.13

Finally, we compare UV-VIS-NIR (see Figure 12C) optical absorption for the uncoated and nanostructured coated surfaces. The optical absorption of nanostructured materials is very different from these of pure surface (Figure 12C: Au/Al, Au/Mylar, Au/MWCNT respectively). Considering the dependence of the NP concentration on the absorption, we see that for the coated surface the optical absorption increases in the entire VIS region, reaching a saturation value for NP concentrations of about 20×10^{14} particles/cm², we therefore will take this concentration as baseline for our measurements. As seen in Figure 12C, the optical absorption of the coated materials is higher in the spectral region ranging from ca. 450 to 1200 nm and for all different substrates.

In particular, the Au NP/Al coated material shows the best results among all considered substrates. For the region of interest of most high-power lasers operating at fundamental frequency 1ω between 800-1000 nm (and 2ω between 400-500 nm) we find a very strong enhancement of the absorption. For the region between 800 and 1000 nm the improvement is ~30% while for the region around 600 nm our material almost triplicate the absorption. The optical absorption of nanostructured materials is characterized by a broad structure, which covers all the visible range, with five absorption peaks at 485, 574, 635, 691, and 776 nm (see Figure 12C).

The same structure has been observed in many other works⁴⁷ using a substrate composed by noble metal nanoparticles or nanoclusters randomly disposed on a layer and can be associated to the absorption and scattering in the nanoparticles network. In particular, the spectral absorption around 550 nm corresponds to the plasmonic resonance of gold nanoparticles with a radius of about 5 nm.

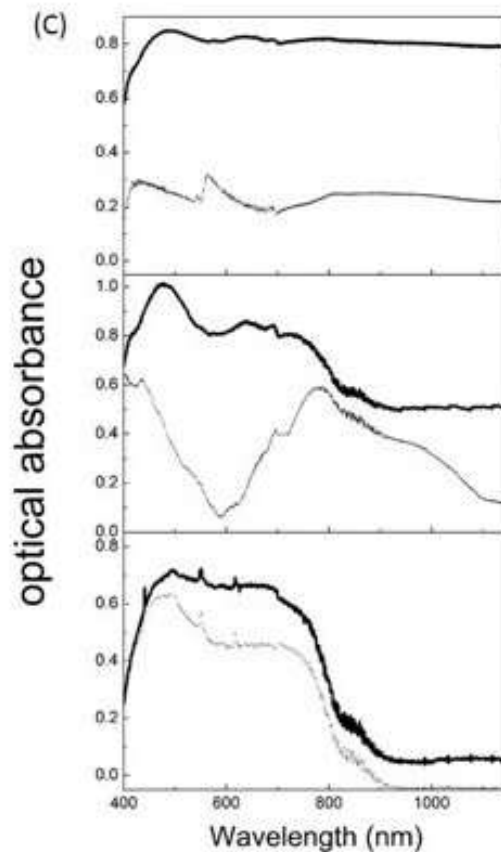


Figure 12 - Optical absorption in VIS and IR ranges for Au NPs structured films (solid lines) and pure substrates (dot lines), from the top to the bottom: aluminum, Mylar, and CNT substrates

The broadband absorption structure visible at about 650 nm can be justified as a superposition of the absorption of Au NPs centered at about 670 nm, the aluminum substrate one at 680 nm and the broad absorption of the aluminum bulk in the red spectral region.

The enhancement of absorption in all visible range can ensure the improvement of Laser adsorption and, then, of particle production in TNSA experiments.

4.2.4 Nanostructured target: the experiment at LLNL facility

As for the case of *one shot-PIXE* we tested the nanostructured targets experimentally using TITAN laser facility located at the Lawrence Livermore National Laboratory (LLNL), Livermore (USA). The TITAN laser has an energy of about 220 J, pulse duration of $\tau=700$ fs, wavelength $\lambda=1.054$ μm , 8-9 μm focal spot diameter (FWHM), producing an intensity of

about $I \sim 5 \times 10^{19}$ W/cm. The laser is used for interacting with the target in order to accelerate protons in the laser-forward direction using the TNSA⁴⁰ mechanism.

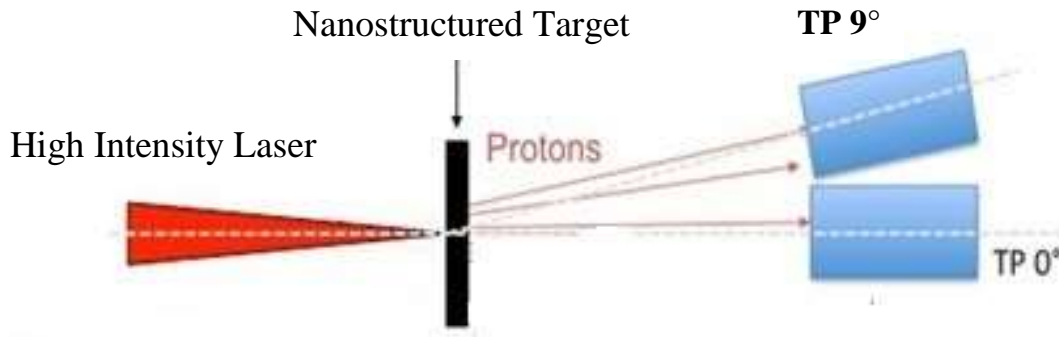


Figure 13 - Experimental setup used for nanostructured target tests

The Amplified Spontaneous Emission (ASE), which delivers ~ 10 mJ in energy, has been estimated to be $< 10^{-6}$ in contrast with respect to the main laser pulse. As targets for the proton generation we use the produced Au NP/Al target and, as comparison, a pure Al 15 micron target. For detecting the proton beam, we use two calibrated Thomson parabolas (TPs) and spectrometers, located at 0° (TP 0°) and 9° (TP 9°) with respect to the main pulse laser axis (Figure 13) to measure the forward generated proton spectrum. Proton spectra measured by the TPs were readout in an absolute manner^{48,49} using Image Plates (BAS-TR 2025 from Fuji Photo Film Co. Ltd) analyzed using a FUJIFILM FLA-7000 reader.

Additional measurements of the proton spectra are obtained using Radio Chromic Films (RCFs) of the type MD that allowed having a spatial distribution of the beam. On most shots, the target was placed occupying only half of the proton beam so that the TP could readout the spectrum using the other half of the proton beam (see Figure 8).

Finally, we measure the laser absorption on target surface. The reflection and transmission of laser from surface are measured by an Ocean optical spectrometer working in the range 200-1200 nm. The absorption is then evaluated using the classical equation:

$$a(\lambda) = 1 - t(\lambda) - r(\lambda) \quad (4)$$

Where $a(\lambda)$, $t(\lambda)$, and $r(\lambda)$ are, respectively, the laser absorption, transmission and the reflection at laser wavelength.

The results of the absorption obtained from the comparison between the classical Aluminum target and the Au NP on Aluminum target clearly indicate an improvement, in terms of laser absorption. In fact, as you can see in the Figure 14 the improvement of laser absorption is of a factor 4: from 0.2 of Al target to 0.8 of Au NP/Al target.

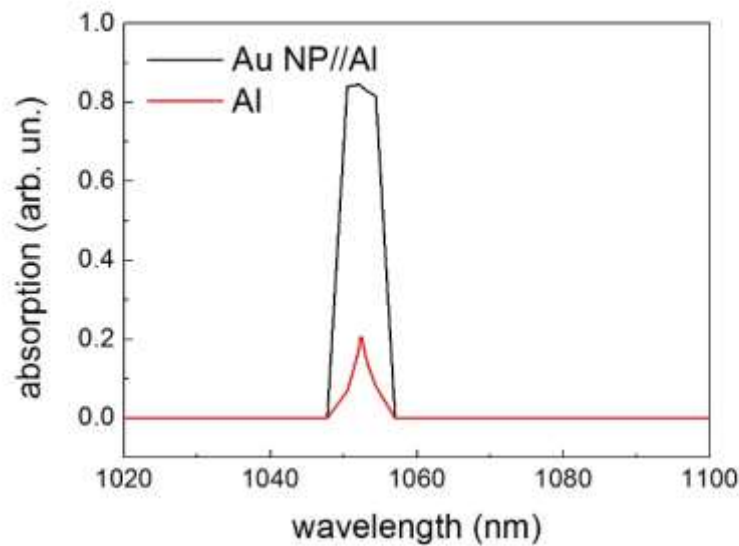


Figure 14 - Laser absorption from Al (red curve) and Au NP/Al target (black curve)

Figure 15 shows the comparison between the accelerated proton spectra, using the two targets: Al and Au NP/Al. The use of nanostructured targets leads to an improvement in terms of accelerated proton number, as can be observed from the reported spectra. We amplify the peak of the proton spectrum at 3 MeV by a factor 2 for (the yield is increased from 0.8×10^{11} protons/MeV/sr in the case of pristine Al to 1.6×10^{11} protons/MeV/sr in the case of a Au NP/Al target). Moreover, in the entire energy range between 2 and 6 MeV, a global enhancement of the proton flux can be observed.

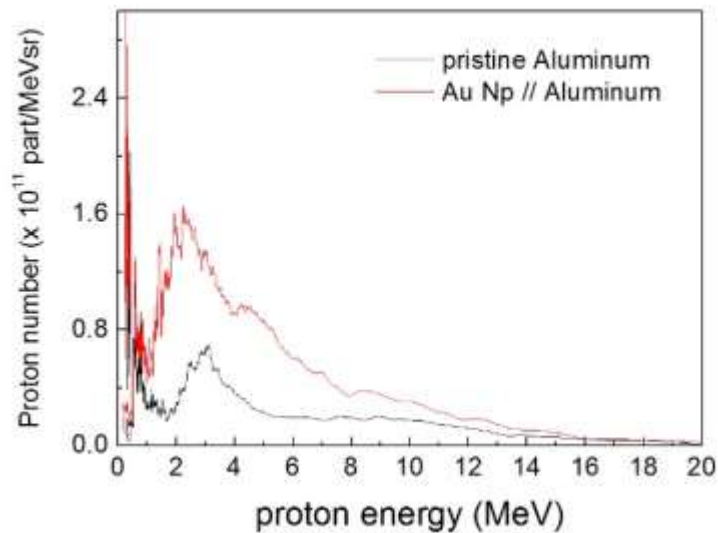


Figure 15 - Proton spectrum obtained from a pristine Al target (red curve) and from an Au NP/Al nanostructured target (black curve)

4.3 Plasma Induced Luminescence in air: a new diagnostic method based on laser-plasma interaction

133

The following section introduces the second diagnostic method based on laser-plasma physics developed in the framework of this thesis. The method can be applied to many analyses in material science and it is particularly suitable for the analysis of large artworks, which cannot be moved from the museum sites or inserted in a vacuum chamber. This is achieved by interaction of a focused high-energy laser with air, producing a sub-millimetric plasma. The energetic electrons generated and accelerated in the plasma at energies higher than 5 keV reach the target surface of the sample to be analyzed, causing luminescence emission and plasmonic resonance.

Each material is characterized by different chemical and optical properties that can be determined with the above-mentioned techniques. As such, our method allows to obtain an exact analysis of the samples, covering surfaces in the range of cm^2 , in only a few minutes. We demonstrate this by showing that the acquired information is identical to what obtained with more sophisticated methods, such as SEM-Cathodoluminescence and Photoluminescence.

4.3.1 Plasma-Luminescence in the framework of Luminescence spectroscopies

As indicated in Chapter 2, luminescence methods (cathodoluminescence, photoluminescence, and ionoluminescence)^{50,51,52,53} assume particular relevance in different scientific fields (from mineralogy to semiconductor physics to nanotechnology) for their ability to identify the chemical composition of materials with a resolution of a few ppm and the individuation of plasmonic resonances. Luminescent materials are mostly solid inorganic materials consisting of a host lattice with impurities. The impurity concentrations generally are low in view of the fact that at higher concentrations the efficiency of the luminescence process usually decreases (concentration quenching). The energy absorption, used to excite the luminescence, takes place by either the host lattice or by impurities. In most cases, the emission takes place on the impurity ions, which, when they generate also the desired emission, are called activator ions.

The luminescence emission can be induced in different ways (i.e. high energetic electron or ion irradiation, heating in temperature range between 300 and 600 °C, or by UV laser irradiation). While photoluminescence can be taken in air in simple UV laser setups, most complicated methods as cathodo- or iono-luminescence need to more complicated setup under SEM and Vacuum conditions. Nevertheless, these latter methods are crucial to distinguish structures as plasmon emission in metals or in nanostructured materials.

The aim of this thesis section is to introduce a new method in laser-dedicated setup for obtaining an in-air complete chemical analysis of the materials surface and its bulk (within a depth of about 2 µm from the surface) based on the study of luminescence emission induced by the plasma radiation (*Plasma-Induced Luminescence PIL*). Plasma induced luminescence event is ascribed to the interaction between the electrons produced and accelerated around the plasma (laser - air interaction) and the material. The idea is to use the beta radiation produced in the laser-plasma interaction to generate cathode-luminescence and plasmonic emission and then, from there, to obtain the chemical composition of materials.

We test the method on three different materials with diverse density and chemical properties (Gold, Aluminum Oxide, and Marble) to explore the effectiveness of the method on metals (Gold), insulators (Aluminum Oxide), and minerals (marble). We demonstrate that our method reveals the plasmonic emission from metals as well as the intrinsic luminescence of oxide or the emission induced by impurities in minerals. In addition, while conventional luminescence techniques are able to characterize surface areas in the order of a few microns

(invested area from laser, electron, or ion beams), *Plasma-Induced Luminescence* is able to analyze a surface area in the order of cm^2 in only a few minutes.

4.3.2 Design of the experimental setup at the ALLS facility

A sketch of the experimental setup is illustrated in Figure 16A and B. The air plasma is generated by interaction of a strongly focused down high-energy laser with air. The Advanced Laser Light Source (ALLS) few-cycle infrared (IR) beamline is used to obtain the air plasma. The source provides a 3 mJ, 15 fs pulse, centered at $1.8 \mu\text{m}$ with a repetition rate of 100 Hz. The energy stability of the pulse is approximately 2.5% rms⁵⁴. The experimental setup, shown in Figure 16 A and B, consists of a series of transport optics, an on-axis parabola, a series of imaging lines for the plasma analysis and luminescence collection.

The luminescence emission is stimulated by the portion of plasma radiation collected through a hole with a diameter of 5 mm drilled inside a mirror placed at a distance of 5 mm from the center of the plasma. The investigated area on the target surface can be modulated simply by changing dimension of the hole, allowing to analyze areas from a few μm^2 to cm^2 .

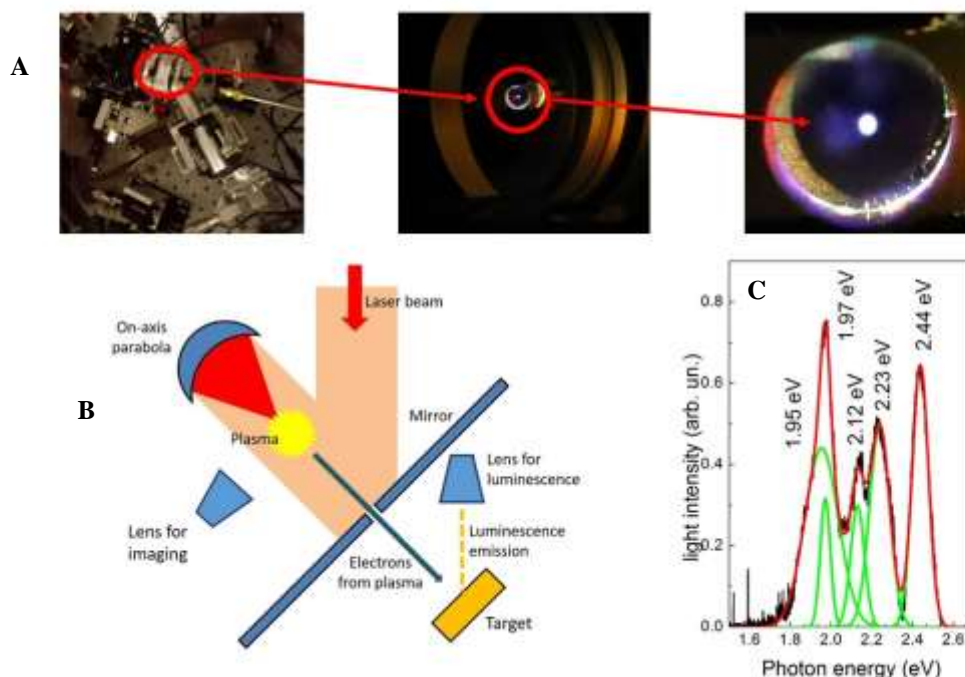


Figure 16 - (A) Experimental setup for air plasma generation and plasma images, (B) sketch of experimental setup for plasma-induced luminescence generation and analysis, (C) spectra of the photon emission obtained from the plasma. The emission is concentrated in the VIS-NIR region, excluding the possibility of photoluminescence generation from the target surface

Luminescence emission at an angle of 45° is collected by a lens positioned at 4.5 cm from the irradiated target (focal distance) and transferred through an optical fiber to a spectrometer working in the UV-VIS range (VIS-140 Horiba). Each luminescence spectrum is collected with an acquisition time of 120 s in order to allow for a sufficient signal/noise ratio.

All the experiments are conducted in darkness, in order to eliminate every possible background light source, which would add noise to the measurement. We irradiate three samples (Gold, Aluminum, and Marble), having a well-known luminescence emission stimulated by both photons and electrons. This allows a direct comparison of our results with those present in literature and from there to attribute the emitted luminescence to different components within the plasma radiation (all the data well compared with the luminescence data base (see Ref.⁵⁴ and reference therein).

4.3.3 Experimental results obtained at the ALLS facility

The plasma produced in the interaction between laser beam and air is visible in optical images in Figure 17. It shows a spheroidal shape with axes of 2 and 3 mm and a photon emission in the visible-NIR region with 5 lines at 1.5, 1.97, 2.12, 2.23, and 2.44 eV. The absence of UV lines in the plasma spectrum excludes the possibility of photoluminescence emission from the target.

Furthermore, a Faraday cup read a negative current of about 40 pA in all the regions around the plasma, until a distance of 20 cm from the plasma center, indicating the presence of electrons produced in the plasma and isotropically accelerated. The first evidence of air-plasma-induced luminescence is visible in Figure 17 where the image of plasma, through a slit, is taken on the surface of aluminum oxide powder - based scintillator. The green-red emission shows a spectrum (collected on a solid target of Al_2O_3) composed by 10 bands (summarized in Table 3 shown below) typical of Aluminum cathodoluminescence and plasmonic resonance. In particular, the 237, 333, 403, 507, 750, and 770 nm bands are attributed to CL emission from intrinsic defects (anion vacancies) from Al_2O_3 thin films on surfaces (⁵⁵and reference therein). All the lines in literature are observed only under CL-SEM, this indicate that they are induced by electrons with a minimum energy of about 20 keV⁵⁴. The 576, 540, and 670 bands are attributed to plasmonic resonance on aluminum, generated by electrons with a minimum energy of 5 keV⁵⁶.

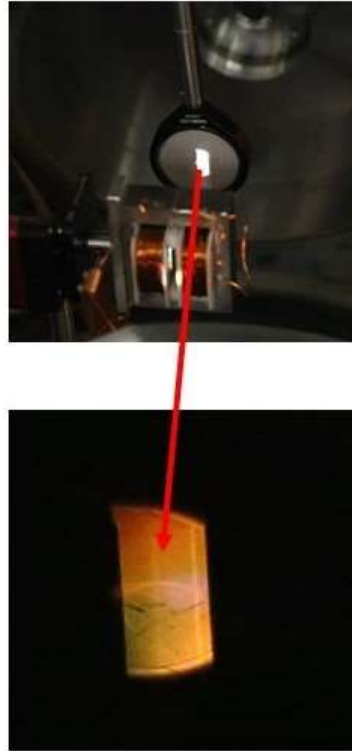


Figure 17 - Luminescence emission from Al_2O_3 powder scintillator

Table 3: Summary of plasma-induced luminescence bands

<i>Gold</i>	<i>Aluminum</i>	<i>Marble</i>
530 nm	237 nm	305 nm
599 nm	333 nm	337 nm
	403 nm	398 nm
	507 nm	519 nm
	576 nm	506 nm
	540 nm	577 nm
	670 nm	
	750 nm	
	770 nm	
	811 nm	

EDX spectra (see Figure 18A) of scintillator indicate the only presence of Al, O and C on surface confirming the assignation of luminescence bands. Similar results are obtained for all the analyzed materials.

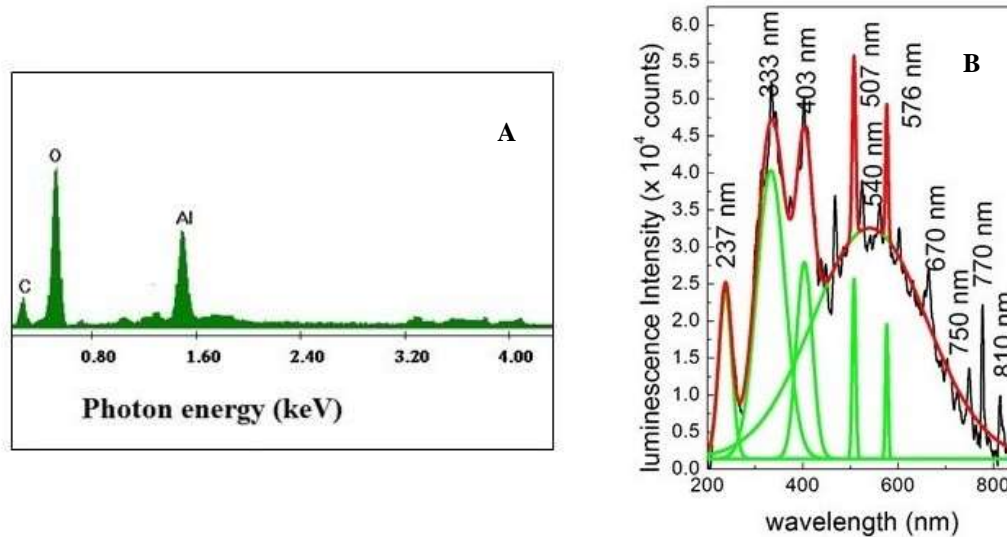


Figure 18 – (A) EDX analysis of chemical composition of scintillator; (B) Luminescence emission from Al₂O₃ powder scintillator spectrum

Luminescence of marble (Figure 19A) reveal six bands in the region 300-600 nm. All the bands can be attributed to CL-SEM (20 keV) emission from intrinsic defects (lattice vacancies) or to Mg²⁺ external impurities (the presence of Mg impurities was confirmed by EDX spectra in Figure 19B)⁵⁷. We can exclude the presence of photoluminescence emission because the absence of bands in the range from 600 to 700 nm⁵⁴. On the other hand, the plasma spectrum (as you can see in Figure 18B above) does not show photons in the UV region (> 3 eV). Luminescence emitted from the pure Gold target (Figure 19C for luminescence spectrum and 19D for EDX analysis) indicates the presence of two bands at 530 and 599 nm, both attributed to Gold Plasmon resonance induced by irradiation of 5 keV (minimum energy) // 30 keV electron beam⁵⁸. The probability of plasmon emission from gold (Plasmon 530 nm and considering electrons with energy between 5 and 30 keV), is about of 10⁻⁴ Photons for incident electron⁵⁶. The photon number calculated from luminescence spectra (collected in a time of 120 s) is of 2.5 x 10² photons/s at 530 nm, this indicates an electron incidence of 2.5 x 10⁸ electrons/s (about 40 pA), which is in perfect agreement with the current measured on the Faraday cup placed in the sample position. The exact correspondence between the measured electron current on sample surface and the photon rate/production clearly indicates that the

plasma-induced luminescence can be exclusively attributed to the electrons produced and accelerated by the plasma.

Concluding, in this thesis section we proved that it is possible to obtain a precise analysis of the material composition using a plasma, generated in air by a high intensity laser. In fact, the luminescence generated from the materials that were exposed to the plasma allows obtaining information about the chemical compositions of the sample. The data acquired with our technique are identical to those obtained with more sophisticated and complex methods, such as SEM cathodoluminescence and photoluminescence. Furthermore, we can assert that for all the materials which we have investigated, i.e. aluminum oxide, gold and marble, the laser-generated plasma is able to induce luminescence emission from structural defects and plasmon resonance. Concerning the surface area that can be analyzed with our technique, we have shown that we are able to reach, within 2 minutes of time, a large surface of investigated material, the order of tens of mm². Moreover, being the electron energy in the range between 5 and 30 keV, it is possible to reach a different penetration depth according to the material of the irradiated samples.

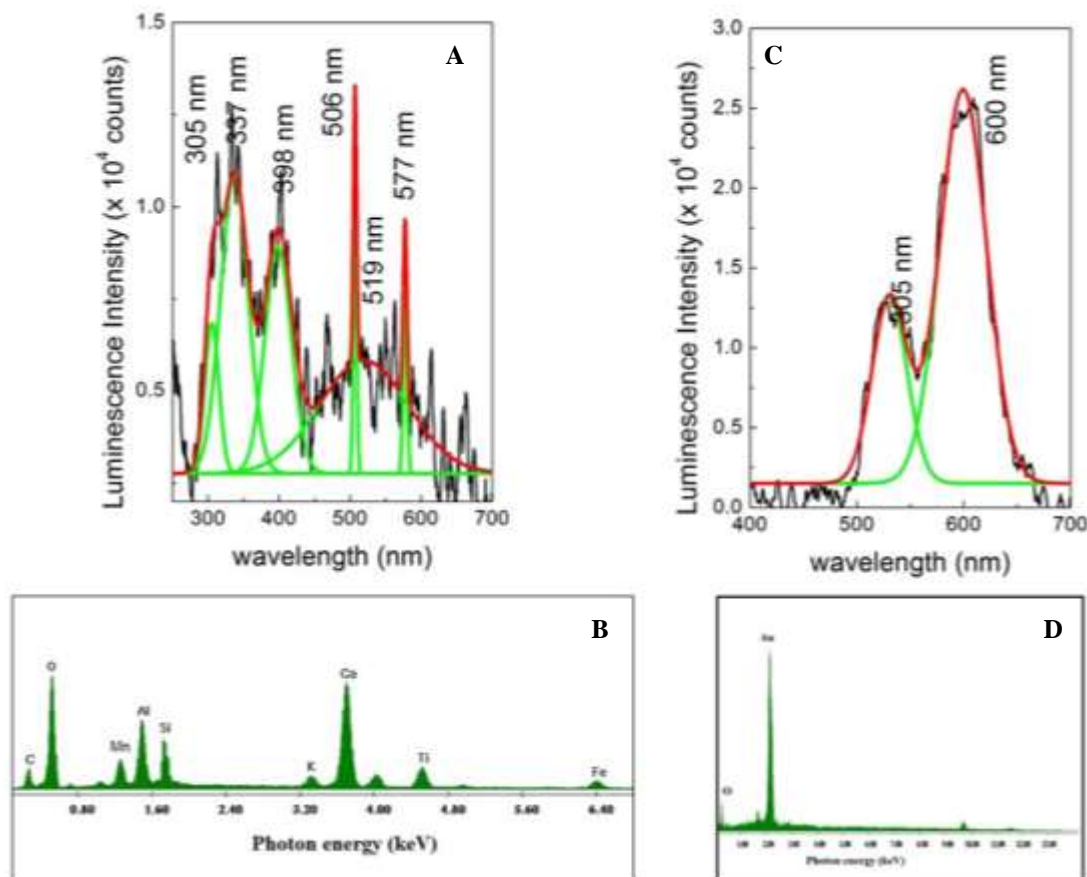


Figure 19 - Luminescence emission and chemical composition of marble (A and B) and gold target (C and D)

Chapter 5

5. General Conclusions and Future Perspectives

The ambitious goal of this Ph. D thesis is to improve both fields of Diagnostic and Conservation of Artistic and Cultural Heritage, applying the methods of both Laser-Plasma Physics and Nanoscience.

The detailed discussion of previous chapters clearly demonstrates the innovation of proposed techniques in comparison with conventional ones. During the project, new experimental setups were conceived, designed, and realized. New diagnostic methods, inspired to laser-plasma world, have been adapted and modulated for analysis of archeological finds and artwork, while nanomaterials and nanostructured films have been realized and applied to the conservation and restoration of artwork surfaces.

The main results of the presented work can be summarized as follows:

1. This thesis shows the effectiveness of nanomaterials as protective surfaces, testing the bactericidal effects of some nanomaterials. The materials have been combined by a hydrophobic matrix and deposited on the surface of materials of interest for Cultural Heritage. The work demonstrates the possibility to use nanomaterials in order to protect precious artworks and archeological finds, without changing their aesthetical or physical properties. The work tests the effectiveness of Titania nanoparticles and carbon-based nanomaterials (graphene and fullerenes) embedded in a Sylgard matrix. The realized protective films show good transparence properties with a transmittance around 95% for films having thicknesses of 200 nm. Biological tests, conducted against *Escherichia Coli*, indicate that the interaction between cells and nanomaterials creates an interface between the film surface and the external environment, preventing the penetration of bacteria into the material's bulk. Moreover, the combined action of hydrophobicity and nanomaterial's stress on the cell membrane strongly limits the bacteria proliferation, causing the destruction of the bacterial colonies after 4 hours of exposure and a complete death of all cells after 9 hours. Finally, biological tests after aging indicate the stability of our films in 25 freeze-thaw cycles.

2. This thesis introduces the first use of laser-generated proton beams as diagnostic for materials of interest in the domain of Cultural Heritage. Using laser-acceleration protons, as generated by interaction of a high-power short-pulse laser with a solid target, we are able to produce proton-induced X-ray and Gamma-ray emission spectroscopies (PIXE/PIGE). By correctly tuning the proton flux on the sample, we are able to perform the PIXE in a single shot, provoking less damage to the sample than conventional methodologies. In order to verify this feature, materials of interest in the Cultural Heritage field have been experimentally irradiated with laser-accelerated protons, thereby measuring the PIXE emission. The morphological and chemical analysis of the sample before and after irradiation are compared in order to assess the damage provoked to the artifact. Montecarlo simulations confirm that the temperature in the sample stays safely below the melting point. Compared to conventional diagnostic methodologies, laser-driven PIXE has the advantage of being potentially quicker and more efficient.
3. This work presents for the first time the realization of a series of different nanostructured targets, which enhance laser absorption and then the proton laser acceleration process. The nanostructures in the target have been realized with a method simpler and cheaper than conventional lithographic processes. The optical absorption of the nanostructure is broadband, and covers the entire visible region up to the infra-red. This absorption improvement is particularly interesting for different applications, such as the laser-driven proton acceleration and the TNSA accelerating process. Finally, PIC simulations confirm an improved accelerating process with an increase of up to 10% in proton number, an enhancement of 17% in the total absorbed laser energy and an increase of 32% in the electron energy density.
4. This thesis demonstrates that it is possible to generate luminescence from materials exposed to a laser generated air-plasma, obtaining a precise analysis of the material composition. The results related to the chemical composition of the materials obtained with our technique are identical to those of more complicated and complex methods such as SEM Cathodoluminescence, Photoluminescence, and analysis of plasmonic resonance. We

tested three different materials, Aluminum Oxide, Gold and Marble, confirming that for all materials Plasma-induced luminescence is able to induce luminescence emission from structural defects and plasmon resonance. Plasma-Induced Luminescence is attributed to the interactions between the electrons produced and accelerated around the plasma in the laser-air interaction and the sample material. Finally, if one estimates the electron energy between 5 and 30 keV, then is possible to investigate within 2 minutes a large surface in the order of tens of mm², with a penetration depth varying from 2 μm, for the Gold and Marble samples, up to 6 μm for the Aluminum Oxide sample.

5. This work introduces, for the first time, the use of the atomic force microscope (AFM) and of the pulsed laser ablation (PLA) as methods for morphological diagnostic with nanoscale precision of archeological artifacts and corrosive patina removal from stone artifacts extracted from the Church of Sotterra (located in Calabria, South Italy). The AFM microscopy was compared with different petrographic, chemical, optical and morphological analysis methods for identifying the textural characteristics, evaluating the state of preservation and formulating some hypotheses about the provenance and composition of the impurity patina located on the artifact surfaces. The results demonstrate that with the nanometric precision obtained with AFM microscopy, it is possible to distinguish the different states of preservation, much better than using conventional petrographic methods. The surface's roughness is evaluated from very small artifact's fragments, reducing the coring at micrometric scale with a minimal damage to the artworks. After the diagnosis, restoration tests have been performed, using the pulsed laser ablation method and compared with the more common micro-sandblasting under dry conditions. The work demonstrates that the PLA is highly effective for the removal of the surficial patina, with a control of a few hundreds of nanometers in the surface cleaning, without introducing chemical or morphological damages to the artifacts. Moreover, PLA can be easily implemented in underwater conditions; this has the great advantage that stone and pottery artifacts for marine archeological sites do not need to be removed from the site. Moreover, the work presents the study of laser ablation (LA) restoration techniques and of thermo-luminescence dating process (TL). The main aim of the work is to demonstrate that LA does not affect the possibility to date ceramic artifacts after restoration. We ablate

Neolithic ceramics in air with a laser YAG first harmonic (1064 nm), dating the artifacts before and after the cleaning process. The obtained discrepancy before and after the cleaning process, respectively, is of about 200 years (3300 B.C. and 3100 B.C.), value which is in below limits of experimental error. Moreover, the temperature of artifacts during the LA was monitored at the point of sampling for dating. The results indicated that the maximum temperature reached is about 100°C, not enough to empty the metastable traps that cause the luminescence signal.

The obtained results allow to project and design future works. Several experiments are already scheduled for 2017-2018. More in detail:

- The implementation of proton beam line dedicated to one-shot PIXE in ALLS facilities and PIXE experiments on Silicon based material (i.e. ceramic, pottery, painting)
- One-shot PIXE analysis on artwork provided by different museums. Research protocols are in preparation with the main European museum: Louvre, Vatican Museum, Egizian Museum of Turin
- Test of one-shot PIXE on Laser Facilities with characteristic different from Titan
- Realization of “Table-Top” line for one-shot PIXE
- Layer by Layer analysis by laser-driven PIXE, integrating an energy selector in the beam line
- Test of protective films with different bacteria and exposure on artworks and building surface.

All the obtained results were presented to Scientific International Community in several International Conferences and were published in prestigious International peer-reviewed journals (i.e. Scientific Reports, Applied Surface Science, Applied Physics Letters, Applied Physics A, Surface and Coatings). The complete publication list is indicated in the Appendix I.

Finally, I think that the main result of this Ph. D. thesis is the integration of three different scientific communities, methods and cultures, (laser-plasma, material science, Restoration and Conservation science), to achieve the common goal to protect, preserve, and transfer our cultural heritage to the future generation.

I can conclude this work citing UNESCO:

“The international cooperation in education, science, culture and communication strengthens the ties between nations and societies, and mobilizes the wider public so that each child and citizen:

- has access to quality education; a basic human right and an indispensable prerequisite for sustainable development;*
- may grow and live in a cultural environment rich in diversity and dialogue, where heritage serves as a bridge between generations and peoples;*
- can fully benefit from scientific advances;*
- and can enjoy full freedom of expression; the basis of democracy, development and human dignity”*

Conclusions and Future Perspectives

Publication List

1. Simona Veltri, M. Barberio, Chiara Liberatore, Massimiliano Scisciò, Antoine Laramée, Luigi Palumbo, Francois Legaré, Patrizio Antici. *Laser Stimulated Plasma-Induced Luminescence: a new method for on-air material analysis*. Applied Physics Letters, 110, 021114 (2017); DOI: 10.1063/1.4973467.
2. Marianna Barberio, Simona Veltri, Massimiliano Scisciò and Patrizio Antici. *Laser-Accelerated Proton Beams as Diagnostics for Cultural Heritage*. Scientific Report, | 7:40415 (2017); DOI: 10.1038/srep40415.
3. Massimiliano Scisciò, Marianna Barberio, Chiara. Liberatore, Simona Veltri, Antoine Laramée, Luigi Palumbo, Francois Legaré, Patrizio Antici. *Analysis of induced stress on materials exposed to laser-plasma radiation during high-intense laser experiments*. Applied Surface Science (in press)
4. Simona Veltri, Esen Sokullu, Marianna Barberio, Marc Andrea Gauthier, Patrizio Antici. *Synthesis and characterization of thin-transparent nanostructured films for surface protection*. Superlattices and Microstructures, 101, 209-218 (2017).
5. Marianna Barberio, Massimiliano Scisciò, Simona Veltri, Patrizio Antici. *Fabrication of nanostructured targets for improved laser-driven proton acceleration*. Superlattices and Microstructures, 95:159-163 (2016).
6. Marianna Barberio, Simona Veltri, Fabio Stranges, Assunta Bonanno, Fang Xu, Patrizio Antici. *AFM and Pulsed Laser Ablation Methods for Cultural Heritage: Application to Archeometric Analysis of Stone Artifacts*. Applied Physics A, 120, 909-916 (2015).
7. Diana Renzelli, Simona Veltri, Fabio Stranges, Pasquale Barone, Marianna Barberio, Fang Xu, Assunta Bonanno. *Laser Ablation Cleaning Effects on Thermoluminescence Dating Technique*. Archaeological Discovery, 2, 58-64 (2014). DOI:10.4236/ad.2014.23007

Attendance at International Conferences

1. Simona Veltri, Marianna Barberio, Esen Sokullu, Marc Andre Gauthier Patrizio Antici. *“Synthesis and characterization of thin-transparent nanostructured films for surface protection”*. Nanosmat Conference “10th International Conference on Surfaces, Coatings and Nanostructured Materials”, Portugal. September 6-9, 2016 (Poster Session)
2. Marianna Barberio, Simona Veltri, Federica Sirianni, Patrizio Antici. *Ageing processes of yellow pictorial layers under UV- white lighting and biological attack*. Green Conservation of Cultural Heritage Conference, Rome, Italy. October 27-28, 2015 (Poster Session)
3. Marianna Barberio, Massimiliano Scisciò, Simona Veltri, Patrizio Antici. *Laser-driven Proton Beams for Cultural Heritage Diagnostics: Theoretical simulations*. “Plasma Quebec: outils d’avenir” Conference, Montreal, Canada. June 3-5, 2015. (Poster Session)
4. Simona Veltri, Barberio Marianna, Massimiliano Scisciò, Javier Fernandez Tobias, Fang Xu, Julien Fuchs, Henry Pepin, Patrizio Antici. *Innovative Laser-Based Accelerators for Cultural Heritage*. National Laboratory Livermore “ National Ignition Facility/Jupiter Laser Facility, Meeting” California. February 09-11, 2015. (Poster Session)
5. Marianna Barberio, Simona Veltri, Esen Sokullu, Marc Andre Gauthier, Patrizio Antici. *Preparation and characterization of nanostructured films: study of hydrophobicity and antibacterial properties for surface protection*. ICACC’ 15 Conference “39 th International Conference and Expo on Advanced Ceramics and Composites”. Daytona, Florida. January 25-30, 2015. (Oral Presentation) (Chairs: Diana Santiago, NASA Glenn Research Center; Maria Paulo, INRS)
6. Marianna Barberio, Simona Veltri, Alessandra Imbrogno, Fang Xu, Patrizio Antici. *TiO₂ and SiO₂ nanoparticle films for cultural heritage: conservation and consolidation of ceramic and stone artifacts*. Nanosmat Conference “9th International Conference on Surfaces, Coatings and Nanostructured Materials”, Ireland. September 8-11, 2014. (Poster Session)

References

Chapter 1

1. P. Baglioni, E. Carretti and D. Chelazzi. *Nanomaterials in art conservation*. Nature Nanotechnology, 10: 287–290, (2015).
2. M. Bawaya. *Salvaging Science*. Science, 347:117-119, (2015).
3. S. Ruffolo, A. Macchia, M. F. La Russa, L. Mazza, C. Urzì, F. De Leo, M. Barberio, and G. M. Crisci. *Marine Antifouling for Underwater Archaeological Sites: TiO₂ and Ag-Doped TiO₂*. International Journal of Photo energy, (2013). Article ID 251647
4. M. F. La Russa, A. Macchia, S. A. Ruffolo, F. De Leo, M. Barberio, P. Barone, G. M. Crisci, C. Urzì. *Testing the antibacterial activity of doped TiO₂ for preventing biodeterioration of cultural heritage building materials*. International Biodeterioration & Biodegradation, 96:87, (2014).
5. K. Sterflinger, G. Pinar. *Microbial deterioration of Cultural Heritage and works of art-tilting at windmills? Applied Microbial Biotechnology*, 97:9637-9646, (2013).
6. C.A. Crispim and C.C. Gaylarde. *Cyanobacteria and Biodeterioration of Cultural Heritage: A review*. Microbial Ecology, 49:1-9, (2004).
7. W. Sand. *Microbial Mechanisms of Deterioration of Inorganic Substrates- A General Mechanistic Overview*. International Biodeterioration & Biodegradation, 40 n. 24:183-190, (1997).
8. C. Gaylarde, M. Ribas Silva, Th. Warscheid. *Microbial impact on building materials: an overview*. Materials and Structures, 36:342-352, (2003).
9. C. Ingrosso, C. Esposito Corcione, R. Striani, R. Comparelli, M. Striccoli, A. Agostiano, M. L. Curri, M. Frigione. *UV-Curable Nanocomposite Based on Methacrylic-Siloxane Resin and Surface-Modified TiO₂ Nanocrystals*. ACS Applied Materials & Interfaces, 7:15494-15505, (2015).

10. P.N. Manoudis, I. Karapanagiotis, A. Tsakalof, I. Zuburtikudis, B. Kolinkeová, C. Panayiotou. *Superhydrophobic films for the protection of outdoor cultural heritage assets*. Applied Physics A, 97:351-360, (2009).
11. T. Tajima, and J. M. Dawson. *Laser Electron Accelerator*. Physical Review Letters, 43:267, (1979).
12. W. Leemans, B. Nagler, A. J. Gonsalves, Cs. Tóth, K. Nakamura, C. G. R. Geddes, E. Esarey, C. B. Schroeder and S. M. Hooker. *GeV electron beams from a centimetre-scale accelerator*. Nature Physics 2, 696-699, (2006).
13. C. Geddes, Cs. Toth, J. Van Tilborg, E. Esarey, C. B. Schroeder, D. Bruhwiler, C. Nieter, J. Cary & W. P. Leemans. *High-quality electron beams from a laser wake field accelerator using plasma-channel guiding*. Nature, 431:538-541, (2004).
14. R. Snavely, R. A. Snavely, M. H. Key, S. P. Hatchett, T. E. Cowan, M. Roth, T. W. Phillips, M. A. Stoyer, E. A. Henry, T. C. Sangster, M. S. Singh, S. C. Wilks, A. MacKinnon, A. Offenberger, D. M. Pennington, K. Yasuike, A. B. Langdon, B. F. Lasinski, J. Johnson, M. D. Perry, and E. M. Campbell. *Intense High-Energy Proton Beams from Petawatt-Laser Irradiation of Solids* Physical Review Letters, 85:2945, (2000).
15. E. L. Clark, K. Krushelnick, J. R. Davies, M. Zepf, M. Tatarakis, F. N. Beg, A. Machacek, P. A. Norreys, M. I. K. Santala, I. Watts, and A. E. Dangor. *Measurements of Energetic Proton Transport through Magnetized Plasma from Intense Laser Interactions with Solids*. Physical Review Letters, 84:670, (2000).
16. S. Buffechoux, J. Psikal, M. Nakatsutsumi, L. Romagnani, A. Andreev, K. Zeil, M. Amin, P. Antici, T. Burris-Mog, A. Compant-La-Fontaine, E. D'Humieres, S. Fourmaux, S. Gaillard, F. Gobet, F. Hannachi, S. Kraft, A. Mancic, C. Plaisir, Gianluca Sarri, M. Taxisien, T. Toncian, U. Schramm, M. Tampo, P. Audebert, O. Willi, T.E. Cowan, H. Pepin, V. Tikhonchuk, M. Borghesi, and J. Fuchs. *Hot Electrons Transverse Refluxing in Ultraintense Laser-Solid Interactions*. Physical Review Letters 105, 015005, (2010).

17. S. Fourmaux, S. Buffechoux, B. Albertazzi, D. Capelli, A. Lévy, S. Gnedyuk, L. Lecherbourg, P. Lassonde, S. Payeur, P. Antici, H. Pépin, R. S. Marjoribanks, J. Fuchs, and J. C. Kieffer. *Investigation of laser-driven proton acceleration using ultra-short, ultra-intense laser pulses*. *Physics of Plasmas*, 20:013110, (2013).
18. K. Zeil, S. D. Kraft, S. Bock, M. Bussmann, T. E. Cowan, T. Kluge, J. Metzkes, T. Richter, R. Sauerbrey, and U. Schramm. *The scaling of proton energies in ultrashort pulse laser plasma acceleration*. *New Journal of Physics*, 12: 045015, (2010).
19. S. V. Bulanov and V. S. Khoroshkov. *Feasibility of using laser ion accelerators in proton therapy*. *Plasma Physics Report*, 28:453 (2002); V. Malka, S. Fritzler, E. Lefebvre, E. d’Humières, R. Ferrand, G. Grillon, C. Albaret, S. Meyroneinc, J.-P. Chambaret, A. Antonetti, D. Hulin. *Practicability of proton therapy using compact laser systems*. *Medical Physics*, 31:1587, (2004).
20. M. Roth, T. E. Cowan, M. H. Key, S. P. Hatchett, C. Brown, W. Fountain, J. Johnson, D. M. Pennington, R. A. Snavely, S. C. Wilks, K. Yasuike, H. Ruhl, F. Pegoraro, S. V. Bulanov, E. M. Campbell, M. D. Perry, and H. Powell. *Fast Ignition by Intense Laser-Accelerated Proton Beams*. *Physical Review Letters*, 86:436, (2001).
21. A. Mancic, J. Robiche, P. Antici, P. Audebert, C. Blancard, P. Combis, F. Dorchie, G. Faussurier, S. Fourmaux, M. Harmand, R. Kodama, L. Lancia, S. Mazevet, M. Nakatsutsumi, O. Peyrusse, V. Recoules, P. Renaudin, R. Shepherd, and J. Fuchs. *Isochoric heating of solids by laser-accelerated protons: Experimental characterization and self-consistent hydrodynamic modelling*. *High Energy Density Physics*, 6:21, (2010).
22. P. Antici, M. Migliorati, A. Mostacci, L. Picardi, L. Palumbo, and C. Ronsivalle. *A compact post-acceleration scheme for laser-generated protons*. *Physics of Plasmas* 18, 073103, (2011)

Chapter 2

1. P.N. Manoudis, A. Tsakalof, I. Karapanagiotis, I. Zuburtikudis, C. Panayiotou. *Fabrication of super-hydrophobic surfaces for enhanced stone protection*. Surface and Coatings Technology, 203:1322-1328, (2009).
2. M. F. La Russa, S. A. Ruffolo, N. Rovella, C. M. Belfiore, A. M. Palermo, M. T. Guzzi, G. M. Crisci. *Multifunctional TiO₂ coatings for Cultural Heritage*. Progress in Organic Coatings, 74:186-191, (2012).
3. S. A. Ruffolo, M. F. La Russa, M. Malagodi, O. Rossi, M. Palermo, M. Crisci. *ZnO and ZnTiO₃ Nano powders for antimicrobial stone coating*. Applied Physics A, 100:829-834, (2010).
4. G. Cappelletti, P. Fermo, F. Pino, E. Pargoletti, E. Pecchioni, F. Fratini, S. A. Ruffolo M. F. La Russa. *On the role of hydrophobic Si-based protective coatings in limiting mortar deterioration*. Environmental Science and Pollution Research, 22:17733–17743, (2015).
5. F. COMPANY. User Manual FEI Quanta 200 FEG, (2006).
6. H. G. M. Edwards and J. M. Chalmers. *Raman Spectroscopy in Archaeology and Art History*. Analytical and Bioanalytical Chemistry, 385:1037-1038, (2006).
7. R. Lewis and H. Edwards. *Handbook of Raman Spectroscopy: From the Research Laboratory to the Process Line*. CRC Press, New York, NY, USA, (2001).
8. Joseph D. Andrade. *X Ray Photoelectron Spectroscopy (XPS)*. New York, NY: Surface and Interfacial Aspect of Biomedical Polymers, 105-195, (1985).
9. G. PK. *Introduction to Photoelectron Spectroscopy*. New York, NY: John Wiley and Sons, Inc., (1983).
10. G. J. Vickerman. *Surface Analysis – The Principal techniques-* 2nd Edition, John Wiley & Sons, (2009).
11. C. Ronda. *Luminescence: From theory to applications*, Weinheim: Wiley - VCH, (2008).

12. SI. Salem, SL. Panossian, RA. Krause. *Experimental K and L relative x-ray emission rates*. Atomic Data Nuclear Data Tables, 14:91, (1974).
13. JH: Scofield. *Relativistic hartree-slater values for K and L X-ray emission rates*. Atomic Data and Nuclear Data Tables, 14:121-137, (1974).
14. Perujio, JA. Maxwell, WJ. Campbell. *Deviation of the $K\beta/K\alpha$ intensity ratio from theory observed in proton-induced X-ray spectra in the $22 \leq Z \leq 32$ region*. Journal of Physics B: Atomic and Molecular Physics, 20:4973, (1987).
15. MO. Krause. *Atomic radiative and radiationless yields for K and L shells*. Journal of Physical and Chemical Reference Data, 8:307, (1979).
16. W. Maenhaut, H. Raemdonck. *Accurate calibration of a Si(Li) detector for PIXE analysis*. Nuclear Instruments and Methods B1:123, (1984); H. Paul. *A test of theoretical K-shell ionization cross sections for protons*. Nuclear Instruments and Methods, B42:443, (1989).
17. JH. Hubbell. *National institute of Standards and Technology Report NISTIR 89-4144*. US Department of Commerce, Gaithersburg, MD,(1989).
18. DD. Cohen, E. Clayton. *A discussion of PIXAN and PIXANPC: The AAEC PIXE analysis computer packages*. Nuclear Instruments and Methods in Physics Research, B22:59, (1987).
19. DD. Cohen. *K and L shell X-ray cross sections for use in PIXE analysis systems*. Nuclear Instruments and Methods, B49:1, (1990).
20. DD. Cohen, M. Harrigan. *Calculated L-shell X-ray line intensities for proton and helium ion impact*. Atomic Data Nuclear Data Tables, 34:393, (1986).
21. DD. Cohen M. Harrigan. *K- and L-shell ionization cross sections for protons and helium ions calculated in the ecpsr theory*. Atomic Data Nuclear Data Tables, 33:255, (1985).
22. SAE Johansson, TB. Johansson. *Analytical application of particle induced X-ray emission*. Nuclear Instruments and Methods, 37:473, (1976).

23. W-K. Chu, JW Mayer, M-A Nicolet. *Backscattering Spectrometry*. New York: Academic Press, (1978).
24. W. Scharf. *Particle Accelerators: Applications in Technology and Research*. Taunton, UK: Research Studies Press Ltd., (1989)
25. Fujishima and K. Honda. *Electrochemical photolysis of water at a semiconductor electrode*. *Nature*, 238:37–38, (1972).
26. C. Urzì. *Microbial Deterioration of Rocks and Marble Monuments of the Mediterranean Basin: A Review*. *Corrosion Review*, 22:441, (2004).
27. S. Scheerer, O. Ortega-Morales, C. Gaylarde. *Microbial Deterioration of Stone Monuments-An Updated Overview*. *Advanced Applied Microbiology*, 66:97-139, (2009).
28. ML. Suihko, HL. Alakomi, A. Gorbushina, I. Fortune, J. Marquardt, M. Saarela. *Characterization of aerobic bacterial and fungal microbiota on surfaces of historic Scottish monument*. *Systematic and Applied Microbiology*, 30:494–508, (2007). DOI: 10.1016/j.syapm.2007.05.001.
29. C. Urzi, F. De Leo. *Evaluation of the efficiency of water-repellent and biocide compounds against microbial colonization of mortars*. *International Biodeterioration & Biodegradation*, 60:25-34, (2007).
30. K. Sterflinger, G. Piñar. *Microbial deterioration of cultural heritage and works of art — tilting at windmills?* *Applied Microbiology and Biotechnology*, 97: 9637–9646, (2013).
31. A. Polo, F. Cappitelli, L. Brusetti, P. Principi, F. Villa, L. Giacomucci, G. Ranalli, C. Sorlini. *Feasibility of Removing Surface Deposits on Stone Using Biological and Chemical Remediation Methods*. *Microbiology Ecology*, 60:1–14 (2010). DOI: 10.1007/s00248-009-9633-6.
32. D. Maxim, L. Bucşa, M. I. Moza, O. Chachula. *Preliminary antifungal investigation of ten biocides against moulds from two different church frescoes*. *Annals of RSBC*, 17:139, (2012).

33. D. Pinna, B. Salvadori, M. Galeotti. *Monitoring the performance of innovative and traditional biocides mixed with consolidants and water-repellents for the prevention of biological growth on stone.* Science of the Total Environment, 423:132–141,(2012).
34. A. Shalaby, T. Angelova, A. Bachvarova-Nedelcheva, N. Georgieva, R. Iordanova, A. Staneva, Yanko Dimitriev. *Sol-gel synthesis of materials in the system $\text{SiO}_2/\text{ZnO}/\text{TiO}_2/\text{RGO}$ and their antimicrobial efficiency against *E. Coli* K12.* Comptes rendus de l'Acad'emie bulgare des Sciences,69:1, (2015).
35. M. F. La Russa, S. A. Ruffolo, N. Rovella, C. M. Belfiore, A. M. Palermo, M. T. Guzzi, G. M. Crisci. *Multifunctional TiO_2 coatings for Cultural Heritage.* Progress in Organic Coatings,74:1, 186-191, (2012).
36. K. Gupta, R. P. Singh, A. Pandey. *Photocatalytic antibacterial performance of TiO_2 and Ag-doped TiO_2 against *S. aureus*, *P. aeruginosa* and *E. Coli*.* Journal of Nanotechnology, 4.1, 345–351, (2013).
37. P. C. Maness, S. Smolinski, D. M. Blake, Z. Huang, E. J. Wolfrum, W.A. Jacoby. *Bactericidal Activity of Photocatalytic TiO_2 Reaction: toward an Understanding of Its Killing Mechanism.* Applied and Environmental Microbiology, 65: 4094-4098, (1999).
38. H. Hitkova, A. Stoyanova, N. Ivanova, M. Sredkova, V. Popova, R. Iordanova, A. Bachvarova-Nedelcheva. *Study of antibacterial activity of non-hydrolytic synthesized TiO_2 againsts *E. Coli*, *P. Aeruginosa* and *S. Aureus*.* Journal of Optoelectronics and Biomedical Materials, 4:1, 9-17, (2012).
39. V. Iliev, D. Tomova, L. Bilyarska, A. Eliyas, L. Petrov. *Photocatalytic properties of TiO_2 modified with platinum and silver nanoparticles in the degradation of oxalic acid in aqueous solution.* Applied Catalysis B, 63:266–271 (2006).
40. P.C. Maness, S. Smolinski, D.M. Blake, Z. Huang, E.G. Wolfrum, W.A. Jacoby. *Bactericidal Activity of Photocatalytic TiO_2 Reaction: toward an Understanding of Its Killing Mechanism.* Applied and Environmental Microbiology, 65: 4094-4098 (1999).

41. L. Yuexiang, P. Shaoqin, J. Fengyi, L. Gongxuan, L. Shuben. *Effect of doping TiO₂ with alkaline-earth metal ions on its photocatalytic activity*. Journal of the Serbian Chemical Society, 72:393-402, (2007).
42. M. H. Mangrola. *Dielectric and optical behavior of Sr-doped TiO₂ synthesized by solid state reaction method*. AIP Conference Proceeding, 1536:767, (2013).
43. Z. Jun-Feng, S. Xiao-Li, L. Ji-Lai, H. Xu-Ri. *Theoretical Study of Methanol C-H and O-H Bond Activation by Pt-Ru Clusters*. Chemical Journal of Chinese Universities, 27(2), 314-318, (2006).
44. X.G. Hou, M.D. Huang, X.L Wu, A.D. Liu. *Preparation and studies of photocatalytic silver-loaded TiO₂ films by hybrid sol-gel method*. Chemical Engineering Journal, 146:42-48, (2009).
45. A. Erkan, U. Bakir, G. Karakas. *Photocatalytic microbial inactivation over Pd doped SnO₂ and TiO₂ thin films*. Journal of Photochemistry and Photobiology, 184:313-321, (2006).
46. R. Zhou, P. Liu, L. Fu, X. Lan, G. Gong. *Improvement of the Antibacterial Activity of Nanocrystalline Zinc Oxide by Doping Mg (II) or Sb (III)*. Journal of Applied Technology, 8:1087-1098, (2011).
47. O. Akhavan. *Lasting antibacterial activities of Ag-TiO₂/Ag/a-TiO₂ nanocomposite thin film*. Journal of Colloid and Interface Science, 336:117-124, (2009).
48. X. Xue, Y. Wang, H. Yanga. *Preparation and characterization of boron-doped titania nano-materials with antibacterial activity*. Journal of Applied Surface Science, 264:94-99, (2013).
49. J. Xua, Y. Ao, M. Chena, D. Fuc. *Low-temperature preparation of boron doped titania by hydrothermal method and its photocatalytic activity*. Journal of Alloys and Compounds, 484:73-79, (2009).

50. M. G. Nair, M. Nirmala, K. Rekha, A. Anukaliani. *Structural, optical, photo catalytic and antibacterial activity of ZnO and Co doped ZnO nanoparticles*. Journal of Materials Letters, 65:1797-1800, (2011).
51. S. Liu, T.H. Zeng, M. Hofmann, E. Burcombe, J. Wei, R. Jiang, J. Kong, and Y. Chen. *Antibacterial Activity of Graphite, Graphite Oxide, Graphene Oxide, and Reduced Graphene Oxide: Membrane and Oxidative Stress*. Journal of Acs Nano, 5:6971-6980, (2011).
52. J. Ma, J. Zhang, Z. Xiong, Y. Yong and X. S. Zhao. *Preparation, characterization and antibacterial properties of silver-modified graphene oxide*. Journal of Materials Chemistry, 21:3350, (2011).
53. A. Nel, T. Xia, L. Mädler, N. Li. *Toxic potential of materials at the nanolevel*. Science 311:622-627, (2006).
54. M. Jones, Eric M. V. Hoek. *A review of the antibacterial effects of silver nanomaterials and potential implications for human health and the environment*, Journal of Nanoparticles Research, 12:1531-1551, (2010).
55. H. Wenbing, P. Cheng, L. Weijie, L. Min, L. Xiaoming, L. Di, H. Qing, F. Chunhai. *Graphene-Based Antibacterial Paper*. Journal of Acs Nano, 4:4317-4323, (2010).

Chapter 3

1. C. Marambio, M.V. Hoek. *A review of the antibacterial effects of silver nanomaterials and potential implications for human health and the environment*. Journal of Nanoparticle Research, 12:1531-1551, (2010).
2. M.E. Young, H. L. Alakomi, I. Fortune, A. A. Gorbushina, W.E. Krumbein, I. Maxwell, C. McCullagh, P. Robertson, M. Saarela, J. Valero, M. Vendrell. *Development of a biocidal treatment regime to inhibit biological growths on cultural heritage: BIODAM*. Journal of Environmental Geology, 56:631-641, (2008).
3. A. Erkan, H. Bakir, G. Karakas. *Photocatalytic microbial inactivation over Pd doped SnO₂ and TiO₂ thin films*. Journal of Photochemistry and Photobiology, 184:313-321, (2006).
4. R. Zhou, P. Liu, L. Fu, X: Lan, G. Gong. *Improvement of the Antibacterial Activity of Nanocrystalline Zinc Oxide by Doping Mg (II) or Sb (III)*. Journal of Applied Technology, 8:1087-1098, (2008).
5. O. Akhavan, A. Ghaderi. *Toxicity of Graphene and Graphene Oxide Nanowalls Against Bacteria*. Acs Nano, 4: 5731-5736, (2010).
6. P. Baglioni, E. Carretti, D. Chelazzi. *Nanomaterials in art conservation*. Nature Nanotechnology, 10:287–290, (2015).
7. M. Bawaya. *Salvaging Science*. Science, 347:6218, 108, (2015).
8. K. Sterflinger, G. Pinar. *Microbial deterioration of Cultural Heritage and works of art-tilting at windmills?* Applied microbial Biotechnology 97:9637-9646, (2013).
9. Crispim, C. C. Gaylarde. *Cyanobacteria and Biodeterioration of Cultural Heritage: A review*. Microbial Ecology, 49:1-9, (2004).
10. K. Sterflinger. *Fungi: Their role in deterioration of cultural heritage*. Fungal biology reviews, 24:47-55, (2010).

11. V. Jurado, S. Sanchez-Moral, C. Saiz-Jimenez. *Entomogenous fungi and the conservation of the cultural heritage: A review*. International Biodeterioration & Biodegradation, 62:325–330, (2008).
12. Al-Omariet, X. Brunetaud, K. Beck, M. Al-Mukhtar. *Effect of thermal stress, condensation and freezing–thawing action on the degradation of stones on the Castle of Chambord, France*. Environmental Earth Science, 71: 3977–3989, (2014).
13. W. Sand. *Microbial Mechanisms of Deterioration of Inorganic Substrates - A General Mechanistic Overview*. International Biodeterioration & Biodegradation, 40:183-190, (1997).
14. C. Gaylarde, M. Ribas Silva, Th. Warscheid. *Microbial impact on building materials: an overview*. Materials and Structures, 36:342-352, (2003).
15. S. Ruffolo, A. Macchia, M. F. La Russa, L. Mazza, C. Urzì, F. De Leo, M. Barberio, G.M. Crisci. *Marine Antifouling for Underwater Archaeological Sites: TiO₂ and Ag-Doped TiO₂*. International Journal of Photoenergy, 2013, (2013). Article ID 251647.
16. M. F. La Russa, A. Macchia, S. R. Ruffolo, F. De Leo, M. Barberio, P. Barone, G. M. Crisci, C. Urzì. *Testing the antibacterial activity of doped TiO₂ for preventing biodeterioration of cultural heritage building materials*. International Biodeterioration & Biodegradation, 96:87, (2014).
17. T. Warscheid. *Impact of microbial biofilm in the deterioration of inorganic building materials and their relevance for the conservation practice*. Restoration of Buildings and Monuments, 2:493-504, (1996).
18. Y. Nuhoglu, E. Oguz, H. Uslu, A. Ozbek, B. Ipekoglu, I. Ocak, İ. Hasenekoglu. *The accelerating effects of the microorganisms on biodeterioration of stone monuments under air pollution and continental-cold climatic conditions in Erzurum, Turkey*. Science of the Total Environment, 364, 272-283, (2005).
19. a) G. Alessandrini, M. Aglietto, V. Castelvetro, F. Ciardelli, R. Peruzzi, L. Toniol. *Comparative evaluation of fluorinated and un-fluorinated acrylic copolymers as water-*

- repellent coating materials for stone*. Journal of Applied Polymer Science, 76:962, (2000); b) L. Toniolo, T. Poli, V. Castelvetro, A. Manariti, O. Chiantore, M. Lazzari. *Development of nanocomposites for conservation of artistic stones*. Journal of Cultural Heritage 3: 309, (2002); c) G. C. Borgia, G. C. Borgia, M. Camaiti, F. Cerri, P. Fantazzini & Franco Piacenti. *Hydrophobic treatments for stone conservation: influence of the application method on penetration, distribution, and efficiency*. Journal of Studies in Conservation, 48:217,(2003); d) A. Tsakalo, P. Manoudis, I. Karapanagiotis, I. Chrysoulakis, C. Panayiotou. *Assessment of synthetic polymeric coatings for the protection and preservation of stone monuments*. Journal of Cultural Heritage, 8:69, (2007); e) L. D'Arienzo, P. Scarfato, L. Incarnato. *New polymeric nanocomposites for improving the protective and consolidating efficiency of tuff stone*. Journal of Cultural Heritage 9:253, (2008).
20. P. N. Manoudis, I. Karapanagiotis, A. Tsakalof, I. Zuburtikudis, B. Kolinkeová, C. Panayiotou. *Superhydrophobic films for the protection of outdoor cultural heritage assets*. Applied Physics A, 97:2, 351-360, (2009).
21. T. Mashino, K. Okuda, T. Hirota, M. Hirobe, T. Nagano, M. Mochizuki. *Inhibition of E. coli growth by fullerene derivatives and inhibition mechanism*. Bioorganic & Medicinal Chemistry Letters, 9:2959, (1999).
22. N. Tsao, T.-Yau Luh, C-Kung Chou, J.-Jong Wu, Y.-Shin Lin, and H.-Yao Lei. *Inhibition of Group A Streptococcus Infection by Carboxy fullerene*. Antimicrobial Agents and Chemotherapy, 45:1788, (2001).
23. S. J. Klaine, P. J. J. Alvarez, G. E. Batley, T. E. Fernaneds, R. D. Handy, D. Y. Lyon, S. Mahendra, M. J. McLaughlin. *Nanomaterials in the environment: Behavior, fate, bioavailability, and effects*. Environmental Toxicology and Chemistry, 27:1825, (2008).
24. S. Liu, T. Helen Zeng, M. Hofmann, E. Burcombe, J. Wei, R. Jiang, J. Kong, and Y. Chen. *Activity of Graphite, Graphite Oxide, Graphene Oxide, and Reduced Graphene Oxide: Membrane and Oxidative Stress*. ACS Nano, 5:6971, (2011).

25. C.-Nam Lok, C.-Ming Ho, R. Chen, Q.-Yu He, W.-Yiu Yu, H. Sun, P. K.-Hang Tam, J.-Fu Chiu, and C.-Ming Che. *Proteomic Analysis of the Mode of Antibacterial Action of Silver Nanoparticles*. Journal of proteome Research, 5: 916, (2006).
26. S. J. Klaine, P. J. J. Alvarez, G.E. Batley, T. F. Fernanedes, R. D. Handy, D. Y. Lyon, S. Mahendra, M. J. McLaughlin. *Nanomaterials in the environment: Behavior, fate, bioavailability, and effects*. Environmental Toxicology and Chemistry, 27:1825, (2008).
27. S. Liu, T.H. Zeng, M. Hofmann, E. Burcombe, J. Wei, R. Jiang, J. Kong, Y. Chen. *Antibacterial Activity of Graphite, Graphite Oxide, Graphene Oxide, and Reduced Graphene Oxide: Membrane and Oxidative Stress*. ACS Nano, 5:6971, (2011).
28. C.-Nam Lok, C.-Ming Ho, R. Chen, Q.-Yu He, W.-Yiu Yu, H. Sun, P. Kwong-Hang Tam, J.-Fu Chiu, and C.-Ming Che. *Proteomic Analysis of the Mode of Antibacterial Action of Silver Nanoparticles*. Journal of proteome research, 5:916, (2006).
29. S. Bosi, T. Da Ros, G. Spalluto, M. Prato. *Fullerene derivatives: an attractive tool for biological applications*. European Journal of Medicine Chemistry, 38:913, (2013).
30. O. Akhavan, E. Ghaderi. *Escherichia coli bacteria reduce graphene oxide to bactericidal graphene in a self-limiting manner*. Carbon, 50:1853-1860, (2012).
31. M. Bawaya. *Salvaging Science*. Science, 347:6218, (2015).
32. O. Akhavan, E. Ghaderi. *Escherichia coli bacteria reduce graphene oxide to bactericidal graphene in a self-limiting manner*. Carbon, 50:1853-1860 (2012).
33. C. M Santos, J. Mangadlao, F. Ahmed, A. Leon, R. C. Advincula and D. F Rodrigues. *Graphene nanocomposite for biomedical applications: fabrication, antimicrobial and cytotoxic investigations*. Nanotechnology, 23:395101, (2012).
34. A. Bianco. *Graphene: Safe or Toxic? The Two Faces of the Medal*. Angewandte Chemie -International Edition, 52:4986, (2013).

35. D.Y. Lyon, L. Brunet, G. W. Hinkal, M. R. Wiesner, P. J. Alvarez. *Antibacterial Activity of Fullerene Water Suspensions (nC60) Is Not Due to ROS-Mediated Damage*. Nano Letters, 8:1539, (2008).
36. Data sheet
<http://www.sigmaaldrich.com/catalog/product/aldrich/761036?lang=it®ion=IT>.
37. M. Jin, X. Feng, J. Xi, J. Zhai, K. Cho, L. Feng, L. Jiang. *Super-Hydrophobic PDMS Surface with Ultra-Low Adhesive Force*. Macromolecular Rapid Communications, 26:1805-1809, (2005).
38. UNI EN 539-2
39. UNI 10925:2001
40. M. Rodney Donlan. *Biofilms: Microbial Life on Surfaces*. Emerging Infectious Diseases, 8:9, 881-890, (2002).
41. T. Abee, A. T. Kovács, O. P. Kuipers, S. Van Der Veen. *Biofilm formation and dispersal in Gram-positive bacteria*. Current Opinion in Biotechnology, 22:2, 172–9 (2010). DOI:10.1016/j.copbio.2010.10.016.
42. P. Vo, M. Nunez. *Bdellovibrio bacteriovorus Predation in Dual-Species Biofilms of E. coli Prey and M. luteus Decoys*. arXiv:1005.3582, (2010).
43. Venier. A. Fraggadaki, M. Kostadima, E. Chatzisyneon, V. Binas, A. Zachopoulos, G. Kirikidis, D. Mantzavinos. *Solar light and metal-doped TiO₂ to eliminate water-transmitted bacterial pathogens: Photocatalyst characterization and disinfection performance*. Applied Catalysis B: Environmental, 93:154-155, (2014).
44. D. Venieria, I. Gounakia, V. Binasb, A. Zachopoulos, G. Kiriakidis, D. Mantzavinos. *Inactivation of MS2 coliphage in sewage by solar photocatalysis using metal-doped TiO₂*. Applied Catalysis B: Environmental, 178:54-64, (2015).

45. D.Y. Lyon, L. Brunet, G. W. Hinkal, M. R. Wiesner, P. J. Alvarez. *Antibacterial Activity of Fullerene Water Suspensions (nC60) Is Not Due to ROS-Mediated Damage*. Nano Letters, 8:1539, (2008).
46. Data sheet:
<http://www.sigmaaldrich.com/catalog/product/aldrich/761036?lang=it®ion=IT>.
47. V. Amendola, M. Meneghetti. *What controls the composition and the structure of nanomaterials generated by laser ablation in liquid solution?* Physical Chemistry Chemical Physics, 15:3027-3046, (2013).
48. K.L. Kelly, E. Coronado, L.L. Zhao, G.C. Schatz. *The Optical Properties of Metal Nanoparticles: The Influence of Size, Shape, and Dielectric Environment*. Journal of Physical Chemistry, B 107:668,(2003).
49. E. D. Palik. *Handbook of Optical Constants of Solids*. Academic Press, (1998).
50. J.C. Vickerman, I.S. Gilmore. *Surface Analysis - The Principal Techniques, 2nd Edition*. Wiley & Sons, (2009).
51. J. Cumpson. *The Thickogram: a method for easy film thickness measurement in XPS*. Surface Interface Analysis, 29:403, (2000).
52. Y. Leprince Wang. *Study of the initial stages of TiO₂ growth on Si wafers by XPS*. Surface and Coatings Technology, 150:257, (2002).
53. V. Amendola, M. Meneghetti. *Size Evaluation of Gold Nanoparticles by UV-Vis Spectroscopy*. Journal of Physical Chemistry C, 113:4277, (2009).
54. <http://srdata.nist.gov/xps/>
55. <http://www.csiro.au/luminescence/about.html>
56. F. Stranges, M. Barberio, P. Barone, A. Abenante, A. Leuzzi, P. Sapia, F. Xu, A. Bonanno. *Deposition of Transparent, Hydrophobic TiO₂ Film for the Protection of Outdoor and Marine Cultural Heritage Assets*. Archaeological Discovery, 2:32, (2013).

57. G. Bitossi, R. Giorgi, M. Mauro, B. Salvadori, L. Dei. *Spectroscopic Techniques in Cultural Heritage Conservation: A Survey*. Applied Spectroscopy Reviews, 40:187-228, (2005).
58. M.F. La Russa, A. Macchia, S.A. Ruffolo, F. De Leo, M. Barberio, P. Barone, G.M. Crisci. *Testing the antibacterial activity of doped TiO₂ for preventing biodeterioration of cultural heritage building materials*. International Biodeterioration & Biodegradation, 96:87, (2014).
59. M. Schreiner, M. Melcher, K. Uhler. *Scanning electron microscopy and energy dispersive analysis: applications in the field of cultural heritage*. Analytical and Bioanalytical Chemistry, 387:737–747, (2007).
60. C. Urzi, M.C. Valles, M. Vendrell, M. Pernice. *Biomineralization Processes on Rock and Monument Surfaces Observed in Field and in Laboratory Conditions*. Geomicrobiology Journal, 16:1, 39-54, (1999).
61. A. De los Rios, C. Ascaso. *Contributions of in situ microscopy to the current understanding of stone biodeterioration*. International Microbiology, 8:181–188, (2005).
62. L.K. Herrera, C. Arroyave, P. Guiamet, S.G. De Saravia, H. Videla. *Biodeterioration of peridotite and other constructional materials in a building of the Colombian Cultural Heritage*. International Biodeterioration & Biodegradation, 54:135–141, (2004).
63. G. Chidichimo, F. Dalena. *Proceedings of the V International Conference on the Rock Civilization* (2011).
64. F. Russo. *Origini e sviluppo della città di Paola*. Tipografia La Nuovissima: Acerra (1971).
65. A. M. Panno. *La chiesa ipogea di Sotterra (sec. IX–X)*. Cosenza, Editoriale Progetto, (2007).

66. P. Pouli, M. Oujja, M. Castillejo. *Practical issues in laser cleaning of stone and painted artefacts: optimisation procedures and side effects*. Applied Physics A, 106:447-464, (2012).
67. D. Camuffo. *Microclimate for Cultural Heritage: Conservation, Restoration and Maintenance of Indoor and Outdoor Monuments - 2nd Edition*. Elsevier, San Diego, (2014).
68. Uni Normal Regulations: [http://www.icr.arti.beniculturali.it/Nor mal/Normal.htm](http://www.icr.arti.beniculturali.it/Nor%20mal/Normal.htm).
69. M. Barberio, P. Barone, F. Stranges, D. Renzelli, F. Xu, A. Bonanno. *Effect of Laser Ablation Cleaning Process on Ceramic Artifacts*. Journal of Physical Science and Application, 4:224–228, (2013).
70. S. Rescic, P. Tiano, F. Fratini, R. Manganelli del Fà. *The micro-sandblasting technique as a new tool for the evaluation of the state of conservation of natural stone and mortar surfaces*. European Journal of Environmental and Civil Engineering, 17(2): 113-127, (2013).
71. PL data base: <http://www.csiro.au/luminescence/>
72. Di Sipio, A. Galgaro, E. Destro, G. Teza, S. Chiesa, A. Giaretta, A. Manzella. *Subsurface thermal conductivity assessment in Calabria (southern Italy): a regional case study*. Journal of Environmental Earth Science, 72: 1383-1401, (2014).
73. S.I. Anisimov, B.S. Luk'yanchuk. *Selected problems of laser ablation theory*. Physics Uspekhi, 45:3, 293-324, (2002).
74. De Filippis, S. Margiotta, S. Negri, M. Giudici. *Numerical modeling of the groundwater flow in the fractured and karst aquifer of the Salento peninsula (Southern Italy)*. Environmental Earth Science, 67:1891-1907 (2012). DOI:10.1007/s12665-012-1631-1

Chapter 4

1. Yogo, K. Sato, M. Nishikino, M. Mori, T. Teshima, H. Numasaki, M. Murakami, Y. Demizu, S. Akagi, S. Nagayama, K. Ogura, A. Sagisaka, S. Orimo, M. Nishiuchi, A. S. Pirozhkov, M. Ikegami, M. Tampo, H. Sakaki, M. Suzuki, I. Daito, Y. Oishi, H. Sugiyama, H. Kiriyaama, H. Okada, S. Kanazawa, S. Kondo, T. Shimomura, Y. Nakai, M. Tanoue, H. Sasao, D. Wakai, P. R. Bolton, and H. Daido. *Application of laser-accelerated protons to the demonstration of DNA double-strand breaks in human cancer cells*. Applied Physics Letters, 98:053701, (2011).
2. R. E. Van Grieken, A. A. Markowicz. *Handbook of X-ray Spectrometry-2nd Edition*. Marcel Dekker, Inc, New York (2002).
3. G. Bitossi, R. Giorgi, M. Mauro, B. Salvadori & L. Dei. *Spectroscopic techniques in cultural heritage conservation: a survey*. Applied Spectroscopy Reviews, 40:187-228 (2005).
4. La recherche au musée du Louvre 2012, Musée du Louvre, Paris, ISBN 978-2-35031-483-9 and Louvre Laboratory web site: <http://c2rmf.fr/>.
5. M. Massi, L. Giuntini, M. Chiari, N. Gelli, P.A. Mando. *The external beam microprobe facility in Florence: Set-up and performance*. Nuclear Instruments and Methods in Physics Research B, 190:276-282, (2002).
6. L. Giuntini, M. Massi, S. Calusi. *The external scanning proton microprobe of Firenze: A comprehensive description*. Nuclear Instruments and Methods in Physics Research A, 576:266-273, (2007).
7. K. Janssens, R. Van Grieken. *Nondestructive microanalysis of Cultural Heritage Materials*. Wilson & Wilson's, XLII Volume, Amsterdam (2004).
8. J. Fuchs, P. Antici, E. D'Humières, E. Lefebvre, M. Borghesi, E. Brambrink, C. A. Cecchetti, M. Kaluza, V. Malka, M. Manclossi, S. Meyroneinc, P. Mora, J. Schreiber, T.

- Toncian, H. Pépin, & P. Audebert. *Laser-driven proton scaling laws and new paths towards energy increase*. Nature Physics, 2:48-54, (2006).
9. L. Robson, P. T. Simpson, R. J. Clarke, K. W. D. Ledingham, F. Lindau, O. Lundh, T. McCanny, P. Mora, D. Neely, C. Wahlström, C.-G. Zepf, and P. McKenna. *Scaling of proton acceleration driven by petawatt-laser-plasma interactions*. Nature Physics, 3, 58-62, (2007).
 10. T.E. Cowan, J. Fuchs, H. Ruh, A. Kemp, P. Audebert, M. Roth, I. Stephens, R. Barton, A. Blazevic, E. Brambrink, J. Cobble, J. Fernandez, J.-C. Gauthier, M. Geiss, M. Hegelich, J. Kaae, S. Karsch, G.P. Le Sage, S. Letzring, M. Manclossi, S. Meyroneinc, A. Newkirk, H. Pepin, and Renard -Le Galloudec. *Ultralow Emittance, Multi-MeV Proton Beams from a Laser Virtual-Cathode Plasma Accelerator*. Physical Review Letters, 92:204801, (2004).
 11. M. Borghesi, A. J. Mackinnon, D. H. Campbell, D. G. Hicks, S. Kar, P. K. Patel, D. Price, L. Romagnani, A. Schiavi, and O. Willi. *Multi-MeV Proton Source Investigations in Ultraintense Laser-Foil Interactions*. Physical Review Letters, 92: 055003, (2004).
 12. T. E. Cowan, J. Fuchs, H. Ruhl, A. Kemp, P. Audebert, M. Roth, R. Stephens, I. Barton, A. Blazevic, E. Brambrink, J. Cobble, J. Fernández, J.-C. Gauthier, M. Geissel, M. Hegelich, J. Kaae, S. Karsch, G. P. Le Sage, S. Letzring, M. Manclossi, S. Meyroneinc, A. Newkirk, H. Pépin, and N. Renard-LeGalloudec. *Ultralow Emittance, Multi-MeV Proton Beams from a Laser Virtual-Cathode Plasma Accelerator*. Physical Review Letters, 92:204801, (2004).
 13. A. Mancic, J. Robiche, P. Antici, P. Audeber, C. Blancard, P. Combis, F. Dorchies, G. Faussurier, S. Fourmaux, M. Harmande, R. Kodamag, L. Lanciaa, S. Mazevetd, M. Nakatsutsumia, O. Peyrussee, V. Recoulesd, P. Renaudind, R. Shepherd, J. Fuchs. *Isochoric heating of solids by laser-accelerated protons: Experimental characterization and self-consistent hydrodynamic modelling*. High Energy Density Physics, 6:21, (2010).
 14. S. V. Bulanov and V. S. Khoroshkov, Plasma Phys. Rep. 28, 453 (2002); V. Malka, Sven Fritzler, Erik Lefebvre, Emmanuel d’Humières, Régis Ferrand, Georges Grillon, Claude

- Albaret, Samuel Meyroneinc, Jean-Paul Chambaret, Andre Antonetti, Danièle Hulin, Med. Phys. 31, 1587 (2004).
15. J. Metzkes, T.E. Cowan, L. Karsch, S.D. Kraft, J. Pawelke, C. Richter, T. Richter, K. Zeila, U. Schramm. *Preparation of laser-accelerated proton beams for radiobiological applications*. Nuclear Instruments and Methods Physics Research Section A, 653:172, (2011).
16. D. Doria, K. F. Kakolee, S. Kar, S. K. Litt, F. Fiorini, H. Ahmed, S. Green, J. C. G. Jeaynes, J. Kavanagh, D. Kirby, K. J. Kirkby, C. L. Lewis, M. J. Merchant, G. Nersisyan, R. Prasad, K. M. Prise, G. Schettino, M. Zepf, and M. Borghesi. *Biological effectiveness on live cells of laser driven protons at dose rates exceeding 109 Gy/s*. AIP Advances, 2:011209, (2012).
17. P. Baglioni, E. Carretti, D. Chelazzi. *Nanomaterials in art conservation*. Nature Nanotechnology 10:287–290 (2015).
18. J. Metzkes, T.E. Cowan, L. Karsch, S.D. Kraft, J. Pawelke, C. Richter, T. Richter, K. Zeila, U. Schramm. *Preparation of laser-accelerated proton beams for radiobiological applications*. Nuclear Instruments and Methods Physics Research Section A 653:172,(2011).
19. P. Baglioni, E. Carretti, D. Chelazzi. *Nanomaterials in art conservation*. Nature Nanotechnology, 10:287–290, (2015).
20. Mancic, A. et al. *Isochoric heating of solids by laser-accelerated protons: Experimental characterization and self-consistent hydrodynamic modeling*. High Energy Density Physics 6, 21 (2010).
21. P. K. Patel, A. J. Mackinnon, M. H. Key, T. E. Cowan, M. E. Ford, M. Allen, D. F. Price, H. Ruhl, P. T. Springer, and R. Stephens. *Isochoric Heating of Solid-Density Matter with an Ultrafast Proton Beam*. Physical Review Letters, 91:125004, (2003).
22. TITAN Laser characteristic: <https://jlf.llnl.gov/> (Date of access: 05/05/2016) (2015).

23. B. Albertazzi, P. Antici, J. Bocker, M. Borghesi, S. Chen, V. Dervieux, E. d'Humières, L. Lancia, M. Nakatsutsumi, R. Shepherd, L. Romagnani, Y. Sentoku, M. Swantusch, O. Willi, H. Pépin and J. Fuchs. *Longitudinal proton probing of ultrafast and high-contrast laser-solid interactions*. EPJ Web of Conferences, 59:17014, (2013).
24. J. Fuchs, Y. Sentoku, S. Karsch, J. Cobble, P. Audebert, A. Kemp, A. Nikroo, P. Antici, E. Brambrink, A. Blazevic, E. M. Campbell, J. C. Fernández, J.-C. Gauthier, M. Geissel, M. Hegelich, H. Pépin, H. Popescu, N. Renard-Le Galloudec, M. Roth, J. Schreiber, R. Stephens, and T. E. Cowan. *Comparison of Laser Ion Acceleration from the Front and Rear Surfaces of Thin Foils*. Physical Review Letters, 94:045004, (2005).
25. J. S. Green, A. P. L. Robinson, N. Booth, D. C. Carroll, R. J. Dance, R. J. Gray, D. A. MacLellan, P. McKenna, C. D. Murphy, D. Rusby, and L. Wilson. *High efficiency proton beam generation through target thickness control in femtosecond laser-plasma interactions*. Applied Physics Letters, 104:214101, (2014).
26. K. Zeil, S. D. Kraft, S. Bock, M. Bussmann, T. E. Cowan, T. Kluge, J. Metzkes, T. Richter, R. Sauerbrey and U. Schramm. *The scaling of proton energies in ultrashort pulse laser plasma acceleration*. New Journal of Physics, 12: 045015, (2010).
27. P. Antici, J. Fuchs, S. Atzeni, A. Benuzzi, E. Brambrink, M. Esposito, M. Koenig, A. Ravasio, J. Schreiber, A. Schiavi and P. Audebert. *Isochoric heating of matter by laser-accelerated high-energy protons*. Journal of Physics, IV 133:1077-1079, (2006).
28. S. C. Wilks, W. L. Kruer, M. Tabak, A. B. Langdon. *Absorption of ultra-intense laser-pulses*. Physical Review Letters, 69:1383, (1992).
29. A. Mančić, J. Fuchs, P. Antici, S. A. Gaillard, P. Audebert. *Absolute calibration of photostimulable image plate detectors used as (0.5–20 MeV) high-energy proton detectors*. Review of Scientific Instruments, 79:073301, (2008).
30. T. Bonnet, M. Comet, D. Denis-Petit, F. Gobet, F. Hannachi, M. Tarisien, M. Versteegen, and M. M. Aleonard. *Response functions of Fuji imaging plates to monoenergetic protons in the energy range 0.6-3.2 MeV*. Review of Scientific Instruments, 84:013508, (2013).

31. D. Renzelli, P. Barone, V. Pingitore, F. Sirianni, R. Purri, M. Davoli, D. Barca, A. Oliva. *SAR TL dating of neolithic and medieval ceramics from Lamezia, Calabria (South Italy): a case study*. *Mediterranean Archaeology and Archaeometry*, 13:1 277, (2013).
32. J. F. Seelya, G. E. Holland, L. T. Hudsonc, C. I. Szaboc, A. Heninsec, H.-S. Parke, P. K. Patele, R. Tommasini, J. M. Laminga *K-shell spectra from Ag, Sn, Sm, Ta, and Au generated by intense femtosecond laser pulses*. *High Energy Density Physics*, 3:263, (2007).
33. S. N. Chen, M. Gauthier, D. P. Higginson, S. Dorard, F. Mangia, R. Riquier, S. Atzeni, J.-R. Marquès, and J. Fuchs. *Monochromatic short pulse laser produced ion beam using a compact passive magnetic device*. *Review of Scientific Instruments*, 85:043504, (2014).
34. V. Scuderia, S. Bijan Jia, M. Carpinelli, G.A.P. Cirrone, G. Cuttone, G. Korn, T. Licciardello, M. Maggiore, D. Margarone, P. Pisciotta, F. Romano, F. Schillaci, b, C. Stancampiano, A. Tramontan. *Development of an energy selector system for laser-driven proton beam applications*. *Nuclear Instruments and Methods in Physics Research A*, 740:8793, (2014).
35. G. Shi, E. Kioupakis. *Electronic and Optical Properties of Nanoporous Silicon for Solar-Cell Applications*. *ACS Photonics*, 2:2, 208-215, (2015).
36. K. Aydin, V. E. Ferry, R. M. Briggs, H.A. Atwater. *Broadband polarization-independent resonant light absorption using ultrathin plasmonic super absorbers*. *Nature Communications*, 517, (2011).
37. F. Rosei. *Nanostructured surfaces: challenges and frontiers in nanotechnology*. *Journal of Physics: Condensed Matter*, 16 S1373-S1436,(2004).
38. V. F. Paz, M. Emons, K. Obata, A. Ovsianikov, S. Peterhänsel, K. Frenner, C. Reinhardt, B. Chichkov, U. Morgner W. Osten. *Development of functional sub-100 nm structures with 3D two-photon polymerization technique and optical methods for characterization*. *Journal of Laser Applications*, 24: 042004, (2012).

39. T. Goda, T. Iyoda. *Ultra-high density electrolytic nanoreactors composed of liquid crystalline block copolymer template: water-electrolysis-induced deposition of cerium oxyhydroxide nanorod array*. Journal of Material Chemistry, 22: 9477-9480, (2012).
40. H. Tong, S. Ouyang, Y. Bi, N. Numezawa, M. Oshikiri. *Nano-photocatalytic materials: possibilities and challenges*. Advanced Material, 24:229, (2014).
41. S.C. Wilks, W.L. Kruer, M. Tabak, A.B. Langdon. *Nano-photocatalytic Materials: Possibilities and Challenges*. Physical Review Letters, 69:1383, (1992).
42. H. Schwoerer, S. Pfotenhauer, O. Jäckel, K. U. Amthor, B. Liesfeld, W. Ziegler, R. Sauerbrey, K.W.D. Ledingham, T. Esirkepov. *Laser-plasma acceleration of quasi-monoenergetic protons from microstructured targets*. Nature 439:445-448, (2006).
43. D. Margarone, O. Klimo, I.J. Kim, J. Prokapek, J. Limpouch, T.M. Jeong, T. Mocek, J. Pikal, H.T. Kim, J. Proka, K.H. Nam, L. Stolcov, I.W. Choi, S.K. Lee, J.H. Sung, T.J. Yu, G. Korn. *Bidimensional Particle-In-Cell simulations for laser-driven proton acceleration using ultra-short, ultra-high contrast laser*. Physical Review Letters, 109:234801, (2012).
44. S. Okihara, T. Zh Esirkepov, K. Nagai, S. Shimizu, F. Sato, M. Hashida, T. Iida, K. Nishihara, T. Norimatsu, Y. Izawa, S. Sakabe. *Generation of high-energy protons from the Coulomb explosion of hydrogen clusters by intense femtosecond laser pulses*. Physical Review E, 69:026401, (2004).
45. Y.T. Li. Zhang, Z.M. Sheng, Y.Y. Ma, Z. Jin, Z.L. Chen, R. Kodama, T. Matsuoka, M. Tampo, K. A. Tanaka, T. Tsutsumi, T. Yabuuchi. *Demonstration of bulk acceleration of ions in ultra-intense laser interactions with low-density foams*. Plasma Physics E . 72, 066404, (2005).
46. L. Willingale, S.R. Nagel, A.G.R. Thomas, C. Bellei, R.J. Clarke, A.E. Dangor, R. Heathcote, M.C. Kaluza, C. Kamperidis, S. Kneip, K. Krushelnick, N. Lopes, S.P.D. Mangles, W. Nazarov, P.M. Nilson, Z. Najmudin. *Characterization of High-Intensity Laser Propagation in the Relativistic Transparent Regime through Measurements of Energetic Proton Beams*. Physical Review Letters, 102:125002, (2009).

47. P. Antici, A. Mancic, M. Nakatsutsumi, P. Audebert, E. Brambrink, S. Gaillard, W. Nazarov, J. Fuchs, Plasma Phys. Control. *Tests of proton laser-acceleration using circular laser polarization, foams and half gas-bag targets*. Plasma Physics and Controlled Fusion, 53:014002, (2011).
48. P. Antici, J. Fuchs, E. d'Humieres, J. Robiche, E. Brambrink, S. Atzeni, A. Schiavi, Y. Sentoku, P. Audebert, H. Pepin. *Laser acceleration of high-energy protons in variable density plasmas*. New Journal of Physics, 11:2, 023038, (2009).
49. M. Barberio, F. Stranges, F. Xu. *Coating geometry of Ag, Ti, Co, Ni, and Al nanoparticles on carbon nanotubes*. Applied Surface Science, 334: 174-179, (2015).
50. K.L. Kelly, E. Coronado, Lin Zhao, G.C. Schatz. *The Optical Properties of Metal Nanoparticles: The Influence of Size, Shape, and Dielectric Environment*. Journal of Physical Chemistry B, 107:668-677, (2003).
51. a) W. Yan, K. Komvopoulos. *A Finite Element-Based Elastic-Plastic Model for the Contact of Rough Surfaces*. Journal Applied Physics 84, 3617, (1998); b) Y. F. Peng, Y. B. Guo. *An adhesion model for elastic-plastic fractal surfaces*. Journal of Applied Physics 102, 053510, (2007).
52. NIST XPS data base <http://srdata.nist.gov/xps/>.
53. K. Aydin, V.E. Ferry, R.M. Riggs, H. A. Atwater. *Broadband, polarization-independent resonant light absorption using ultrathin plasmonic super absorbers*. Nature Communications, 2: 517, (2011).
54. A. Mančić, J. Fuchs, P. Antici, S.A. Gaillard, P. Audebert. *Absolute calibration of photostimulable image plate detectors used as (0.5-20 MeV) high-energy proton detectors*. Review Science Instruments 79: 073301, (2008).
55. T. Bonnet, M. Comet, D. Denis-Petit, F. Gobet, F. Hannachi, M. Tarisien, M. Versteegen, and M. M. Aleonard. *Response functions of Fuji imaging plates to monoenergetic protons in the energy range 0.6-3.2 MeV*. Review of Scientific Instruments, 84:013508, (2013).

56. M. Barberio, P. Barone, A. Bonanno, M. Camarca, F. Xu. *Thermo and iono-luminescence on MWCNT bundles*. Radiation Physics and Chemistry, 76:3,492-494, (2007).
57. M. Barberio, P. Barone, A. Oliva. Optical properties of ZnS-carbon nanotubes composites. Radiation Physics and Chemistry, 81:6, 642-646, (2012).
58. C. Ronda. *Luminescence: from Theory to Applications*. Wiley-VCH, Verlag GmbH & Co. KGaA, (2008).
59. H. S. Nalwa, L. S. Rohwer. *Handbook of Luminescence*. Display Materials and Devices, (2003). ISBN: 1-58883-010-1.
60. S. Payeur, S. Fourmaux, B. E. Schmidt, J. P. MacLean, C. T. Chervenkov, F. Légaré, M. Piché, J. C. Kieffer. *Generation of a beam of fast electrons by tightly focusing a radially polarized ultrashort laser pulse*. Applied Physics Letters, 101:041105, (2012).